Instituto Nacional de Matemática Pura e Aplicada

Lattice Boltzmann modelling for immiscible Rayleigh-Taylor turbulence

by

Hugo Saraiva Tavares

Rio de Janeiro-RJ

December 2020

Instituto Nacional de Matemática Pura e Aplicada

Lattice Boltzmann modelling for immiscible Rayleigh-Taylor turbulence

by

Hugo Saraiva Tavares [†]

under the supervision of Prof. Alexei A. Mailybaev

Thesis presented to the Postgraduate Program in Mathematics at Instituto Nacional de Matemática Pura e Aplicada-IMPA as partial fulfillment of the requirements for the degree of Doctor of Mathematics.

Rio de Janeiro-RJ

December 2020

[†]This work had financial support from CAPES

Aos cientistas brasileiros, em especial aqueles que estão pesquisando na linha de frente de combate ao COVID-19.

Abstract

Rayleigh-Taylor (RT) instability occurs when a lighter fluid is pushing a heavier fluid. We study turbulence induced by the RT instability for two-dimensional immiscible two-component flows by using a multicomponent lattice Boltzmann method. First, we develop and test the numerical method. Then, based on numerical simulations implemented on GPUs (Graphics Processing Units), we analyze the energy budgets for RT systems. This analysis verifies some important theoretical assumptions about the immiscible RT turbulence using accurate numerical experiments, like the connection between the variation of interface energy and the energy flux due to the Korteweg stress tensor. We also analyze the energy dissipation, showing that the interface acts as a source of vorticity. In the second part of our numerical tests, we approach a phenomenological theory for the immiscible RT turbulence. We extend this theory to the two-dimensional case using the earlier results by Chertkov, Kolokolov and Lebedev (2005) for three-dimensional flows. We compare, numerically, the growth of the mixing layer, typical velocity, average density profiles and enstrophy between the cases of immiscible and miscible two-component fluids. Also, we investigate the evolution of typical drop size and the dynamics of the interface length in the emulsion-like state, confirming the power-law theoretical predictions.

Keywords: Rayleigh-Taylor turbulence; immiscible fluids; lattice Boltzmann method.

Resumo

A instabilidade de Rayleigh-Taylor (RT) ocorre quando um fluido mais leve é acelerado de encontro a um fluido mais pesado. Nós estudamos a turbulência induzida pela instabilidade de RT para escoamentos bidimensionais imiscíveis com duas componentes usando um método lattice Boltzmann multicomponente. Primeiro, desenvolvemos e testamos o método numérico. Em seguida, com base em simulações numéricas implementadas em GPUs (Graphics Processing Unit - Unidade de Processamento Gráfico), analisamos os balanços de energia para sistemas RT. Nesta análise verificamos alguns pressupostos teóricos importantes sobre a turbulência de RT imiscível usando experimentos numéricos precisos, como a relação entre a variação da energia da interface e o fluxo de energia devido ao tensor de Korteweg. Analisamos também a dissipação de energia, mostrando que a interface atua como fonte de vorticidade. Na segunda parte de nossos testes numéricos, abordamos uma teoria fenomenológica para a turbulência imiscível de RT. Estendemos essa teoria para o caso bidimensional usando os resultados anteriores de Chertkov, Kolokolov e Lebedev (2005) para fluxos tridimensionais. Comparamos numericamente o crescimento da camada de mistura, velocidade típica, perfis de densidade média e enstrofia entre os casos de fluidos com duas componentes imiscíveis e miscíveis. Além disso, investigamos a evolução do tamanho típico de pequenas estruturas e a dinâmica do comprimento total da interface no estado emulsão para tempos longos, confirmando previsões teóricas em forma de leis de potência.

Palavras-chave: Turbulência de Rayleigh-Taylor; fluidos imiscíveis; método lattice Boltzmann.

Acknowledgments

First, to my parents, the main reasons for my achievements. Especially my mother, who was a great model of perseverance and determination in my life.

To my advisor Prof. Alexei A. Mailybaev for his teachings, patience and support on the most diverse occasions. With Alexei I learned a whole new way of thinking scientifically. I will be forever grateful.

To my colleagues in the Fluid Dynamics Laboratory: Guilherme Tegoni, Luis Fernando, Jose Manuel, Ciro Campolina and especially to my companion Júlia Domingues Lemos for the essential help in the most difficult times of the pandemic.

To Sergio Pilotto and Daniel Lins de Albuquerque for the technical support provided in several computational aspects of the research of this thesis.

To my friends from the Archdiocesan Seminary of São José in Rio de Janeiro, especially Canon Leandro Câmara and the nun Terezinha Fernandes for all the support in my initial moments of my doctorate, contributing a lot to my adaptation in the city of Rio de Janeiro.

To Prof. Luca Biferale and Prof. Mauro Sbragaglia from the University of Rome-Tor Vergata for all their shared knowledge about the Boltzmann lattice method and turbulent flows. Such contacts had the valuable support of the ERC-ADG NewTURB project.

To Francesca Pelusi of the University of Rome-Tor Vergata for the many enriching discussions about the lattice Boltzmann method for fluid mixtures.

To Prof. J. Hans Bruining of the Delft University of Technology (TU Delft) for the valuable conversations and collaborations during my sandwich period in the Netherlands.

To the professors of the examining board for accepting to participate in the evaluation of this work and for the valuable suggestions.

To Alexandra Elbakyan for her remarkable efforts to popularize access to scientific articles.

To Prof. Leslie Lamport and Prof. Donald Knuth for their extraordinary contri-

bution to the development of tools for writing mathematical texts.

To CAPES and NUFFIC for their financial support.

And to all the others who somehow contributed to this achievement.

Agradecimentos

Primeiramente aos meus pais e irmãos, as maiores razões das minha conquistas. Em especial a minha mãe, que foi um grande modelo de perseverança e determinação na minha vida.

Ao meu orientador Prof. Alexei A. Mailybaev pelos ensinamentos, paciência e apoio nas mais diversas ocasiões. Com Alexei aprendi toda uma nova maneira de pensar cientificamente. Serei eternamente grato.

Aos meus colegas do Laboratório de Dinâmica de Fluidos: Guilherme Tegoni, Luis Fernando, Jose Manuel, Ciro Campolina e principalmente à minha companheira Júlia Domingues Lemos pela ajuda essencial nos tempos mais difíceis de pandemia.

A Sergio Pilotto e Daniel Lins de Albuquerque pelo suporte técnico prestado em diversos aspectos computacionais da pesquisa desta tese.

Aos meus amigos do Seminário Arquidiocesano de São José no Rio de Janeiro, em especial ao Cônego Leandro Câmara e a freira Terezinha Fernandes por todo o surporte nos meus momentos iniciais do doutorado, contribuindo muito para a minha adaptação na cidade do Rio de Janeiro.

Aos professores Luca Biferale e Mauro Sbragaglia da Universidade de Roma-Tor Vergata por todo o conhecimento compartilhado sobre o método lattice Boltzmann e escoamentos turbulentos. Tais contatos tiveram o valioso suporte do projeto ERC-ADG NewTURB.

A Francesca Pelusi da Universidade de Roma–Tor Vergata pelas enriquecedoras discussões sobre o método lattice Boltzmann para misturas de fluidos.

Ao Prof. J. Hans Bruining da Universidade Técnica de Delft (TU Delft) pelas valiosas conversas e colaborações durante meu período sanduíche na Holanda.

Aos professores da banca examinadora por aceitarem participar da avaliação deste trabalho e pelas valiosas sugestões.

Aos professores do departamento de matemática da UFCG, em especial aos professores Henrique Fernandes, Marco Antônio e Severino Horácio por terem me introduzido no estudo de uma série de tópicos de matemática avançada e por sempre estarem

dispostos a me ajudar.

A Alexandra Elbakyan pelo seu notável empenho para a popularização do acesso a artigos científicos.

Aos professores Leslie Lamport e Donald Knuth pela extraordinária contribuição ao desenvolvimento de ferramentas para a escrita de textos matemáticos.

A CAPES e a NUFFIC pelo apoio financeiro.

E a todos os outros que de alguma forma contribuíram para esta conquista.

Contents

Chapter 1

Introduction

When a heavy fluid is accelerated against a lighter fluid the so-called Rayleigh-Taylor (RT) instability can develop [76, 92], which eventually leads to a mixing layer with a turbulent motion called Rayleigh-Taylor turbulence. In this process the two fluids seek to reduce the total potential energy of the system [25]. The turbulent regime is relevant in many different contexts, for example, in the understanding of the Earth's climate, in the nuclear fusion process [73, 21] and as a key mechanism for thermonuclear flames in some types of supernovae [103, 83]. In the context of classical fluids, the incompressible Rayleigh-Taylor turbulence has important properties [13], one of the most important of which is the quadratic growth of the mixing layer width. In some cases, important connections have been found with classical theories of turbulence for simple fluids [38, 28, 1].

Physical experiments of the RT instability have been challenging due to the difficulty of sustaining an unstable density stratification necessary to set up the appropriate initial conditions for the instability [25, 75, 31, 46, 97]. Despite this limitation, considerable advances in numerical simulations of the Rayleigh-Taylor instability have been verified in the last decades, especially in the context of the systems with miscible fluids [28, 10, 26, 13, 8, 101]. Only a few works have been dedicated to the immiscible viscous case [25, 99, 64, 18, 22, 66], and most of them are devoted to the early stages of the instability with little information about the state of developed turbulence. One of the reasons for this is the highly complicated pattern formed by the interfaces that appear in the immiscible case, originating high gradients and singularities in the solutions,

which is a source of challenging numerical instabilities in many numerical methods for multicomponent and multiphase flows.

Concerning to the theoretical aspects of the immiscible RT turbulence, it is only recently that a consistent phenomenological study of the effects of surface tension has been carried out by Chertkov and collaborators [29]. It followed the earlier work [28], where a phenomenological theory was developed for two and three-dimensional miscible RT turbulence considering Boussinesq approximation. Said work considers a 3D scenario, in which the direct energy cascade happens in a range of scales limited by the mixing layer width (integral scale) and the viscous (Kolmogorov) scale, both dependent on time. In the two dimensional case, the lack of energy and enstrophy cascades leads to the assumption of Bolgiano–Obukhov theory describing the cascade of temperature fluctuations in the inertial range [17, 71]. The work [29] described the theory of three-dimensional immiscible RT turbulence, studying the effects of the surface tension in the emulsion-like state and predicting the rate of growth for the typical drop size.

In this thesis, we extend the phenomenological theory of [29] for the two-dimensional immiscible RT turbulence. This extension includes predictions for the growth of the total length of the interface and the typical drop size. We also provide predictions for the evolution of the enstrophy in the miscible and immiscible cases, which have not been addressed earlier. These predictions are tested using numerical simulations based on the multicomponent lattice-Boltzmann method with Shan-Chen pseudopotential model [55, 89]. In the immiscible case, this method is able to accurately overcome the inherent numerical complexity caused by the complicated structure of the interface that appears in the fully developed turbulent regime [82, 25, 99]. This method also admits parallel implementations in many situations, which is very important for statistical analyses that require a substantial number of simulations, like in our numerical verification for the phenomenological predictions.

We run several simulations of the RT turbulence in parallel on Graphics Processing Units (GPUs) using the CUDA compute platform [70] with a computational grid with resolution 10.000×5.000. In this step of our research, the optimization of the lattice-Boltzmann algorithms for GPUs used in this thesis was developed in collaboration with Prof. Luca Biferale and Prof. Mauro Sbragaglia from the University of Rome-Tor Vergata. The collaboration happened through direct contact in two long-

term visits between the years 2018 and 2019. The first visit received a support from the ERC-ADG NewTURB project; and the second visit in 2019 was supported by the project CAPES/NUFFIC, which also included the collaboration with Prof. J. Hans Bruining from Delft University of Technology.

In 2018, the research was focused in basic verifications of the Shan-Chen multicomponent method for the immiscible Rayleigh-Taylor instability. We validate basic lattice-Boltzmann codes by testing dispersion relations. After these validations, we focused on the optimization of the LBM codes for simulations in CUDA. With the optimized versions of the codes, in 2019 a few preliminary phenomenological numerical verifications were obtained about the evolution of the mixing layer, total length of the interface and typical drop size. These results were presented in 32nd Brazilian Mathematics Colloquium; in the workshop "Waves, Coherent Structures, and Turbulence (WCST2019)" held at the University of East Anglia (Norwich, UK); and in the conference "Universal features of hydrodynamical, optical and wave turbulence" held at the University of Nice Sophia Antipolis in Nice (France).

At the end of 2019, our research addressed the implementation of a CUDA code of the Shan-Chen multicomponent method in the computer cluster Tsunami5 on IMPA. Simultaneously, the analysis of the energy budget of the Rayleigh-Taylor flows generated some results. In the beginning of 2020, the final numerical validations of the phenomenology for immiscible Rayleigh-Taylor flows were obtained (which we present in the final chapter of this thesis). These results can be divided into two main parts: one part dedicated to the verifications of the phenomenological predictions, and a second part addressed the numerical analysis of the energy budget. Some of these results were presented in the 29th International Conference on Discrete Simulation of Fluid Dynamics (DSFD 2020), organized by the University of Tuscia in Viterbo (Italy). After this conference, our work about the numerics of the energy budget received an invitation to be published in the journal Philosophical Transactions of the Royal Society A [91], as a contribution to the progress in mesoscale methods for fluid dynamics simulation. The summary of the numerical verifications of the phenomenological predictions presented in this thesis can be found in the article [90].

This thesis is organized as follows:

- In Chapter 2 we describe the basic equations for the classical Rayleigh-Taylor system, miscible and immiscible, characterizing the Boussinesq approximation and studying the surface tension effects. The details of the mechanisms that generate the Rayleigh-Taylor instability are studied in the analysis of the dispersion relation.

- In Chapter 3 we describe the multicomponent lattice-Boltzmann method with Shan-Chen pseudopotential model. We show how to consider the Boussinesq approximation for the Rayleigh-Taylor systems with this method, giving details of the setup of the simulations used to test the proposed phenomenology.

- In Chapter 4 we provide some verifications and validations of the Shan-Chen multicomponent method. We first calculate the surface tension coefficient using the Laplace-Young test in the numerical results of LBM simulations of droplets. The accuracy of the Shan-Chen method for the initial times of the immiscible Rayleigh-Taylor instability is tested by verifying classical dispersion relations. At the end of this chapter, we discuss some limitations in this method for simulations of immiscible mixtures, verifying the magnitude of the so-called spurious currents in droplets simulation [89, 55].

- In Chapter 5 we analyse the energy budget in RT flows. In the first part we study the evolution of the kinetic and potential energies of the systems, comparing miscible and immiscible systems side by side. In the energy budget comparison between the miscible and immiscible flows, some differences due to the energy necessary to form the interfaces are expected to be observed [12, 32, 42, 65], as well as the possible generation of the vorticity in them [93, 20]. To investigate such possibility, we calculate numerically the energy of the interface and we compare with the energy flux due to the Korteweg stress tensor [3, 42]. The generation of vorticity at the interface is investigated by analyzing the evolution of the enstrophy and PDFs of the vorticity fields. At the end of the chapter we analyse the existence of critical points in the transition to turbulent regimes in the immiscible case by studying the evolution of the typical curvature values of the interface.

- In Chapter 6 we construct phenomenological predictions for mixing layer, typical velocity and averaged density profile, with the respective numerical verifications, showing a direct comparison between miscible and immiscible cases. The final part of this chapter is dedicated the phenomenological properties of the interface, where we first investigate the evolution of the typical drop size and total length of the interface in the emulsion-like state, and at the end we study the evolution of enstrophy. The statistics for the enstrophy are also used to understand the influence of the interface on small-scale statistics and to verify the validity of the assumption of the Bolgiano-Obukhov regime in our phenomenology.

- Chapter 7 provides some conclusions and perspectives.

Chapter 2

Immiscible and miscible Rayleigh-Taylor systems

2.1 Governing equations

An interface between two fluids of different densities becomes unstable when the heavier fluid is placed above the lighter fluid under gravity [27]. In the classical formulation of fluid dynamics, the flow is described by the incompressible Navier–Stokes equations

$$\rho\left(\frac{\partial \mathbf{u}}{\partial t} + \mathbf{u}\cdot\nabla\mathbf{u}\right) = -\nabla p + \nabla\cdot\left[\mu\left(\nabla\mathbf{u} + (\nabla\mathbf{u})^T\right)\right] + \mathbf{f}, \tag{2.1}$$

$$\nabla\cdot\mathbf{u} = 0, \tag{2.2}$$

where $\mathbf{u}$ is the fluid velocity depending on spatial coordinates $\mathbf{x}$ and time t, as well as the pressure p. ρ and μ are the fluid density and dynamic viscosity, and the buoyancy forcing term is

$$\mathbf{f} = \rho\mathbf{g} \tag{2.3}$$

with the acceleration of gravity $\mathbf{g}$ pointing downwards. In this thesis we study two-dimensional flows with $\mathbf{x} = (x, y)$ for two different physical models describing the immiscible and miscible flows.

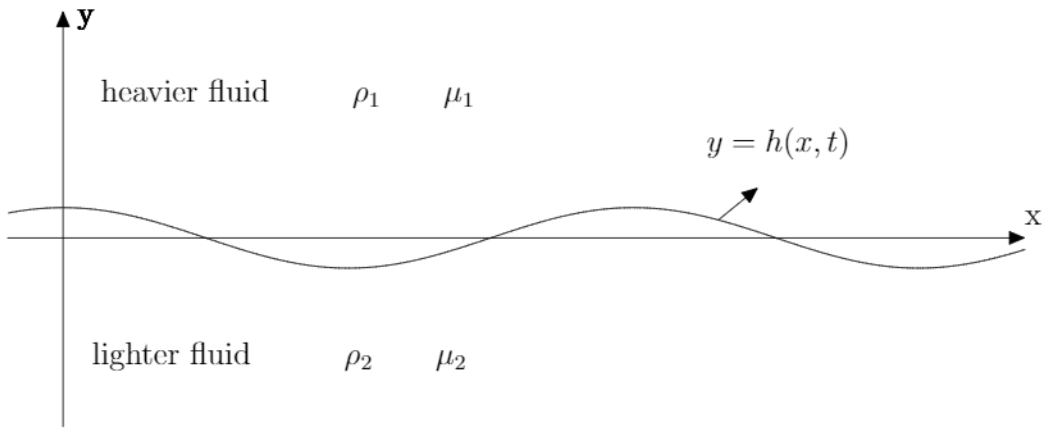

Figure 2.1: Unstable configuration characteristic of the Rayleigh-Taylor instability. In this configuration the fluid with the bigger density ρ_1 is placed above the fluid with the smaller density ρ_2. In this configuration, any single mode pertubation $y = h(x,t)$, with a wave number smaller than some critical value, can generate the instability, as we see in the next subsection.

The immiscible formulation considers two fluid phases with constant densities and viscosities: ρ_1 and μ_1 for the first phase and ρ_2 and μ_2 for the second phase. We assume that $\rho_1 > \rho_2$, i.e., the first phase is heavier. The two subdomains occupied by each phase are separated by a moving interface $\Gamma(t) = \{(x,y) \in \mathbb{R}^2; y = h(x,t)\}$, see Fig 2.1. Equations of motion for each phase are given by (2.1) with the corresponding constant values of density and viscosity. At the interface, the boundary conditions take the form

$$\mathbf{x} \in \Gamma : \quad \begin{cases} [\mathbf{u}]_\Gamma = 0 \\ \mathbf{u} \cdot \mathbf{n} = u_\Gamma \\ \left[-p\mathbf{n} + \mu\left(\nabla\mathbf{u} + (\nabla\mathbf{u})^T\right)\mathbf{n}\right]_\Gamma = -\gamma\kappa\mathbf{n}, \end{cases} \tag{2.4}$$

where $[\cdot]_\Gamma$ denotes the jump of the quantity across the interface, $\mathbf{n}$ and u_Γ are the interface normal vector and velocity, γ is the surface tension and κ is the interface curvature. In our models we consider a constant surface tension, for models with variable surface tensions, see [87, 3]. The first two conditions in (2.4) describe the continuity of fluid velocity and mass conservation, while the last condition corresponds to the balance of momentum. We will mostly focus on configurations with rigid flat boundaries on the top and the bottom, and periodic boundary conditions in the horizontal directions. The no-slip condition, $\mathbf{u} = 0$, is assumed at the rigid boundaries.

When density variations compared to their mean values are small, we can use the Boussinesq approximation for the system [56]. In this approximation the density fluctuations $\delta\rho = \rho - \rho_0$, where $\rho_0 = (\rho_1 + \rho_2)/2$ is the reference density, affect only the buoyancy term [56, 51]. In the rest of the momentum equation (2.1) the density is set to the constant reference value ρ_0. If viscosities μ_1 and μ_2 of two components are close, one can approximately use the mean kinematic viscosity $\nu = (\mu_1 + \mu_2)/(2\rho_0)$. After this approximations, the momentum equation (2.1) becomes

$$\rho_0 \left(\frac{\partial \mathbf{u}}{\partial t} + \mathbf{u} \cdot \nabla \mathbf{u} \right) = -\nabla p + \rho_0 \nu \nabla^2 \mathbf{u} + \delta\rho \mathbf{g} \tag{2.5}$$

where the background value of the buoyancy term $\rho_0 \mathbf{g}$ is included into pressure term. Introducing the order parameter ϕ as a function equal 1 in the first phase and -1 in the second phase, it is possible to refine the buoyancy contribution in (2.5) in terms of ρ_1, ρ_2 and ϕ as [25]

$$\begin{aligned} \delta\rho\mathbf{g} &= -(\rho - \rho_0) g \mathbf{e}_y \\ &= -\left[\rho_1 \left(\frac{1+\phi}{2} \right) + \rho_2 \left(\frac{1-\phi}{2} \right) - \rho_0 \right] g \mathbf{e}_y \\ &= -\frac{(\rho_1 - \rho_2)}{2} \phi g \mathbf{e}_y \\ &= -\rho_0 \mathcal{A} \phi g \mathbf{e}_y \\ &= -\rho_0 \tilde{g} \phi \mathbf{e}_y. \end{aligned} \tag{2.6}$$

where $\mathcal{A} = (\rho_1 - \rho_2)/(\rho_1 + \rho_2)$ is the so-called Atwood number, $\tilde{g} = \mathcal{A} g$ is the effective gravity and $\mathbf{e}_y = (0, 1)$ is the unit vector in vertical direction.

2.2 Linear stability analysis

In this section, we consider an idealized situation for the Rayleigh-Taylor instability with an initial configuration at $t = 0$ corresponding to a fluid at rest, with zero initial velocity, with the heavier (first) component occupying the upper half-plane $y > 0$ and the lighter (second) component occupying the lower half-plane $y < 0$, see Fig. 2.1. In this configuration we investigate with more details the conditions that lead to the development of the Rayleigh-Taylor instability by analyzing the linearized equations of motion and finding the single modes perturbation growth. In this analysis we suppose

that the amplitude of the perturbations are small in a such way that the conditions at $y = h(x,t)$ are approximately valid also for $y = 0$. First, for the sake of clarity, we consider a system composed by two ideal fluids. Thereafter we discuss the implication of the viscosity in the developed calculations.

Consider the Rayleigh-Taylor system represented in Fig. 1.1, with the location of the interface described by a function $y = h(x,t)$ and with $\mu_1 = \mu_2 = 0$. By the Stokes theorem, there exist potential functions ξ_1 and ξ_2 such that the velocity fields $\mathbf{u}_1$, for $y > h$, and $\mathbf{u}_2$, for $y < h$, are given by

$$\mathbf{u}_1 = \nabla\xi_1 \quad \text{for} \quad y > h, \tag{2.7}$$

$$\mathbf{u}_2 = \nabla\xi_2 \quad \text{for} \quad y < h. \tag{2.8}$$

with

$$\Delta\xi_1 = \Delta\xi_2 = 0, \tag{2.9}$$

by the incompressibility condition (2.2). With the potential flow assumption, one can show that from (2.1) for each component we obtain [40]

$$\nabla\left(\frac{\partial\xi_i}{\partial t} + \frac{1}{2}|\nabla\xi_i|^2 + gy + \frac{p_i}{\rho_i}\right) = 0 \quad \text{for } i = 1,2. \tag{2.10}$$

or, equivalently,

$$\frac{\partial\xi_1}{\partial t} + \frac{1}{2}|\nabla\xi_1|^2 + gy + \frac{p_1}{\rho_1} = C_1(t) \quad \text{for } y > h(x,t) \tag{2.11}$$

$$\frac{\partial\xi_2}{\partial t} + \frac{1}{2}|\nabla\xi_2|^2 + gy + \frac{p_2}{\rho_2} = C_2(t) \quad \text{for } y < h(x,t). \tag{2.12}$$

where $C_i(t)$ are functions of the time only. We can set $C_i(t) = 0$. In fact, if we define

$$\theta_i = \xi_i - D_i(t), \quad \text{for} \quad i = 1,2, \tag{2.13}$$

where $D_i(t)$ is an integral of $C_i(t)$, we have $\nabla\theta_i = \nabla\xi_i = \mathbf{u}_i$ and

$$\frac{\partial\theta_1}{\partial t} + \frac{1}{2}|\nabla\theta_1|^2 + gy + \frac{p_1}{\rho_1} = 0 \quad \text{for } y > h(x,t) \tag{2.14}$$

$$\frac{\partial\theta_2}{\partial t} + \frac{1}{2}|\nabla\theta_2|^2 + gy + \frac{p_2}{\rho_2} = 0 \quad \text{for } y < h(x,t). \tag{2.15}$$

At each time, the interface motion can be given by $s(x,y,t) = 0$, where the function

$$s(x,y,t) = y - h(x,t). \tag{2.16}$$

If a particle of the fluid occupies a position $\mathbf{r}(t)$ in the fluid domain, then the velocity of this particle is given by $\frac{d\mathbf{r}(t)}{dt} = \mathbf{u}(\mathbf{r}(t), t)$, where $\mathbf{u}$ is the velocity field satisfying (2.7) in the component 1 and (2.8) in the component 2. At the interface we have $s(\mathbf{r}(t), t) = 0$ for any time $t > 0$, which implies that

$$\frac{\partial s}{\partial t} + \mathbf{u} \cdot \nabla s = 0. \tag{2.17}$$

For a particle in the component 1 immediately above the interface $y = h_+(x, t)$, we have

$$\lim_{y \to h, y > h} \mathbf{u}(x, y, t) = \mathbf{u}_1(x, h_+, t) = \nabla \theta_1(x, h_+, t), \tag{2.18}$$

and for a particle immediately below the interface $y = h_-(x, t)$ in the component 2

$$\lim_{y \to h, y < h} \mathbf{u}(x, y, t) = \mathbf{u}_1(x, h_-, t) = \nabla \theta_2(x, h_-, t), \tag{2.19}$$

where θ_1 and θ_2 are given by (2.13). Then, from (2.17) and (2.16) we have

$$\frac{\partial s}{\partial t} + \nabla \theta_1 \cdot \nabla s = -\frac{\partial h}{\partial t} - \frac{\partial \theta_1}{\partial x}\frac{\partial h}{\partial x} + \frac{\partial \theta_1}{\partial y} = 0 \quad \text{at} \quad y = h_+ \tag{2.20}$$

and

$$\frac{\partial s}{\partial t} + \nabla \theta_2 \cdot \nabla s = -\frac{\partial h}{\partial t} - \frac{\partial \theta_2}{\partial x}\frac{\partial h}{\partial x} + \frac{\partial \theta_2}{\partial y} = 0 \quad \text{at} \quad y = h_-. \tag{2.21}$$

The pressures p_1 and p_2 can be related with the curvature κ of the interface by the Laplace-Young equation [86, 55]

$$p_1 - p_2 = \gamma \kappa = \gamma \frac{h_{xx}}{(1 + (h_x)^2)^{3/2}}. \tag{2.22}$$

In the linear analysis of the equations (2.14), (2.15), (2.20) and (2.21) we neglect all the quadratic terms, which also implies that $p_1 - p_2 \simeq \gamma h_{xx}$. Thus, we obtain the following system of linear equations for the inviscid immiscible Rayleigh-Taylor system

$$\begin{cases} \Delta \theta_1 = 0, & \text{for } y > 0, \\ \Delta \theta_2 = 0, & \text{for } y < 0, \\ \dfrac{\partial h}{\partial t} = \dfrac{\partial \theta_1}{\partial y}, \qquad \dfrac{\partial h}{\partial t} = \dfrac{\partial \theta_2}{\partial y}, & \text{for } y = 0, \\ \rho_1 \left(\dfrac{\partial \theta_1}{\partial t} + gh \right) + \gamma h_{xx} = \rho_2 \left(\dfrac{\partial \theta_2}{\partial t} + gh \right), & \text{for } y = 0, \end{cases} \tag{2.23}$$

with the boundary conditions far from the interface satisfying

$$\frac{\partial \theta_i}{\partial y} \to 0 \quad \text{for} \quad |y| \to \infty, \quad i = 1, 2. \tag{2.24}$$

We now seek solutions for three different functions h, θ_1 and θ_2 fulfilling the system (2.23). To do this we employ an eigenmode analysis

$$\theta_1 = A(y)\exp(ikx+\sigma t) \text{ for } y > h, \tag{2.25}$$

$$\theta_2 = B(y)\exp(ikx+\sigma t) \text{ for } y < h, \tag{2.26}$$

where k is the wave number, σ is the angular frequency and $A(y)$ and $B(y)$ are functions that correspond to usual analyzes by plane wave ansatz [40]. The forms (2.25) and (2.26) are compatible with the characteristic form of the general solutions of the system (2.23) obtained by method of the separation of the variables [36]. We also assume that the shape of the disturbed interface is given by a normal-mode expression

$$h = \hat{h}\exp(ikx+\sigma t). \tag{2.27}$$

where $\hat{h}$ is the mode amplitude. The potentials θ_1 and θ_2 satisfy the Laplace equation, which leads to

$$\frac{\partial A(y)}{\partial y} = k^2 A(y), \quad \frac{\partial B(y)}{\partial y} = k^2 B(y). \tag{2.28}$$

The conditions far from the interface (2.24) imply that $A(y) \propto \exp(-ky)$ and $B(y) \propto \exp(ky)$. Thus, from (2.25) and (2.26), we have the following equations for a single Fourier mode

$$\theta_1 = \hat{\theta_1}\exp(-ky)\exp(ikx+\sigma t) \text{ for } y > 0, \tag{2.29}$$

$$\theta_2 = \hat{\theta_2}\exp(ky)\exp(ikx+\sigma t) \text{ for } y < 0, \tag{2.30}$$

where $\hat{\theta_1}$ and $\hat{\theta_2}$ are the corresponding mode amplitudes. Inserting the modes in the system (2.23) we obtain the following algebraic system

$$\begin{bmatrix} \sigma & -k & 0 \\ \sigma & 0 & k \\ [g(\rho_1-\rho_2)-\gamma k^2] & \rho_1\sigma & -\rho_2\sigma \end{bmatrix} \begin{bmatrix} \hat{h} \\ \hat{\theta_1} \\ \hat{\theta_2} \end{bmatrix} = \begin{bmatrix} 0 \\ 0 \\ 0 \end{bmatrix}. \tag{2.31}$$

Analyzing the determinant of the coefficient matrix of the system (2.31), we can see that nontrivial *unstable* solutions with $\hat{h} \neq 0$ exist for

$$\sigma(k) = \sqrt{\left(\frac{\rho_1-\rho_2}{\rho_1+\rho_2}\right)gk - \gamma\frac{k^3}{\rho_1+\rho_2}} = \sqrt{\mathcal{A}gk - \gamma\frac{k^3}{2\rho_0}}. \tag{2.32}$$

This analysis implies that if $\mathcal{A} > 0$ and $k < \sqrt{2\rho_0 \mathcal{A} g/\gamma}$, then the initial perturbation of the interface grows exponentially,

$$h \sim \hat{h} e^{\sigma(k)t}, \tag{2.33}$$

with $\sigma(k)$ given by (2.32).

In the presence of viscosity, it is possible to use the previous procedure to estimate the dispersion relation in the case of fluids with small viscosity. In this case, the flow in the initial stages of the RT instability can be considered almost irrotational, and a direct estimation of the dispersion relation can be obtained using the viscous potential flow analysis (VPF) [48, 39, 88, 15]. In this analysis, the term $\mu \nabla^2 \mathbf{u}$ in the Navier-Stokes equation (2.1) is considered negligible, with the viscous stresses affecting only in the normal stress balance in (2.4) [88], i.e.,

$$-p_1 + 2\mu_1 \frac{\partial^2 \theta_1}{\partial y^2} - \left(-p_2 + 2\mu_2 \frac{\partial^2 \theta_2}{\partial y^2} \right) = -\gamma \frac{\partial^2 h}{\partial x^2}. \tag{2.34}$$

As a consequence, the last equation in the system (2.31) is changed to

$$(\rho_1 \sigma + 2\mu_1 k^2)\hat{\theta}_1 - (\rho_2 \sigma + 2\mu_2 k^2)\hat{\theta}_2 - \gamma k^2 = 0 \tag{2.35}$$

which leads to the following dispersion relation

$$\sigma(k) = -\nu k^2 + \sqrt{\mathcal{A} g k - \gamma \frac{k^3}{2\rho_0} + \nu^2 k^4}. \tag{2.36}$$

The formula (2.36) is actually known as an upper bound for the growth rate of the perturbation of the interface for fluids with arbitrary viscosity [27]. In the case of fluids with small viscosity, this upper-bound is also a good approximation of the actual value of the dispersion relation [15, 88].

In Fig. 2.2, we analyze the effects of the surface tension and viscosity in the dispersion relation (2.36). It is possible to see that without surface tension and viscosity (red dashed line), any perturbation can generate the instability for $\mathcal{A} > 0$. With the addition of the surface tension (blue dashed line) the instability is generated only for $k < \sqrt{2\rho_0 \mathcal{A} g/\gamma}$. The viscosity (black solid line) only reduces the growth rate without changing the critical wave number $k_c = \sqrt{2\rho_0 \mathcal{A} g/\gamma}$. In Chapter 4, we provide a series of tests verifying the dispersion relation (2.36) for the immiscible RT instability,

comparing with some results generated by the lattice Boltzmann method, a numerical technique to be described in Chapter 3.

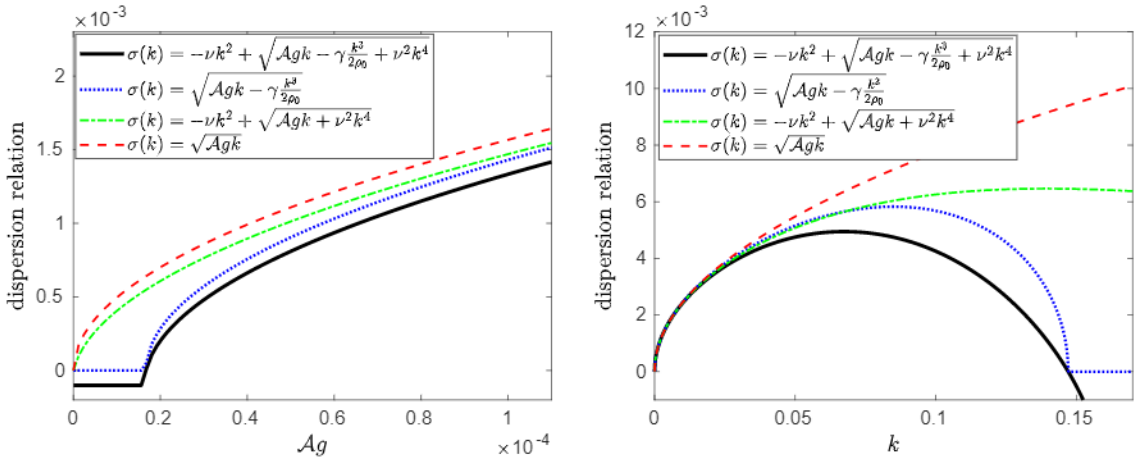

Figure 2.2: (a) Theoretical dispersion relations for the immiscible RT system for different values of the effective gravity $\tilde{g} = \mathcal{A}g$ with a fixed wave number $k = 2\pi/256$, and (b) for different values of the wave numbers and fixed effective gravity $\tilde{g} = \mathcal{A}g = 0.0006$. For both pictures the kinematic viscosity is $\nu = 0.1667$ and the surface tension coefficient $\sigma = 0.061$.

2.2.1 Miscible flow

In the miscible flow, the fluid is modeled by a single phase with a variable density. Analogously to the immiscible case, we write this density as $\rho = \rho_0 (1 + \mathcal{A}\phi)$ from the relation (2.6), which in the miscible case is a consequence of the law of additive volumes for mixtures of fluids with close densities [50, 49].

The order parameter $\phi(\mathbf{x}, t)$ describing density variations satisfies the convection–diffusion equation

$$\frac{\partial \phi}{\partial t} + \mathbf{u} \cdot \nabla \phi = \nabla \cdot (D \nabla \phi), \tag{2.37}$$

where D is the diffusion coefficient. In general, both viscous and diffusion coefficients are functions of density. Analogous formulation arises when the density is considered to be a function of temperature T, in which case $\phi = -\beta(T - T_0)$ with the coefficient of thermal expansion β [58]. The equations of motion for the Boussinesq approximation

in the miscible case are

$$\rho_0 \left(\frac{\partial \mathbf{u}}{\partial t} + \mathbf{u} \cdot \nabla \mathbf{u} \right) = -\nabla p + \rho_0 \nu \nabla^2 \mathbf{u} - \rho_0 \tilde{g} \phi \mathbf{e}_y, \tag{2.38}$$

$$\nabla \cdot \mathbf{u} = 0. \tag{2.39}$$

The initial condition for the miscible Rayleigh-Taylor instability is considered in the same form as for the immiscible configuration like in Fig. 2.1. If the interface is straight, $h \equiv 0$ then a uniform diffusion layer is developed at the interfacial region with limits that satisfy a diffusion equation derived from (2.37) [49].

When a small perturbation of the interface is introduced, the calculation of the dispersion relation for the miscible Rayleigh-Taylor instability is also analogous to the immiscible case, with the exception that in the miscible case we disregard the surface tension. This yields

$$\sigma(k) = -\nu k^2 + \sqrt{\mathcal{A} g k + \nu^2 k^4}. \tag{2.40}$$

In Fig. 2.2(a) and Fig. 2.2(b) we have a representation of (2.40) by the dashed green lines. In these cases, if $\mathcal{A} > 0$ then perturbations with arbitrary wave numbers can generate the instability.

2.3 Turbulent mixing

We can see that the system configuration outlined in Fig 2.1 is an unstable stationary solution: small perturbations of the interface with wavenumbers $k < \sqrt{2\rho_0 A g/\gamma}$ grow exponentially with the dispersion relation given by (2.36). After an initial linear growth such perturbations develop into nonlinear mushroom-like structures evolving further to the fully developed turbulent mixing layer as shown in Fig. 2.3.

The miscible Rayleigh-Taylor instability corresponds to the same initial conditions as the immiscible one. It follows a similar scenario, where small perturbations of the interface are amplified first linearly and then nonlinearly, growing into the developed turbulent mixing layer, as shown in Fig. 2.4. The important difference between the immiscible and miscible cases can be seen at small scales. The immiscible Rayleigh-Taylor turbulence leads to the formation of emulsion-like state with a multitude of small bubbles. On the contrary, the miscible Rayleigh-Taylor turbulence develops sharp gradients leading the enhanced diffusion at small scales.

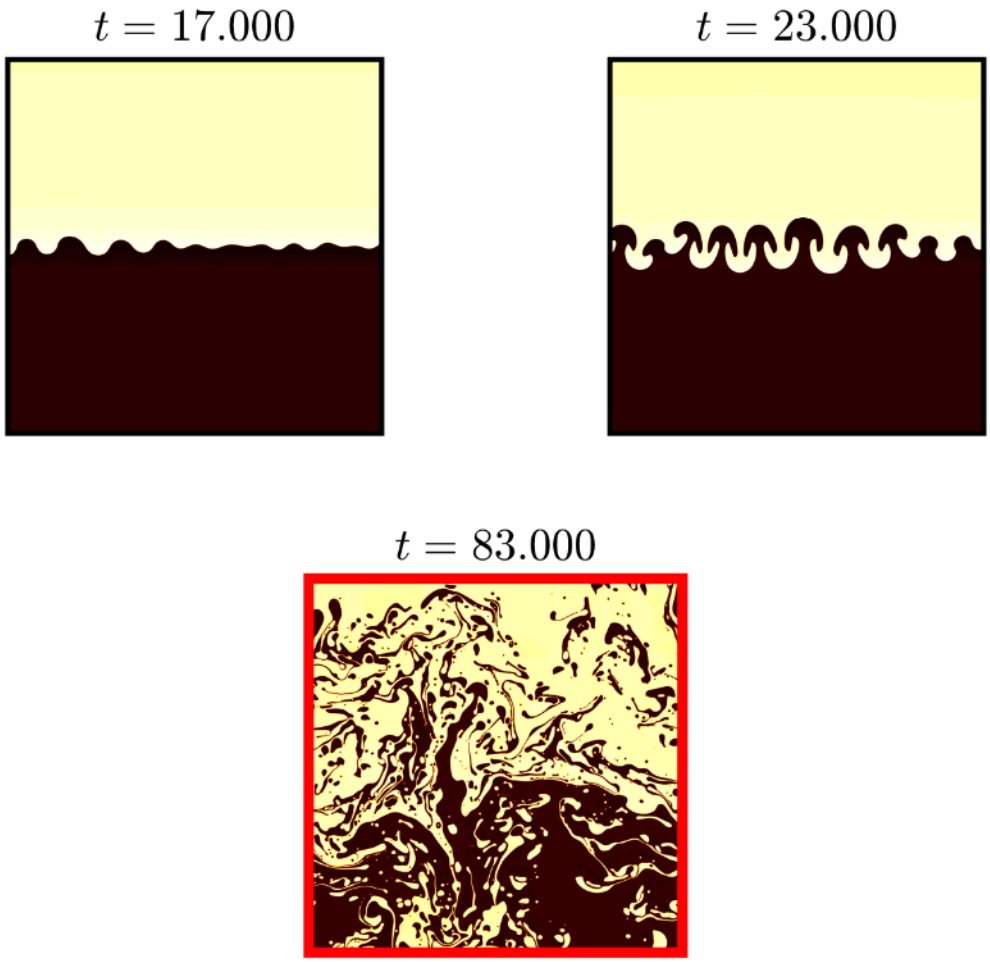

Figure 2.3: Mixing layer of the immiscible Rayleigh-Taylor turbulence, where the brown color corresponds to a lighter phase and the yellow color represents a heavier phase. The pictures show the phases in the same region for three different times: the initial linear growth, formation of nonlinear mushroom-like structures at intermediate times, and fully developed turbulent mixing at larger times. The images shown are clippings with size 2.000×1400 from simulations performed on grids 10.000×5.000 in lattice-Boltzmann units (lbu). This set of units is directly connected with the lattice Boltzmann method described in Chapter 3. A full picture of this simulations is shown in Chapters 3 and 5

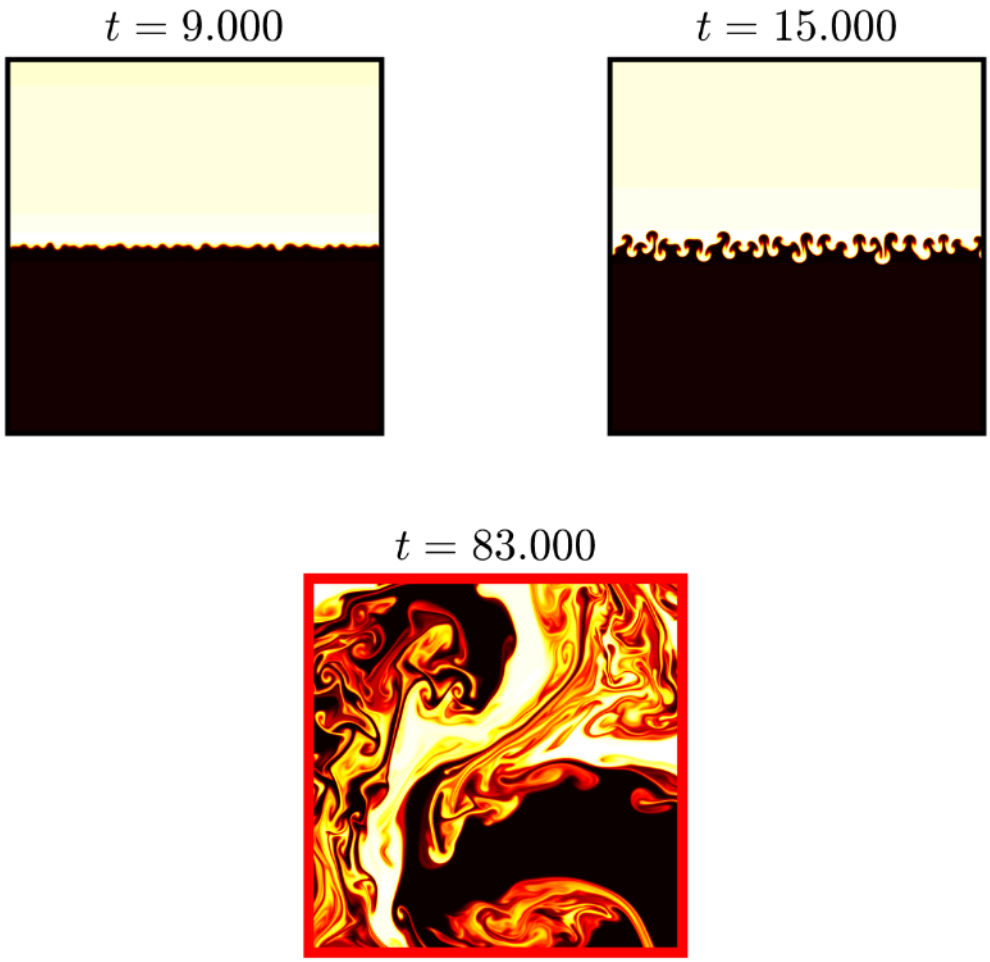

Figure 2.4: Mixing layer of the miscible Rayleigh-Taylor turbulence, where colors describe the fluid density; lighter colors representing the heavier fluid. The pictures show the densities in the same region for three different times: the initial linear growth, formation of nonlinear mushroom-like structures at intermediate times, and fully developed turbulent mixing at larger times. The images shown are clippings with size 2.000×1.400 from simulations performed on grids 10.000×5.000 in lattice-Boltzmann units (lbu). This set of units is directly connected with the lattice Boltzmann method described in Chapter 3. A full picture of this simulations is shown in Chapters 3 and 5

Chapter 3

The lattice-Boltzmann model

In this section, we approach numerical solutions for a class of multicomponent flows using some methods derived from statistical mechanics. Specifically, following mostly [55] and [98], we approach the basics of the Shan-Chen multicomponent method, which is one of the so-called lattice Boltzmann methods. The main objective is to show how to use these kind of methods to simulate the Rayleigh-Taylor systems described in the Chapter 2.

A basic lattice Boltzmann method (LBM) can be interpreted as a method that simulates fluid dynamics through the interactions of a set of fictitious particles located at the nodes of a uniform mesh in the fluid domain. These fictive particles interact through successive streaming and collision processes. Fluid properties, such as density and velocity, for example, emerge from interactions as moments of the distribution function in each node. In our study, we do a basic analysis of the Shan-Chen multicomponent method with the generalized Bhatnagar-Gross-Krook (BGK) collision operator model. The physical motivation involves the link between the multi-species Boltzmann equation and the Cahn-Hilliard-Navier-Stokes (CHNS) system.

In the first part of this chapter, we consider the case of simple fluids, describing the relationships between the classical Boltzmann equation and hydrodynamic equations. Thereafter, we introduce a particular numerical scheme for the Boltzmann equation, describing the so-called Lattice Boltzmann equation (LBE); and we show how to approach numerical solutions for the Navier-Stokes equations using this scheme. The same type of analysis is applied for the case of binary fluid systems, where we approach

the Boltzmann equation for a multi-species mixture, the Shan-Chen multicomponent method and its relation with the CHNS system. A parallelization scheme using CUDA C for the Shan-Chen method is also briefly discussed. At the end of the chapter, we show how to simulate the Boussinesq approximation for the Rayleigh-Taylor systems described in Chapter 2, giving details of the configuration required in the Shan-Chen method to simulate these systems.

3.1 From the Boltzmann equation to hydrodynamic models

This section is dedicated to the connection between the Boltzmann equation and the classical hydrodynamic equations in the context of simple fluids. This connection happens when the mean free path l_{mfp} of the system is small in comparison to the to the macroscopic length scale L. Under such conditions is possible to employ the so-called *Chapman-Enskog expansion*, to be described later. These ideas are also the basis for some numerical methods in fluid dynamics using the Boltzmann equation, some of these methods are discussed in the subsequent sections. All the equation described in this chapter are in a nondimensional form.

Consider a thermodynamic system out of equilibrium. Changes of some physical quantities of the system, such as and momentum and heat exchange, can be calculated using the Boltzmann equation, which gives on a macroscopic scale the macroscopic behaviour of a fluid. The Boltzmann equation is an integro-differential equation for the probability density function $f(\mathbf{x}, \mathbf{v}, t)$ in six-dimensional space of a particle position $\mathbf{x} \in \mathbb{R}^3$ and momentum $\mathbf{v} \in \mathbb{R}^3$ given by

$$\partial_t f + \nabla_{\mathbf{x}} f \cdot \mathbf{v} + \frac{\mathbf{F}}{\rho} \cdot \nabla_{\mathbf{v}} f = Q(f, f), \tag{3.1}$$

where $Q(f, f)$ is collision integral, $\mathbf{F}$ is the body force, ρ is macroscopic mass density of the system, and $\nabla_{\mathbf{x}}$ and $\nabla_{\mathbf{v}}$ are gradients with respect to the position $\mathbf{x}$ and velocity $\mathbf{v}$ coordinates, respectively.

It can be shown that the collision integral $Q(f, f)$ has at least five invariants [98],

i.e., a set of functions $\xi_k,\ k = 1, 2, 3, 4, 5$, satisfying

$$\int \xi_k(\mathbf{v}) Q(f, f) d\mathbf{v} = 0, \tag{3.2}$$

which are $\xi_1 = 1$, $(\xi_2, \xi_3, \xi_4) = \mathbf{v}$ and $\xi_5 = |\mathbf{v}|^2$, with the integration being performed in $\mathbb{R}^2$. A general collision invariant can be written as linear combinations of the functions ξ_k. The invariants are associated to some important macroscopic quantities in the system

$$\text{mass density:} \qquad \int f d\mathbf{v} = \rho, \tag{3.3}$$

$$\text{mean momentum:} \qquad \int f \mathbf{v} d\mathbf{v} = \rho \mathbf{u}, \tag{3.4}$$

$$\text{total energy density:} \qquad \frac{1}{2} \int f |\mathbf{v}|^2 d\mathbf{v} = \rho E. \tag{3.5}$$

A set of conservation laws for each of this quantities can be obtained multiplying the Boltzmann equation (3.1) by a collision invariant and subsequently integrating with respect to the velocity. For example, for $\xi_k = 1$, we have

$$\frac{\partial}{\partial t} \left(\int f d\mathbf{v} \right) + \nabla_{\mathbf{x}} \cdot \left(\int f \mathbf{v} d\mathbf{v} \right) + \frac{\mathbf{F}}{\rho} \cdot \left(\int \nabla_{\mathbf{v}} f d\mathbf{v} \right) = \int Q(f, f) d\mathbf{v} = 0 \quad \Rightarrow \tag{3.6}$$

$$\Rightarrow \quad \partial_t \rho + \nabla \cdot (\rho \mathbf{u}) = 0, \tag{3.7}$$

obtaining to the continuity equation. Similarly, if we take first moment of the Boltzmann equation we find

$$\frac{\partial (\rho \mathbf{u})}{\partial t} + \nabla \cdot \Pi = \mathbf{F}, \tag{3.8}$$

where Π is the *momentum flux tensor* given by

$$\Pi = \int f \mathbf{v} \otimes \mathbf{v} d\mathbf{v}. \tag{3.9}$$

By splitting the particle velocity $\mathbf{v} = \mathbf{u} + \mathbf{w}$, where $\mathbf{w}$ is the relative velocity, we obtain

$$\Pi = \rho \mathbf{u} \otimes \mathbf{u} + \int f \mathbf{w} \otimes \mathbf{w} d\mathbf{v}. \tag{3.10}$$

Thus, the equation (3.8) becomes the *Cauchy momentum equation*

$$\frac{\partial (\rho \mathbf{u})}{\partial t} + \nabla \cdot (\rho \mathbf{u} \otimes \mathbf{u}) = \nabla \cdot \mathbf{P} + \mathbf{F}. \tag{3.11}$$

However, in this equation we do not know explicitly the *stress tensor*

$$\mathbf{P} = -\int (\mathbf{w} \otimes \mathbf{w}) f d\mathbf{v}. \tag{3.12}$$

We can approximate this stress tensor using an explicit approximation for the distribution function f. This can be done analysing the approach to equilibrium of the system.

Boltzmann showed in 1872 [98] that the entropy,

$$H(t) = \int f(\mathbf{x}, \mathbf{v}, t) \ln(f(\mathbf{x}, \mathbf{v}, t)) d\mathbf{x} d\mathbf{v}, \tag{3.13}$$

where f is any function satisfying the Boltzmann equation (3.1), fulfills the equation

$$\frac{dH}{dt} \leq 0. \tag{3.14}$$

The equality in (3.14) holds for a distribution $f^{(eq)}$ given by

$$f^{(eq)}(\rho, \mathbf{u}, \mathbf{v}, T) = \rho \left(\frac{1}{2\pi RT} \right)^{3/2} e^{-|\mathbf{v}-\mathbf{u}|^2/(2RT)}, \tag{3.15}$$

where T is the temperature and R is the ideal gas constant. This is the so-called the *local equilibrium distribution* of the system. A direct calculation using (3.1) also shows that $Q(f^{(eq)}, f^{(eq)}) = 0$.

Due to the complicated form of the collision integral in real physical systems, some alternative simpler expressions have been proposed to approximate such integral [98]. The collision operators commonly used in numerical methods for the Boltzmann equation are based on the Bhatnagar-Gross-Krook (BGK) collision operator:

$$\Omega(f, f) = -\frac{1}{\tau}(f - f^{(eq)}), \tag{3.16}$$

where τ is known as the *relaxation time*, which determines the speed of the convergence to the equilibrium state of the system. The relaxation time is an approximation of the typical collision time, i.e., the average time lapse between two subsequent collisions. This parameter can be assumed to be contant for incompressible fluids with contant viscosity [55]. The BGK formula reflects the tendency of $f(\mathbf{x}, \mathbf{v}, t)$ towards the local equilibrium distribution $f^{(eq)}$ due to the particle collisions in the system.

If we approximate $f \simeq f^{(eq)}$, the equation (3.11) becomes the *Euler momentum equation*

$$\frac{\partial(\rho \mathbf{u})}{\partial t} + \nabla \cdot (\rho(\mathbf{u} \otimes \mathbf{u})) = \nabla p + \mathbf{F}, \tag{3.17}$$

where p is the pressure given by

$$p = \frac{1}{3} \int |\mathbf{w}|^2 f^{(eq)}(\mathbf{x}, \mathbf{v}, t) d\mathbf{v}. \tag{3.18}$$

The fact that the Euler equation is obtained considering a particle distribution f at equilibrium indicates that the effects of the viscous dissipation and heat diffusivity are associated with the *non-equilibrium* part of the distribution, i.e., $f - f^{eq}$ [55]. A more general approximation for f, which accounts the non-equilibrium effects, is obtained using the *Chapman-Enskog analysis*. It consists in the expansion of f as a perturbation around f^{eq} given by

$$f = f^{eq} + \sum_{k=1}^{\infty} \varepsilon^k f^{(k)}, \tag{3.19}$$

where ε labels each term's order and is often stated in the literature as proportional to the Knudsen number $\mathrm{Kn} = \ell_{mfp}/L$ of the system [55], defined as the ratio between the mean free path ℓ_{mfp} and the representative physical length scale L. For $\mathrm{Kn} \to 0$ the system is dominated by collisions and the particle distribution is approximately equilibrium [59], characterizing the behavior described by the Euler equation (3.17).

Analogously, the operators ∂_t and $\nabla_{\mathbf{x}}$ have to be defined such that they are consistent with the conservation laws (3.11) and (3.7), which leads to the expansions

$$\partial_t = \sum_{k=1}^{\infty} \varepsilon^k \partial_t^{(k)}, \qquad \nabla_{\mathbf{x}} = \sum_{k=1}^{\infty} \varepsilon^k \nabla_{\mathbf{x}}^{(k)} \tag{3.20}$$

To the first order approximation $f \approx f^{eq} + \varepsilon f^{(1)}$, we obtain the *Navier-Stokes model* with the following stress tensor

$$\mathbf{P} \simeq -p\mathbf{I} + \frac{\eta}{2}(\nabla \mathbf{u} + \nabla \mathbf{u}^T) \tag{3.21}$$

from the equation (3.12), where η is the dynamic viscosity. Thus, from a solution of the Boltzmann equation for a given system we can derive a solution for the Navier-Stokes equations for the same case.

The collision invariant $\xi_5(\mathbf{v}) = |\mathbf{v}|^2$ is related to the conservation law for the total energy density of the system (3.5) [55, 59], but in this thesis we will not discuss this equation, since we are considering only isothermal and incompressible systems without chemical reactions.

Shifted hydrodynamics

It is possible to include the forcing term in (3.1) into the collision operator (3.16) defining a generalized BGK collision term, obtained by moving the force term in (3.1)

to the right-hand side as follows

$$C(f) = Q(f,f) - \frac{\mathbf{F}}{\rho}\cdot\nabla_{\mathbf{v}} f \tag{3.22}$$

$$\simeq -\frac{1}{\tau}(f - f^{(eq)}) - \frac{\mathbf{F}}{\rho}\cdot\nabla_{\mathbf{v}} f. \tag{3.23}$$

Consider the following approximation

$$C(f) \simeq C^e(f) = -\frac{1}{\tau}(f - f^{(eq)}) - \frac{\mathbf{F}}{\rho}\cdot\nabla_{\mathbf{v}} f^{(eq)}, \tag{3.24}$$

where we evaluate the forcing term as acting on the local equilibrium. This approximation has no significant impact on the mass and momentum transfer to the fluid by the force field [89]. In fact, consider the following identity [89]

$$f\left(t,\mathbf{x},\mathbf{v}+\tau\frac{\mathbf{F}}{\rho}\right) = \left[\exp\left(\tau\frac{\mathbf{F}}{\rho}\cdot\nabla_{\mathbf{v}}\right)\right] f(t,\mathbf{x},\mathbf{v}) \tag{3.25}$$

where the operator in the right hand side is defined, up to second order, as follows

$$\left[\exp\left(\tau\frac{F_a}{\rho}\partial_{v_a}\right)\right] f^{(eq)} = \left(1 + \tau\frac{F_a}{\rho}\partial_{v_a} + \frac{\tau^2}{2}\frac{F_a}{\rho}\partial_{v_a}\frac{F_b}{\rho}\partial_{v_b}\right) f^{(eq)} + O(Fr^2) \tag{3.26}$$

where F_a and F_b are component of the force $\mathbf{F}$ and we have defined the local *Froude* number as [55]

$$Fr \equiv \left|\frac{F_a}{\rho}\frac{\partial_{v_a} f^{(eq)}}{f^{(eq)}}\right|. \tag{3.27}$$

Consequently, we can write

$$(1+\tau F_a\partial_{v_a}) f^{(eq)} \sim \left[\exp\left(\tau\frac{F_a}{\rho}\partial_{v_a}\right)\right] f^{(eq)} - \frac{\tau^2}{2}\frac{F_a}{\rho}\partial_{v_a}\frac{F_b}{\rho}\partial_{v_b} f^{(eq)}. \tag{3.28}$$

Thus, the shifted collision operator (3.24) can be written as

$$C^e(f) = -\frac{1}{\tau}\left(f(v_a) - f^{(eq)}\left(v_a + \tau\frac{F_a}{\rho}\right)\right) + \frac{\tau}{2}\frac{F_a}{\rho}\partial_{v_a}\frac{F_b}{\rho}\partial_{v_b} f^{(eq)} + O(Fr^2) \tag{3.29}$$

where, for simplicity, we omit the dependency of $(t,\mathbf{x})$ in the distributions . In practice, what is actually used is the following relation

$$C_S^e(f) = -\frac{1}{\tau}\left(f(\mathbf{v}) - f^{(eq)}\left(\mathbf{v} + \tau\frac{\mathbf{F}}{\rho}\right)\right), \tag{3.30}$$

i.e.,

$$C_S^e(f) \sim C^e(f) - \frac{\tau}{2}\frac{F_a}{\rho}\partial_{v_a}\frac{F_b}{\rho}\partial_{v_b} f^{(eq)}. \tag{3.31}$$

This shifted equilibrium include the effects of diffusion in velocity space to the second order in the Froude number. It can be check by direct integration that the diffusion term in (3.29) has no impact on the mass and conservation momentum [89].

The generalized collision operator (3.30) gives an important simplification in the treatment of the forcing term in some numerical algorithms for the Boltzmann equation, as we show in the next sections of this chapter.

We refer the interested readers to [55, 89, 98, 7] for more details on the derivation of fluid dynamic equations using Chapman-Enskog analysis.

3.1.1 The lattice-Boltzmann method for simple fluids

The connection between Boltzmann and Navier-Stokes equations is the essence of the so-called *lattice-Boltzmann method* (LBM). In this method the basic quantity is the *discrete-velocity distribution function* $f_i(x,t)$, often called the *particle populations*, it represents the density of particles with velocity $\mathbf{c}_i$ at position $\mathbf{x}$ and time t. Analogously, the mass density and momentum density $\rho\mathbf{u}$ at (x,t) can be found through weighted sums known as moments of f_i as

$$\rho(x,t) = \sum_i f_i(\mathbf{x},t), \tag{3.32}$$

$$\rho\mathbf{u}(\mathbf{x},t) = \sum_i \mathbf{c}_i f_i(\mathbf{x},t). \tag{3.33}$$

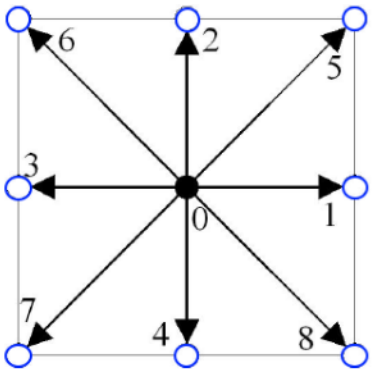

Figure 3.1: Lattice velocities for D2Q9 scheme.

The main difference bewteen f_i and the continuous distribution function f is that all of the argument variables of f_i are discrete, with the subscript i refering to a finite

discrete set of velocities $\mathbf{c}_i$. The points $\mathbf{x}$ at which f_i is defined are positioned as a square lattice in space, with lattice spacing Δx and f_i is defined only in a discrete set of times separated by a time step Δt. The time step Δt and lattice spacing Δx respectively represent a time resolution and a space resolution in any set of units. A most common choice in the LB literature is the lattice-Boltzmann units (LBU), a simple artificial set of units scaled such that $\Delta t = 1$ and $\Delta x = 1$. The conversion between LBU and physical units can be done similarly as converting between two general sets of physical units.

By discretizing the Boltzmann equation in velocity space, physical space, and time, we obtain the *discrete Boltzmann equation*

$$f_i(\mathbf{x} + \mathbf{c}_i\Delta t, t + \Delta t) = f_i(\mathbf{x}, t) + \Omega_i(\mathbf{x}, t). \tag{3.34}$$

This equation expresses that a particle $f_i(\mathbf{x}, t)$ moves with velocity $\mathbf{c}_i$ to the nearest neighbors after a time step Δt. One of the most used velocity sets is the so-called D2Q9 scheme, where each particle is allowed to have nine velocities $\mathbf{c}_0, \ldots, \mathbf{c}_8$. These velocities are given by the vectors $(0, 0)$, $(\pm c, 0)$, $(0, \pm c)$ and $(\pm c, \pm c)$ with $c = \Delta x/\Delta t$, such that a particle stays at the same or moves to a neighboring lattice point at a single time step. In the next developments and in all simulations presented we assume the lattice Boltzmann units. This choice of units offers a reasonable numerical stability in the numerical simulations and also simplify the implementation of the lattice Boltzmann algorithms, as we will see later.

The discrete version of the BGK-collision operator (3.16) is given by Ω_i defined as

$$\Omega_i(f, f) = -\frac{f_i - f_i^{(eq)}}{\tau}. \tag{3.35}$$

The equilibrium distribution is calculated by maximizing the entropy [98]

$$S(\rho, \mathbf{u}) = -\sum_i f^{eq}(\rho, \mathbf{u}) \ln\left(\frac{f^{eq}(\rho, \mathbf{u})}{w_i}\right), \tag{3.36}$$

for given constraints, which for case under consideration are the mass and momentum densities given by (3.32) and (3.33), i.e.,

$$\sum_i f_i^{(eq)} = \sum_i f_i = \rho, \tag{3.37}$$

$$\sum_i \mathbf{c}_i f_i^{(eq)} = \sum_i \mathbf{c}_i f_i = \rho\mathbf{u}. \tag{3.38}$$

The weighting $1/w_i$ in the entropy formula will lead to equilibrium distributions of the form $f_i^{(eq)} = w_i e^{h(\rho,\mathbf{u},c_i)}$, implying $S = 0$ for $f_i^{(eq)} = w_i$. The functional

$$\overline{S} = S + \overline{A}(\rho, \mathbf{u})\rho + \overline{B}(\rho, \mathbf{u}) \cdot \mathbf{u}, \tag{3.39}$$

incorporates the constraints by the coupling with the Lagrange multipliers $\overline{A}$ and $\overline{B}$. Expanding $\overline{A}$ and $\overline{B}$ up to second order in $\mathbf{u}$ and using the symmetry of the D2Q9, we obtain as a minimum of $\overline{S}$ the following distribution:

$$f_i^{(eq)}(\rho, \mathbf{u}) = \rho w_i \left(1 + \frac{3\mathbf{c}_i \cdot \mathbf{u}}{c^2} + \frac{9(\mathbf{c}_i \cdot \mathbf{u})^2}{2c^4} - \frac{3\mathbf{u} \cdot \mathbf{u}}{2c^2}\right), \tag{3.40}$$

where the weights w_i are associated to the velocity set D2Q9. Note that the equilibrium distribution is a function of the density ρ and velocity $\mathbf{u}$ only. The weights are connected to the velocity components $\mathbf{c}_i = (c_i^1, c_i^2)$ by the conditions

$$\sum_i w_i c_i^a c_i^b = c_s^2 \delta_{ab}, \quad \sum_i w_i c_i^a c_i^b c_i^c c_i^d = c_s^4 \left(\delta_{ab}\delta_{cd} + \delta_{ad}\delta_{bc} + \delta_{ac}\delta_{bd}\right) \quad \text{for} \quad a, b, c, d = 1, 2, \tag{3.41}$$

where δ_{ab} is the Kronecker delta. The simplified equilibrium distribution (3.40) and the discrete velocity space D2Q9 are sufficient to obtain the correct macroscopic conservation laws in two-dimensions for several applications [55].

The connection between LBM and the Navier-Stokes equation is given by the Chapman-Enskog expansion (3.19) and (3.20). Using this expansion, the kinematic shear viscosity is associated to the relaxation time by the equation

$$\nu = c_s^2 \left(\tau - \frac{1}{2}\right), \tag{3.42}$$

where $c_s = c/\sqrt{3}$ is the speed of sound in LBU. The bulk viscosity will be given by $\nu_B = 2\nu/3$. In addition, the momentum flux tensor $\mathbf{P}$ is approximated from f_i as

$$\mathbf{P} \simeq \left(1 - \frac{1}{2\tau}\right) \sum_i (\mathbf{c}_i \otimes \mathbf{c}_i) f_i \tag{3.43}$$

analogously to the formula (3.12) in the continuum case. The viscous contribution $\boldsymbol{\sigma}$ to the momentum flux tensor is approximated as

$$\boldsymbol{\sigma} \simeq \left(1 - \frac{\Delta t}{2\tau}\right) \sum_i (\mathbf{c}_i \otimes \mathbf{c}_i)(f_i - f_i^{(eq)}) = \rho\nu(\nabla\mathbf{u} + \nabla\mathbf{u}^T). \tag{3.44}$$

Using the BGK approximation in the equation (3.34), we obtain the lattice BGK equation:

$$f_i(\mathbf{x}+\mathbf{c}_i, t+1) = f_i(\mathbf{x}, t) - \frac{1}{\tau}\left(f_i(\mathbf{x}, t) - f_i^{(eq)}(\rho, \mathbf{u})\right). \tag{3.45}$$

This equation can be decomposed into two parts that are performed in different time steps:

- The first part is the collision (or relaxation), where we compute

$$f_i^*(\mathbf{x}, t) = f_i(\mathbf{x}, t) - \frac{1}{\tau}\left(f_i(\mathbf{x}, t) - f_i^{(eq)}(\rho, \mathbf{u})\right) \tag{3.46}$$

  where f_i^* represents the distribution after collisions.

- The second part is the propagation (or streaming), where we compute

$$f_i(\mathbf{x}+\mathbf{c}_i, t+1) = f_i^*(\mathbf{x}, t) \tag{3.47}$$

The simplest way to initialize the populations at the initial time $t = 0$ is to set

$$f_i(\mathbf{x}, t=0) = f_i^{(eq)}(\rho(\mathbf{x}, t=0), \mathbf{u}(\mathbf{x}, t=0)). \tag{3.48}$$

The LBM algorithm consists of a cyclic sequence of substeps, with each cycle corresponding to one time step [55]. Specifically, the following substeps shows the necessary information to set up an LBM computer code:

- For given initial values of density $\rho(\mathbf{x}, t)$ and velocity $\mathbf{u}(\mathbf{x}, t)$ calculate the equilibrium distribution $f_i^{(eq)}$ from the formula (3.40) and set $f_i = f_i^{(eq)}$.

- Perform collision according to (3.46).

- Perform propagation according to (3.47).

- Calculate from the propagation process new values of $\rho(\mathbf{x}, t)$ and $\mathbf{u}(\mathbf{x}, t)$ using the definitions (3.32) and (3.33).

- The next time step starts from the calculations of the new equilibrium distributions. The subsequent evolution of the system is done by repeating the operations of this algorithm until the last time step or convergence has been reached.

The external forces in the discrete Boltzmann equation are generally taken into account introducing a discrete force F_i, which is a generalization of the forcing term $\frac{\mathbf{F}}{\rho} \cdot \nabla_{\mathbf{v}} f$ in (3.1). Thus:

$$f_i(\mathbf{x} + \mathbf{c}_i, t + 1) = f_i(\mathbf{x}, t) + \Omega_i(\mathbf{x}, t) + F_i(\mathbf{x}, t) \tag{3.49}$$

In particular, we demand that the discrete force should conserve the moments of the term $\frac{\mathbf{F}}{\rho} \cdot \nabla_{\mathbf{v}} f$, i. e.,

$$\sum_i F_i = \int \frac{F_a}{\rho} \partial_{v_a} f d\mathbf{v} = 0 \tag{3.50}$$

$$\sum_i F_i c_i^a = \int v_a \frac{F_b}{\rho} \partial_{v_b} f d\mathbf{v} = F_a \tag{3.51}$$

$$\sum_i F_i c_i^a c_i^b = \int v_a v_b \frac{F_c}{\rho} \partial_{v_c} f d\mathbf{v} = F_a u_b + u_a F_b \tag{3.52}$$

where the index $a, b, c = 1, 2$ are indications of the Cartesian components of the vectors. Using the shifted hydrodynamics approach, the forcing term can be inserted in the expression of the equilibrium distribution (3.40) using the generalized BGK operator (3.30) as follows

$$f_i(\mathbf{x} + \mathbf{c}_i, t + 1) - f_i(\mathbf{x}, t) = -\frac{1}{\tau} \left[f_i(\mathbf{x}, t) - f_i^{(eq)} \left(\rho, \mathbf{u} + \frac{\tau \mathbf{F}}{\rho} \right) \right], \tag{3.53}$$

this is the so-called Shan-Chen forcing scheme [89]. This is the forcing scheme we adopt in the next sections.

To treat the boundaries, we assume that the whole computational domain is divided into many uniform voxels, which are occupied by either solid or fluid, with the variables defined at the voxel centers. In the applications of this theses we use the bounce-back boundary for the non-slip boundary condition. In this method we allow the distribution $f_i(\mathbf{x}_{fluid}, t)$, which belongs to the fluid grid at $\mathbf{x}_{fluid}$ and moves toward the solid grid at $\mathbf{x}_{solid}$ in the $\mathbf{c}_i$ direction, to bounce back at the same time step to update [62]

$$f_{i'}(\mathbf{x}_{fluid}, t) = f_{i'}(\mathbf{x}_{solid}, t) = f_i(\mathbf{x}_{solid}, t) = f_i(\mathbf{x}_{fluid}, t), \tag{3.54}$$

where i' is the index of $\mathbf{c}_{i'}$ opposite to $\mathbf{c}_i$. In this thesis, we consider only bounce-back and periodic boundary conditions.

3.2 From the multi-species Boltzmann equation to the Cahn-Hilliard-Navier-Stokes system

This section is dedicated to extending the theory described in the previous sections to the context of incompressible multicomponent fluids without phase changes.

For a binary mixture, a natural generalization of the lattice Boltzmann method comes from the analysis of the multi-species Boltzmann equation [47, 7]. In the two dimensional case, this equation describes the evolution of a vector distribution $f = (f^A, f^B)$ where each entry $f^s(\mathbf{x}, \mathbf{v}, t)$ represents the distribution of the specie $s = A, B$ at time t in a point $(\mathbf{x}, \mathbf{v})$ on the phase space. The Boltzmann equation for the multi-species system is given by [7]

$$\partial_i f^A + \mathbf{v} \cdot \nabla_{\mathbf{x}} f^A + \frac{\mathbf{F}_A}{\rho_A} \cdot \nabla_{\mathbf{v}} f_A = \Omega_{AA}(f^A, f^A) + \Omega_{AB}(f^A, f^B), \tag{3.55}$$

$$\partial_i f^B + \mathbf{v} \cdot \nabla_{\mathbf{x}} f^B + \frac{\mathbf{F}_B}{\rho_B} \cdot \nabla_{\mathbf{v}} f_B = \Omega_{BB}(f^B, f^B) + \Omega_{BA}(f^B, f^A) \tag{3.56}$$

where $\Omega_{ss'}(f^s, f^{s'})$ represents the effects of the collision between the species s and s' and $\mathbf{F}_A$ and $\mathbf{F}_B$ are forces acting on the components A and B respectively. The terms $\Omega_{AA}(f^A, f^A)$ and $\Omega_{BB}(f^B, f^B)$ accounts for the tendencies to the local equilibrium states and phase transitions in each component. The terms $\Omega_{AB}(f^A, f^B)$ and $\Omega_{BA}(f^B, f^A)$ are associated to the interactions between different components; that can result in attraction, repulsion or no interaction. In this section we consider a binary system without phase changes.

Analogously to the previous section, we define some important macroscopic quantities for system:

$$\text{bare mass density} \quad \rho_s = \int f^s d\mathbf{v}, \tag{3.57}$$

$$\text{bare momentum density} \quad \rho_s \mathbf{u}_s = \int f^s \mathbf{v} d\mathbf{v} \tag{3.58}$$

$$\text{bare momentum flux tensor} \quad \mathbf{S}_s = \int \mathbf{v} \otimes \mathbf{v} f_s d\mathbf{v} \tag{3.59}$$

$$\text{total mass density} \quad \rho = \rho_A + \rho_B, \tag{3.60}$$

$$\text{total momentum density} \quad \rho \mathbf{u} = \rho_A \mathbf{u}_A + \rho_B \mathbf{u}_B, \tag{3.61}$$

$$\text{order parameter} \quad \phi = \rho_A - \rho_B \tag{3.62}$$

$$\text{total momentum flux tensor} \quad \mathbf{S} = \mathbf{S}_A + \mathbf{S}_B \tag{3.63}$$

In a mixture model, for each specie, there are a conservation laws for the mass densities and total momentum [47]. They are obtained by multiplying the collision term with $\xi = \left(1, \mathbf{v}, \frac{1}{2}|\mathbf{v}|^2\right)$ and integrating with respect to $\mathbf{v}$. In a system with incompressible components with no chemical reaction with a constant temperature, some of the most import conservation laws are given by

$$\begin{aligned}
\partial_t \rho_s + \nabla \cdot (\rho_s \mathbf{u}) &= \nabla \cdot \mathbf{J}^{(s)}, \quad s = A, B, \\
\partial_t \phi + \nabla \cdot (\phi \mathbf{u}) &= \nabla \cdot \mathbf{J}^{(\phi)}, \\
\partial_t \rho + \nabla \cdot (\rho \mathbf{u}) &= 0, \\
\partial_t (\rho \mathbf{u}) + \nabla \cdot (\rho \mathbf{u} \otimes \mathbf{u}) &= \nabla \cdot \mathbf{S} + \mathbf{F},
\end{aligned}$$

where $\mathbf{F} = \mathbf{F}_A + \mathbf{F}_B$ and the diffusive currents verify $\mathbf{J}^{(\phi)} = -2\mathbf{J}^{(B)} = 2\mathbf{J}^{(A)} = 2\rho_A(\mathbf{u} - \mathbf{u}_A)$ by the Gibbs-Duhem equation [58]. An important difference in the context of multicomponent systems is in the equilibrium distributions for the components of the system. It can be show that if

$$\Omega_{AA}(f^A, f^A) = \Omega_{AB}(f^A, f^B) = 0, \tag{3.64}$$

$$\Omega_{BB}(f^B, f^B) = \Omega_{BA}(f^B, f^A) = 0, \tag{3.65}$$

then f^A and f^B are Maxwellians with common velocity $\mathbf{u}$ and temperature T [7], i.e.,

$$f^{s(eq)}(\rho_s, \mathbf{u}, \mathbf{v}, T) = \rho_s \left(\frac{1}{2\pi RT}\right)^{3/2} e^{-|\mathbf{v}-\mathbf{u}|^2/(2RT)}, \text{ for } s = A, B. \tag{3.66}$$

We can also apply the Chapman-Enskog expansion for binary mixtures expanding f^s as a perturbation around (3.66) as

$$f^s = f^{s(eq)} + \sum_{k=1}^{\infty} \varepsilon^k f^{s(k)} \tag{3.67}$$

where ε labels each term's order in the Knudsen number Kn of the component s, which we assume to be the same for both components, for the sake of simplicity. The multiscale expansion is also applied the operators ∂_t and $\nabla_{\mathbf{x}}$, analogously to (3.20).

In the limit $\mathrm{Kn} \to 0$, the collision terms vanishes leading to the Euler limit of the system [47, 7]. In this limit $J^{(A)} = J^{(B)} = 0$ and $\nabla \cdot \mathbf{S} \to -\nabla p$, where p is the hydrostatic pressure given by $p = c_s^2 \rho$ with c_s^2 being the speed of sound. In this regime the mixture behaves like a mixture of ideal gases without interactions.

To model the non-equilibrium effects, we consider $f^s \simeq f^{s(eq)} + \varepsilon f^{s(1)}$. Analogously to the cases of the simple fluids, we have

$$\mathbf{S} \simeq -p\mathbf{I} + \eta(\nabla\mathbf{u} + (\nabla\mathbf{u})^T). \tag{3.68}$$

where η is the dynamic viscosity of the system. The effects of the self interactions of the components, represented by the terms $\Omega_{AA}(f^A, f^A)$ and $\Omega_{BB}(f^B, f^B)$, are approximated using the BGK collision operator given by

$$\Omega_{ss}(f^s, f^s) = -\frac{1}{\tau}(f^s - f^{s(eq)}) \tag{3.69}$$

where τ is the relaxation time. For effects of the interactions between components, represented by $\Omega_{A,B}(f^A, f^B)$ and $\Omega_{B,A}(f^B, f^A)$, we can use the approximations given by the so-called Shan-Chen (SC) intermolecular force $\mathbf{F}_s^{SC}$, which assumes the following hypothesis between the points in the fluid domain [55]:

- The intermolecular forces act between pairs of molecules and are additive.
- The magnitude of intermolecular forces between fluid elements at $\mathbf{x}$ and $\overline{\mathbf{x}}$ is proportional to the product of the densities in each point, i.e., $\rho_s(\mathbf{x})\rho_{\overline{s}}(\overline{\mathbf{x}})$.
- Interaction is a strong function of the distance between the elements of the fluid.
- A kernel function $G_{s\overline{s}}(\mathbf{x}, \overline{\mathbf{x}})$ carries the dependence of the spatial dependence of the force.

A continuous function that fulfills the mentioned requirements is given by

$$\mathbf{F}_s^{SC}(\mathbf{x}) = -\int (\overline{\mathbf{x}} - \mathbf{x}) G_{s\overline{s}}(\mathbf{x}, \overline{\mathbf{x}}) \rho_s(\mathbf{x}) \rho_{\overline{s}}(\overline{\mathbf{x}}) d\overline{\mathbf{x}}, \tag{3.70}$$

with $\overline{s} = B$ for $s = A$ and vice versa. In the next subsetion, we introduce a discrete models for (3.70). For large values of ρ_s is common to use an effective density or *pseudopotential* ψ_s instead of the densities ρ_s in the expression (3.70). A common form for the pseudopotential ψ_s is given by [55]

$$\psi_s(\rho_s) = \rho_{s0}[1 - \exp(\rho_s/\rho_{s0})] \text{ for } s = A, B, \tag{3.71}$$

where ρ_{s0} is a reference density. The reason for ψ_s is rather than ρ_s is the possibility of numerical instabilities for large values of ρ_s [89], which is not the case for the applications in this thesis.

In the Shan-Chen method, the effect of the interaction between components is accounted by the introduction of extra forcing terms $\mathbf{F}_A^{SC}(\mathbf{x})$ and $\mathbf{F}_B^{SC}(\mathbf{x})$ in the equations (3.55) and (3.56). By this way, we obtain [82, 5]

$$\mathbf{J}^{(A)} = \frac{\rho_A \rho_B}{\rho}\left[\nu\left(\frac{\nabla\rho_A}{\rho_A} - \frac{\nabla\rho_B}{\rho_B}\right) - \tau\left(\frac{\mathbf{F}_A}{\rho_A} - \frac{\mathbf{F}_B}{\rho_B}\right)\right] = -\mathbf{J}^{(B)}, \tag{3.72}$$

and the global momentum equation will be given by

$$\partial_t(\rho\mathbf{u}) + \nabla\cdot(\rho\mathbf{u}\otimes\mathbf{u}) = -\nabla p + \nabla\cdot(\rho\nu(\nabla\mathbf{u} + (\nabla\mathbf{u})^T)) + \mathbf{F}, \tag{3.73}$$

where $\mathbf{F}$ includes the Shan-Chen force $\mathbf{F}^{(SC)} = \mathbf{F}_A^{SC} + \mathbf{F}_B^{SC}$ and other external forces. The Shan-Chen force can also be incorporated into some suitable stress tensor $\mathbf{P}$ verifying the relation

$$\nabla\cdot\mathbf{P} = \nabla p - \mathbf{F}^{(SC)}. \tag{3.74}$$

3.2.1 Lattice-Boltzmann method for binary mixtures without phase changes

The lattice Boltzmann equation for each component is written as

$$f_i^A(x + c_i, t+1) = f_i^A(x,t) + \Omega_i^{AA} + \Omega_i^{AB}, \tag{3.75}$$

$$f_i^B(x + c_i, t+1) = f_i^B(x,t) + \Omega_i^{BB} + \Omega_i^{BA}. \tag{3.76}$$

where the terms Ω_i^{AA} and Ω_i^{BB} accounts for the self-interactions of the system; and the terms Ω_i^{AB} and Ω_i^{BA} are related to the interaction between the different components. The densities of each component (bare densities) and common velocity of the fluid are defined as

$$\rho_s(\mathbf{x},t) = \sum_i f_{is}(\mathbf{x},t), \tag{3.77}$$

$$\mathbf{u}(\mathbf{x},t) = \frac{\sum_{s,i} f_i^s(\mathbf{x},t)\mathbf{c}_i/\tau_s}{\sum_s \rho_s(\mathbf{x},t)/\tau_s} \tag{3.78}$$

For the self-interaction term we can employ the BGK approximation

$$\Omega_i^{ss}(\mathbf{x},t) = -\frac{1}{\tau_s}(f_i^s(\mathbf{x},t) - f_i^{s(eq)}(\rho_s,\mathbf{u})), \tag{3.79}$$

describing the relaxation towards the local equilibrium distribution $f_i^{s(eq)}$ for each component defined, analogously to the single component case, as

$$f_i^{s(eq)}(\rho_s,\mathbf{u}) = \rho_s w_i\left(1 + \frac{3\mathbf{c}_i\cdot\mathbf{u}}{c^2} + \frac{9(\mathbf{c}_i\cdot\mathbf{u})^2}{2c^4} - \frac{3\mathbf{u}\cdot\mathbf{u}}{2c^2}\right). \tag{3.80}$$

Note that the velocity in the equilibrium distribution is the same for all components of the system, analogous to the formula (3.66) for the continuous case.

The external forces $\mathbf{F}^s$ acting on the component s are taken into account by using the Shan-Chen forcing scheme

$$f_i^s(\mathbf{x}+\mathbf{c}_i, t+1) - f_i^s(\mathbf{x}, t) = -\frac{1}{\tau_s}\left[f_i^s(\mathbf{x}, t) - f_i^{s(eq)}\left(\rho, \mathbf{u} + \frac{\tau_s \mathbf{F}_s}{\rho_s}\right)\right]. \tag{3.81}$$

The forcing term $\mathbf{F}_s$ contain three parts: the fluid-fluid interaction $\mathbf{F}_s^{SC}$, the fluid-boundary interaction $\mathbf{F}_s^{fb}$ and the external forces $\mathbf{F}_s^{ext}$, i.e., $\mathbf{F}_s = \mathbf{F}_s^{SC} + \mathbf{F}_s^{fb} + \mathbf{F}_s^{ext}$.

In this thesis, the interaction between components $\mathbf{F}_s^{SC}$ is calculated by the Shan-Chen force (3.70). If we assume that the interaction force is short-ranged, then a suitable expression for the kernel $G_{s\bar{s}}(\mathbf{x}, \overline{\mathbf{x}})$ in the discrete case is given by

$$G(\mathbf{x}, \overline{\mathbf{x}}) = \begin{cases} w_i G_{s\bar{s}}, & \text{for } \overline{\mathbf{x}} = \mathbf{x} + \mathbf{c}_i, \\ 0, & \text{otherwise} \end{cases} \tag{3.82}$$

and (3.70) becomes

$$\mathbf{F}_s^{SC}(\mathbf{x}) = -\rho_s(\mathbf{x}) G_{s\bar{s}} \sum_i w_i \rho_{\bar{s}}(\mathbf{x}+\mathbf{c}_i)\mathbf{c}_i. \tag{3.83}$$

The interaction between fluid and boundary in the Shan-Chen model is given by

$$\mathbf{F}_s^{fb} = -G_{sb}\rho_s(\mathbf{x}, t) \sum_i w_i S(\mathbf{x}+\mathbf{c}_i)\mathbf{c}_i, \tag{3.84}$$

where $S(\mathbf{x})$ is the indicator equal to unity at boundary nodes and vanishing otherwise. The parameters G_{Ab} and G_{Bb} control interactions between fluid components and solid boundary; they are related to contact angles of fluids in the mixture. For a wetting fluid, the interaction should be attractive and therefore $G_{sb} < 0$; and non-wetting fluids should have $G_{sb} > 0$ [55]. In the Boussinesq approximation, the contact angles θ_A and θ_B, measured in the fluids A and B respectively, can be approximated by the following relations [44]

$$\cos\theta_A \simeq \frac{2(G_{Bb} - G_{Ab})}{G_{AB}\mathcal{A}\rho_0}, \quad \cos\theta_B \simeq \frac{2(G_{Ab} - G_{Bb})}{G_{AB}\mathcal{A}\rho_0}. \tag{3.85}$$

For an external force $\mathbf{F}^{ext}$ acting in both components, e.g, gravity, we distribute the force to the components according to their concentration [55]

$$\mathbf{F}_s^{ext} = \frac{\rho_s}{\rho}\mathbf{F}^{ext}, \quad \rho = \sum_s \rho_s. \tag{3.86}$$

The general algorithm for the Shan-Chen multicomponent model is very similar to lattice BGK algorithm described in the previous section for simple fluids. Analogously, at the initial time $t = 0$, we set

$$f_i^s(\mathbf{x}, t) = f_i^{s(eq)}(\rho(\mathbf{x}, t = 0), \mathbf{u}(\mathbf{x}, t = 0)), \tag{3.87}$$

and then:

- Find the fluid densities ρ_s and total velocity $\mathbf{u}$ according to (3.77) and (3.78).
- Calculate the Shan-Chen force for each component $\mathbf{F}_s^{SC}$ according to the formula (3.83). Fluid site interacting with a solid wall is calculated with (3.84). If additional forces act on the fluid, such gravity, sum up all force contributions.
- Compute the equilibrium distribution $f^{s(eq)}$ using (3.80) with a shifted velocity $\mathbf{u}^{(eq)}$ given by
$$\mathbf{u}^{(eq)} = \mathbf{u} + \frac{\tau_s \mathbf{F}_s}{\rho_s} \tag{3.88}$$
where $\mathbf{F}_s$ is the sum of all the forces acting on the component s.
- Collide and stream according to (3.81). The boundary conditions, such bounce-back, are included in the same way as in the case of simple fluids.
- The next time step starts from the calculations of the new equilibrium distributions, and the subsequent evolution of the system is done by repeting the operations of this algorithm until the last time step or convergence has been reached.

Every cycle of the substeps mentioned above corresponds to one time step in the simulations.

3.2.2 Parallel Computing in CUDA

In the lattice Boltzmann method, the collision step occurs locally at each lattice site and the propagation step has only impacts in the closest lattice sites. More specifically, defining $\mathbf{y} = \mathbf{x} + \mathbf{c}_i$ we can rewrite the main evolution equation (3.45) as

$$f_i(\mathbf{y}, t + 1) = f_i(\mathbf{y} - \mathbf{c}_i, 1) - \frac{1}{\tau}(f_i(\mathbf{y} - \mathbf{c}_i, 1) - f_i^{(eq)}(\rho, \mathbf{u})). \tag{3.89}$$

This shows that for each point $\mathbf{y}$ in the discrete grid the algorithm is divided in two steps: i) takes from from the neighboring sites the values of the fields f_i corresponding to populations that are sent to y and then ii) performs the mathematical processing needed to compute the quantities appearing in (3.89). One important aspect is that both steps are completely uncorrelated for different points of the grid, which implies that they can be parallelized according to any convenient schedule if the step i) is performed before step ii) [9].

A second important aspect is the computational domain where the simulation is performed can be partitioned into a sequence of subdomains, where each subdomain is treated by a processor in a CPU. In the LBM algorithm, only the information along the boundary of the subdomain treated by each processor is be transferred to the corresponding neighboring processors. These aspects makes the LBM well suited for computational parallelization, specially on GPUs [78]. A generic pseudocode for the Shan-Chen multicomponent method for CPUs is shown in the Algorithm 1 described below, where the results are plotted for every tPlot time steps, i.e., we plot the numerical solutions when the time parameter is a multiple of the parameter tPlot.

More specifically, GPUs are specialized for compute-intensive and highly parallel computation due to big number of Arithmetic Logic Units (ALU) in comparison to the CPUs. They serves as a coprocessor for CPUs [70], see Fig. 3.2. The ALUs from the NVIDIA GPUs (those are the type of GPUs we use in the simulations of this thesis) are fully programmable using the platform so-called CUDA (Compute Unified Device Architecture), a parallel computing platform which is an extension of C released in 2007 [2]. This platform enable to employ the massive parallel computing capacity of

Figure 3.2: GPU programming interface. Image from [70] by Nvidia Corporation.

Algorithm 1 LBM algorithm–CPU version

-Allocate memory for f_i^s, $f_i^{s(eq)}$, ρ and $\mathbf{u}$;

-Load initial data for ρ_s and $\mathbf{u}$;

-Initialize $f_i^{s(eq)}$ and set $f_i = f_i^{s(eq)}$;

for $(\text{time} = 0; \text{time} <= \text{duration}; \text{time}++)$ **do**

-Perform collision and propagation of f_i^s;

if (tPlot divides time) **then**

-Calculate from the propagation process new values of $\rho_s(\mathbf{x}, t)$, $\mathbf{u}(\mathbf{x}, t)$ and $f_i^{s(eq)}$;

-Print results for $\rho_s(\mathbf{x}, t)$ and $\mathbf{u}(\mathbf{x}, t)$;

end if

end for

-Free memory;

NVIDIA GPUs in order to perform general purpose computation.

The bases for the CUDA programming model is the idea of kernel. The kernel is a function executed in an array of threads in a GPU. A thread on the GPU is a basic abstraction of the data to be processed [70]. In the NVIDIA CUDA architecture, several threads running on multiple processing cores executes the same program on separate data.

Each CUDA function is executed by an array of threads. Each thread had an identification ID that is used to track the memory access. A block is defined as a set of threads running simultaneously and communicating with each other through some shared resources. An scheme of the NVIDIA CUDA thread architecture is shown in Fig. 3.3.

A generic program in CUDA consists in one or more stages executed in a CPU (called *host*) and in the GPU (called *device*). A typical GPU implementation consists in the following main stages [52]:

- Allocate memory in the CPU (*host*) for inputs and outputs and execute the necessary initialization,
- Allocate data on the GPU (*device*) for inputs and outputs,

- Transfer data for *host* to the *device*,
- Execute the kernels and store results in the *device* memory,
- Transfer the processed data for *device* to the *host*,
- Plot results and execute the necessary finalizations.

The parallelization happens in fact when the kernel functions are executed. The specification of the configuration of a kernel function is given by an expression of the form

$$\text{Kernel} <<< n\_\text{threads}, n\_\text{blocks} >>> (\text{inputs}), \tag{3.90}$$

where n_blocks is the number of blocks and $n\_threads$ the number of threads per block. The symbols $<<<$ and $>>>$ are part of the syntax for the kernel functions. The quantity $n\_blocks \times n\_threads$ indicates the number of threads that should be created in the GPUs to execute the respective kernel function. According to [70], the maximum number of threads comported by a block is generally 1024; this value can change depending on the GPU.

In the GPUs we can highlight two types of memories: the *shared memory* and the *global memory*. The information in the *shared memory* is visible to all threads within that block and have the same duration of the block. This type of memory allows for threads to communicate and share data between them. The information in the *global memory* is visible to all threads within the application (also to the host), and has the same duration of the host allocation. The *global memory* is also known to process data more slowly than the *shared memory* [52]. For some other types of memory residing in GPUs, see [70].

A generic pseudocode for the Shan-Chen multicomponent method is shown in the Algorithm 2 below, where the results are plot for every tPlot time steps. All steps are synchronized by the use of the function *cudaDeviceSynchronize* after each kernel launch (some other ways to synchronize threads are available, see [52]). Each point of the grid is processed by several computational steps in the loops over time, for each loop we keep two copies of the grid, with each step reading the data from one copy and writing the results to the other [9].

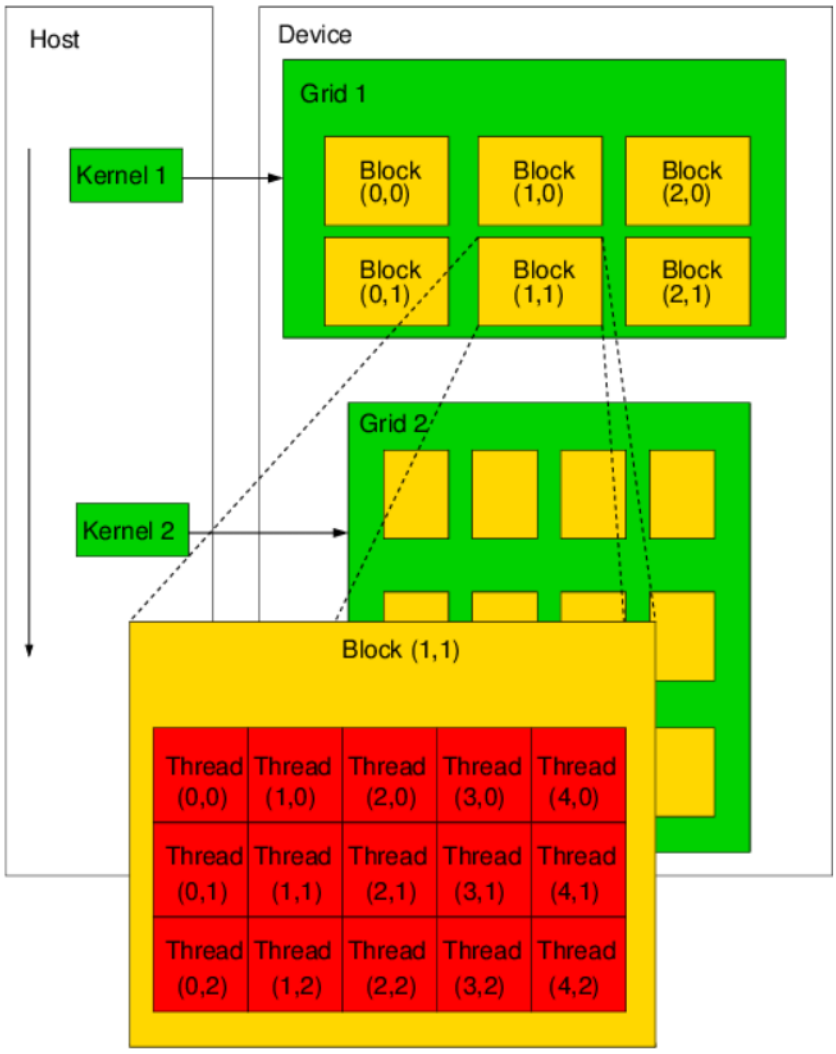

Figure 3.3: A schematic example of a GPU programming interface. The same function defined by the kernel is executed in all threads of the GPU. Image from [41].

The function Kernel 1 in the Algorithm 2 for GPUs executes essentially the algorithm described in the Algorithm 1 for CPUs, with the exception that the propagation of the distributions f_i^s between blocks is executed by another kernel function, which we call Kernel 2. Depending on the complexity of the LBM code, in terms of complex computational domains and memory usage, more elaborate kernels are used. For more details, see [9, 11].

Algorithm 2 GPU version/Shan-Chen multicomponent method

Main program in CPU

-Alocate global memory on device;

-Upload initial data for ρ_s, $\mathbf{u}$, $f_i^{s(eq)}$, f_i^s and $\mathbf{F}_s^{(SC)}$ on device;

for $(\text{time} = 0; \text{time} <= \text{duration}; \text{time}++)$ **do**

-Execute Kernel $1<<<n\_\text{threads}, n\_\text{blocks}>>>(\rho_s, \mathbf{u}, f_i^{s(eq)}, f_i^s, \mathbf{F}_s^{(SC)})$;

-cudaDeviceSynchronize();

if (tPlot divides time) **then**

-Download updated data ($\rho_s(\mathbf{x}, t)$, $\mathbf{u}(\mathbf{x}, t)$,...) from global memory on device;

-Print results;

end if

-Execute Kernel $2<<<n\_\text{threads}, n\_\text{blocks}>>>(f_i^s)$;

-cudaDeviceSynchronize();

end for

-Free global memory on device;

Algorithm 3 Kernel 1

-Load f_i^s from global memory on device;

-Alocate shared memory for f_i^s;

-Calculate $\mathbf{u}$, ρ_s and $f_i^{s(eq)}$;

-Apply the collision process on f_i^s;

-Stream f_i^s inside the shared memory of the same block;

-Propagates f_i^s in global memory;

-Some distributions f_i^s are propagated within global memory bewteen thread block using the Kernel 2 function;

3.3 Continuum limit equations and the Boussinesq system

The traditional Navier-Stokes and Cahn-Hilliard equations (CHNS system) can be approximately recovered from the Shan-Chen LBM algorithm if the total density $\rho = \rho_A + \rho_A$ of the fluid mixture is almost constant [63, 5], which is the case for mixtures with similar densities. The order parameter $\phi = \rho_A - \rho_B$ and velocity field $\mathbf{u}$ satisfies, in the incompressible limit $|\mathbf{u}| \ll c/\sqrt{3}$, the following CHNS system:

$$\begin{aligned}
\nabla \cdot \mathbf{u} &= 0, && (3.91)\\
\frac{\partial \phi}{\partial t} + \nabla \cdot (\phi \mathbf{u}) &= \nabla \cdot [M \nabla \mu] && (3.92)\\
\rho \left(\frac{\partial \mathbf{u}}{\partial t} + (\mathbf{u} \cdot \nabla)\mathbf{u} \right) &= -\nabla \cdot \mathbf{P}^{TOT} + \nabla \cdot \left[\rho \nu (\nabla \mathbf{u} + \nabla^T \mathbf{u}) \right] + \mathbf{F}, && (3.93)\\
M &= \frac{\rho^2 - \phi^2}{\rho} (\tau - 0.5), && (3.94)\\
\mu &= \frac{c_s^2}{2} \ln \left(\frac{\rho + \phi}{\rho - \phi} \right) - \frac{c_s^2 \tau G_{AB}}{2(\tau - 0.5)} \phi - \frac{c_s^4 \tau G_{AB}}{4(\tau - 0.5)} \Delta \phi, && (3.95)\\
& && (3.96)
\end{aligned}$$

where M is the mobility, μ is the chemical potential, $\mathbf{F} = \mathbf{F}_A + \mathbf{F}_B$ is the total force acting on the system and $\mathbf{P}^{(TOT)}$ is the *momentum-flux tensor*, which can be decomposed as the sum of a kinetic component $\mathbf{P}^{kin}$ plus an interaction term $\mathbf{P}^{int}$, i.e.,

$$\mathbf{P}^{(TOT)} = \mathbf{P}^{kin} + \mathbf{P}^{int}, \tag{3.97}$$

where

$$\mathbf{P}^{kin} = \sum_{is} f_{is} \mathbf{c}_i \otimes \mathbf{c}_i, \tag{3.98}$$

and $\mathbf{P}^{int}$ is defined by the condition

$$\nabla \cdot \mathbf{P}^{int} = -\sum_{s} \mathbf{F}_s^{SC}. \tag{3.99}$$

When the distribution functions f_i^A, f_i^B are close to the local equilibrium, the kinetic part of the pressure tensor takes the form [80]

$$\mathbf{P}^{kin} = c_s^2 \rho \mathbf{I} + \mathbf{K}^{(\tau)}, \tag{3.100}$$

where

$$\mathbf{K}^{(\tau)} = c_s^4 \frac{\rho_A \rho_B}{\rho} \left(\tau - \frac{1}{2}\right)^2 \left(\frac{\nabla \rho_A}{\rho_A} - \frac{\nabla \rho_B}{\rho_B}\right) \otimes \left(\frac{\nabla \rho_A}{\rho_A} - \frac{\nabla \rho_B}{\rho_B}\right). \tag{3.101}$$

This extra spurious τ-dependent contribution $\mathbf{K}^{(\tau)}$ is small for τ close to $1/2$ and for small variations of the total densities of the system. The study of the influence of such spurious contributions in the context of the Rayleigh-Taylor systems is given in Chapter 5.

An explicit form for the interaction a pressure tensor $\mathbf{P}^{int}$ verifying (3.99) can be constructed interactively, by guessing an initial form and applying the gradient operator to it, identifying the extraneous terms that do not satisfy (3.99), and modifying the $\mathbf{P}^{int}$ guess by inspection of the extra terms. For the sake of clarity, let us expand each density $\rho_s(\mathbf{x} + \mathbf{c}_i)$ about $\mathbf{x}$

$$\rho_s(\mathbf{x}+\mathbf{c}_i) = \rho_s(\mathbf{x},t) + c_i^a \partial_a \rho_s(\mathbf{x},t) + \frac{1}{2} c_i^a c_i^b \partial_a \partial_b \rho_s(\mathbf{x},t) + \frac{1}{6} c_i^a c_i^b c_i^c \partial_a \partial_b \partial_c \rho_s(\mathbf{x},t) + \cdots \tag{3.102}$$

Substituting the expansions into the Shan-Chen force (3.83) for each component, we have:

$$\begin{aligned}
\mathbf{F}_A^{SC}(\mathbf{x},t) &= -G_{AB}\rho_A(\mathbf{x},t) \sum_i w_i \mathbf{c}_i \left(\rho_B(\mathbf{x},t) + c_i^a \partial_a \rho_A(\mathbf{x},t) + \right. \\
&+ \left. \frac{1}{2} c_i^a c_i^b \partial_a \partial_b \rho_B(\mathbf{x},t) + \cdots\right), \\
\mathbf{F}_A^{SC}(\mathbf{x},t) &= -G_{BA}\rho_B(\mathbf{x},t) \sum_i w_i \mathbf{c}_i \left(\rho_A(\mathbf{x},t) + c_i^a \partial_a \rho_A(\mathbf{x},t) + \right. \\
&+ \left. \frac{1}{2} c_i^a c_i^b \partial_a \partial_b \rho_A(\mathbf{x},t) + \cdots\right),
\end{aligned}$$

Due to the symmetry of the velocity sets, the terms $\sum_i w_i \mathbf{c}_i$ and $\sum_i w_i \mathbf{c}_i c_i^a c_i^b$ vanishes [55]. Including expansion terms from (3.102) up to third order, the continuum form of the total Shan-Chen force $\mathbf{F}^{SC} = \mathbf{F}_A^{SC} + \mathbf{F}_B^{SC}$ is given by

$$\mathbf{F}^{SC}(\mathbf{x},t) = -c_s^2 G_{AB} \nabla(\rho_A \rho_B) - \frac{c_s^4 G_{AB}}{2} \rho_A(x,t) \nabla \Delta \rho_B(x,t) - \frac{c_s^4 G_{AB}}{2} \rho_B(x,t) \nabla \Delta \rho_A(x,t). \tag{3.103}$$

It is possible to verify by inspection that a continuum form of the interaction pressure tensor $\mathbf{P}^{int}$ satisfying (3.99) is given by

$$\mathbf{P}^{int} = c_s^2 G_{AB} \rho_A \rho_B + c_s^4 \frac{G_{AB}}{2} \left[\rho_A \Delta \rho_B + \rho_B \Delta \rho_A - (\nabla \rho_A \cdot \nabla \rho_B)\right] - c_s^4 G_{AB} \nabla \rho_A \otimes \nabla \rho_B. \tag{3.104}$$

A similar procedure without using the assumption of the continuum limit [79] leads to the following expression

$$P_{ab}^{int}(\mathbf{x}) = \frac{G_{AB}}{2}\rho_A(\mathbf{x})\sum_i w_i\rho_B(\mathbf{x}+\mathbf{c}_i)c_i^a c_i^b + \frac{G_{AB}}{2}\rho_B(\mathbf{x})\sum_i w_i\rho_A(\mathbf{x}+\mathbf{c}_i)c_i^a c_i^b. \quad (3.105)$$

If we neglect the gradients of the total density ρ in $\mathbf{P}^{int}$ and the contribution of $\mathbf{K}^{(\tau)}$ in $\mathbf{P}^{kin}$, we have

$$\mathbf{P}^{(TOT)} = c_s^2\left[\rho + \frac{G_{AB}}{4}(\rho^2-\phi^2) - c_s^2\frac{G_{AB}}{4}\phi\Delta\phi - c_s^2\frac{G_{AB}}{8}|\nabla\phi^2|\right]\mathbf{I} + c_s^4\frac{G_{AB}}{4}\nabla\phi\otimes\nabla\phi. \quad (3.106)$$

This is the classical form the stress tensor with Korteweg stresses characteristic of diffuse interface methods [3]. We give a short description of general diffuse interface formulations for multicomponent flows in Appendix A.

The total stress tensor (3.106) can also be split into two parts

$$\mathbf{P}^{(TOT)} = p_b\mathbf{I} + \mathbf{P}^K, \quad (3.107)$$

where p_b denotes the pressure in the bulk regions, which leads to the following equation of state

$$p_b = c_s^2\rho + \frac{G_{AB}c_s^2}{4}(\rho^2-\phi^2). \quad (3.108)$$

In Chapter 3 we use the relation (3.108) to obtain parameters like the surface tension using the Laplace-Young test [55]. The effects of the interfaces are taken into account by the contribution

$$\mathbf{P}^k = \left[-c_s^4\frac{G_{AB}}{4}\phi\Delta\phi - c_s^4\frac{G_{AB}}{8}|\nabla\phi^2|\right]\mathbf{I} + c_s^4\frac{G_{AB}}{4}\nabla\phi\otimes\nabla\phi \quad (3.109)$$

corresponding to the Korteweg stress tensor [57, 100, 3]. This tensor is responsible for the effects of surface tension in mixtures of immiscible fluids. A more detailed analysis of such effects is described in Chapter 5.

If we considering a system with external forces in each component given by

$$\mathbf{F}_A^{ext} = -\rho_A\,\tilde{g}\mathbf{e}_y, \quad \mathbf{F}_B^{ext} = \rho_B\tilde{g}\,\mathbf{e}_y, \quad (3.110)$$

where $\tilde{g}$ is the buoyancy intensity, we obtain from (3.94) the following momentum equation

$$\rho\left(\frac{\partial\mathbf{u}}{\partial t} + (\mathbf{u}\cdot\nabla)\mathbf{u}\right) = -\nabla\cdot\mathbf{P}^{(TOT)} + \nabla\cdot\left[\rho\nu(\nabla\mathbf{u}+\nabla\mathbf{u}^T)\right] - \phi\tilde{g}\mathbf{e}_y. \quad (3.111)$$

which corresponds to the diffuse interface formulation [3] of the Boussinesq approximation (2.2), (2.5) and (2.6) introduced in the Chapter 2. This approximation holds for the equations of the Rayleigh-Taylor systems at scales much larger than the width of the diffuse interface.

3.3.1 Diffusion equation for the order parameter for miscible mixtures

In this subsection, we clarify the connection between the Cahn-Hilliard equation (3.92), obtained by the SC multicomponent method, and the advection–diffusion equation (2.37) for the order parameter for miscible mixtures of incompressible fluids with close densities.

Assuming small variations of the total density, the classical diffusion equation for the order parameter for miscible mixtures case can be recovered through the Chan-Hilliard (3.92). In this context, the order parameter in the bulk region is almost constant and in the region where the components interact the typical value of this parameter is small in comparison with the value of the total density, $\phi \ll \rho$, leading to the approximation

$$M(\rho, \phi, \tau) \simeq M(\rho, \tau) = \rho\,(\tau - 0.5)\,. \tag{3.112}$$

This yields to the generalized advection–diffusion equation for the order parameter:

$$\frac{\partial \phi}{\partial t} + \nabla \cdot (\phi \mathbf{u}) = M \Delta \mu. \tag{3.113}$$

For miscible mixtures we neglect order parameter derivatives of order $O(\partial^4)$ [55], which implies that we can neglect influence of the Laplacian term in the chemical potential inside the CH equation. Therefore

$$\frac{\partial \phi}{\partial t} + \nabla \cdot (\phi \mathbf{u}) = M(\rho, \tau) \Delta \left(\frac{c_s^2}{2} \ln \left(\frac{\rho + \phi}{\rho - \phi} \right) - \frac{c_s^2 \tau G_{AB}}{2(\tau - 0.5)} \phi \right). \tag{3.114}$$

Also, considering $\phi \ll \rho$, we expand the logarithm and we keep only the first order terms. We also neglect the constants because the CH equations only accounts for the first variations of the chemical potential. The result is the following

$$\frac{\partial \phi}{\partial t} + \nabla \cdot (\phi \mathbf{u}) = \left[M(\rho, \tau) \left(\frac{c_s^2}{\rho} - \frac{c_s^2 \tau G_{AB}}{2(\tau - 0.5)} \right) \right] \Delta \phi. \tag{3.115}$$

Next, define the approximate diffusion coefficient as

$$D_{AB} = M(\rho,\tau)\left(\frac{c_s^2}{\rho} - \frac{c_s^2\tau G_{AB}}{2(\tau-0.5)}\right) = c_s^2\left[(\tau-0.5) - \frac{\rho\tau G_{AB}}{2}\right], \tag{3.116}$$

and finally

$$\frac{\partial\phi}{\partial t} + \nabla\cdot(\phi\mathbf{u}) = D_{AB}\Delta\phi. \tag{3.117}$$

This is the advection-diffusion equation for the order parameter in the Shan-Chen method multicomponent method. It describes the order parameter evolution for the miscible Rayleigh-Taylor system presented in Chapter 2.

3.4 Free-energy procedure and the mechanism of the process of the separation of the components

In the systems formed by the equations (3.91), (3.92) and (3.111) the difference between miscible and immiscible flows is essentially determined by the values of the interaction parameter G_{AB}. In this section, we give more details of the role of the mechanisms of the separation of the components in the Shan-Chen model. These mechanisms are completely analogous to the phenomenon of the spinodal decomposition in classical thermodynamic theories based on the Ginsburg-Landau free energy functional [58, 45, 32].

The mechanism fixing the bulk densities in the phase separation process in the Shan-Chen method is naturally associated with free energy functional in the continuum limit (where all discrete lattice effects disappear) when $\tau \gg 1/2$. Consider the following free-energy density of the form

$$\begin{aligned} F(\rho,\phi) &= c_s^2\left(\frac{\rho+\phi}{2}\right)\log\left(\frac{\rho+\phi}{2}\right) + c_s^2\left(\frac{\rho-\phi}{2}\right)\log\left(\frac{\rho-\phi}{2}\right) \\ &+ \frac{c_s^2 G_{AB}}{4}\left(\rho^2-\phi^2\right) + c_s^4\frac{G_{AB}}{8}|\nabla\phi|^2. \end{aligned} \tag{3.118}$$

This equation consists in two ideal free-energy densities plus an interaction term, and is based on the form of the Ginzburg-Landau free energy for incompressible binary mistures [32]. The bulk contribution is given by the so-called bulk potential

$$V(\rho,\phi) = c_s^2\left(\frac{\rho+\phi}{2}\right)\log\left(\frac{\rho+\phi}{2}\right) + c_s^2\left(\frac{\rho-\phi}{2}\right)\log\left(\frac{\rho-\phi}{2}\right) + \frac{c_s^2 G_{AB}}{4}\left(\rho^2-\phi^2\right), \tag{3.119}$$

which correctly reproduces the bulk contribution of the stress tensor (3.108) by using the following generalized Legendre's transformation

$$P_b(\rho,\phi) = \rho\frac{\partial V(\rho,\phi)}{\partial \rho} + \phi\frac{\partial V(\rho,\phi)}{\partial \phi} - V(\rho,\phi) = c_s^2\rho + \frac{c_s^2 G_{AB}}{4}\left(\rho^2 - \phi^2\right). \tag{3.120}$$

We next introduce the mass conserving free energy density

$$L^{\lambda_1,\lambda_2} = L - \lambda_1\phi - \lambda_2\rho, \tag{3.121}$$

where λ_1 and λ_2 are Lagrange multipliers introduced to ensure the global conservation of ϕ and ρ. This leads to the Euler-Langrage equations

$$\frac{\delta L^{\lambda_1,\lambda_2}}{\delta\phi} = \frac{\partial L^{\lambda_1,\lambda_2}}{\partial\phi} - \nabla\cdot\left[\frac{\partial L^{\lambda_1,\lambda_2}}{\partial(\nabla\phi)}\right] = 0, \tag{3.122}$$

$$\frac{\delta L^{\lambda_1,\lambda_2}}{\delta\rho} = \frac{\partial L^{\lambda_1,\lambda_2}}{\partial\rho} - \nabla\cdot\left[\frac{\partial L^{\lambda_1,\lambda_2}}{\partial(\nabla\rho)}\right] = 0, \tag{3.123}$$

resulting in

$$\lambda_1 = \frac{\partial V(\phi,\rho)}{\partial\phi} - \frac{c_s^4 G_{AB}}{8}\Delta\phi, \quad \lambda_2 = \frac{\partial V(\phi,\rho)}{\partial\rho}. \tag{3.124}$$

The free-energy density (3.118) is invariant with respect to translations of the spatial coordinates, which implies in a correspondent conservation law for the system according to Noether's theorem [3], i.e., $\nabla\cdot\mathbf{C} = 0$, where $\mathbf{C}$ is second-order tensor given by

$$\mathbf{C} = -L^{\lambda_1,\lambda_2} + \nabla\phi\otimes\frac{\partial L^{\lambda_1,\lambda_2}}{\partial(\nabla\phi)}. \tag{3.125}$$

Using the solutions for the Lagrange multipliers, we obtain

$$\mathbf{C} = \left[p_b - \frac{c_s^2 G_{AB}}{4}\phi\Delta\phi - \frac{c_s^2 G_{AB}}{8}|\nabla\phi|^2\right]\mathbf{I} + \frac{c_s^4 G_{AB}}{4}\nabla\phi\otimes\nabla\phi, \tag{3.126}$$

which corresponds to the total pressure tensor (3.106).

The free-energy formulation also permits to rewrite the chemical potential in the order parameter equation (3.92) in terms of the

$$\mu = \frac{\delta F}{\delta\phi} = \frac{c_s^2}{2}\log\left(\frac{\rho+\phi}{\rho-\phi}\right) - \frac{G_{AB}}{2}c_s^2\phi - \frac{c_s^4 G_{AB}}{4}\Delta\phi. \tag{3.127}$$

Note that in the formula (3.92), we have some spurious influence of the parameter τ, indicating the appearance of lattice discreetness effects, it shows that an exact matching between momentum and order parameter equations starting from the continuum

free-energy formulation (3.118) is not direct and more elaborated arguments are necessary [5]. Nevertheless, is possible to fix the bulk densities introducing the following τ-dependent functional

$$F^{(\tau)}(\rho,\phi) = c_s^2\left(\frac{\rho+\phi}{2}\right)\log\left(\frac{\rho+\phi}{2}\right) + c_s^2\left(\frac{\rho-\phi}{2}\right)\log\left(\frac{\rho-\phi}{2}\right) \quad (3.128)$$

$$+ \frac{c_s^2 G_{AB}^{(\tau)}}{4}\left(\rho^2-\phi^2\right) + c_s^4\frac{G_{AB}^{(\tau)}}{8}|\nabla\phi|^2. \quad (3.129)$$

where $G_{AB}^{(\tau)} = \left(\frac{\tau}{\tau-1/2}\right)G_{AB}$ is the effective interaction parameter. Note that in the limit $\tau \gg 1/2$, with constant viscosity, we have $G_{AB}^{(\tau)} \to G_{AB}$, reproducing the continuum value (3.118). This τ dependence also has an influence in the values of the bulk densities, which are determined by the bulk potential

$$V^{(\tau)}(\rho,\phi) = c_s^2\left(\frac{\rho+\phi}{2}\right)\log\left(\frac{\rho+\phi}{2}\right) + c_s^2\left(\frac{\rho-\phi}{2}\right)\log\left(\frac{\rho-\phi}{2}\right) + \frac{c_s^2 G_{AB}^{(\tau)}}{4}\left(\rho^2-\phi^2\right). \quad (3.130)$$

In Fig. 3.4, we show that a suitable choice of $G_{AB}^{(\tau)}$ produces a double well structure, meaning that there are two possible bulk solutions, i.e., these are two bulk phases that coexist in equilibrium characterizing an immiscible mixture. Once we know the total density ρ and the interaction parameter $G_{AB}^{(\tau)}$, we can determine the minima for $V(\phi,\rho)$ and predict the bulk equilibrium values of the order parameter.

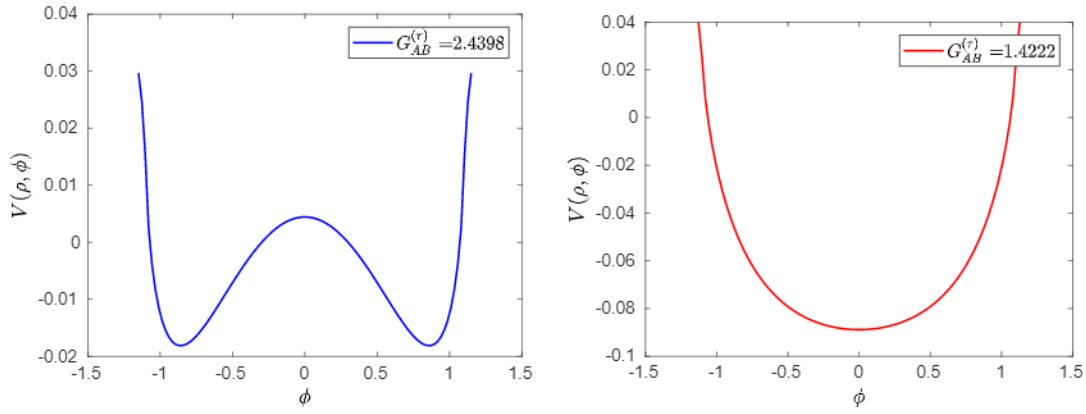

(a) (b)

Figure 3.4: Free energy density $V^{(\tau)}$ as a function of the variable ϕ for a fixed $\rho = 1.1$ as a function of the order parameter ϕ for a two-phase (a) and a single phase (b) mixture. We consider different interaction strengths parameters $G_{AB}^{(\tau)}$. It is possible to see that increasing the values of G_{AB} we obtain the spinodal decomposition characteristic of the immiscible mixtures.

3.5 Immiscible and miscible Rayleigh-Taylor systems

Using the Shan-Chen multicomponent method we simulate the immiscible and miscible Rayleigh-Taylor systems described in Chapter 2. The results are shown in the Figures 3.5 and 3.6 for the immiscible and miscible cases, respectively. In this subsection, we describe the details of these simulations.

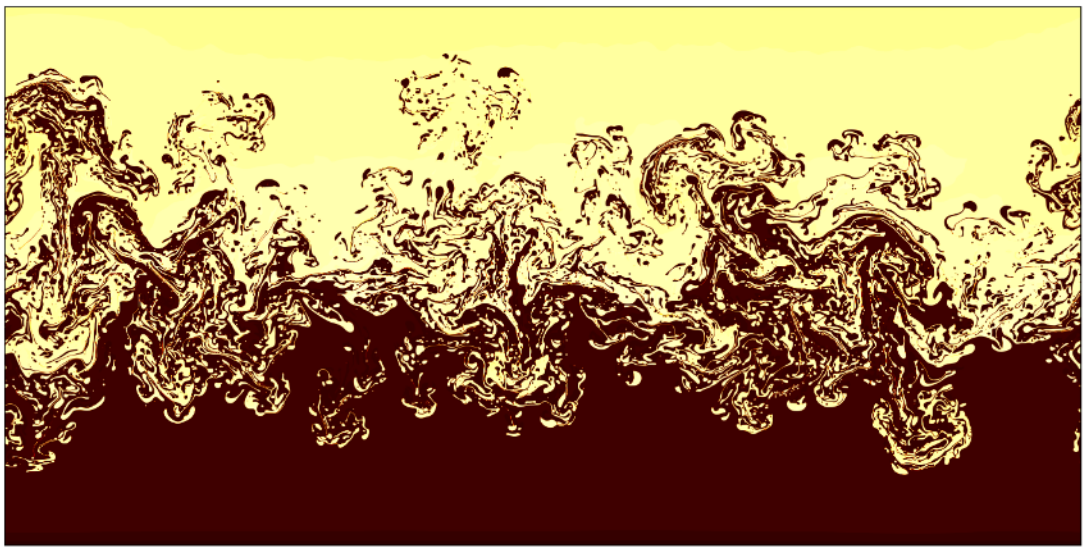

Figure 3.5: Immiscible Rayleigh-Taylor turbulence for the time $t = 83.000$ corresponding to the fully developed turbulent phase showed in Figure 1.3 from Chapter 2.

We choose $\Delta x = \Delta t = 1$ (considered as lattice units) in the rectangular domain of horizontal size $L_x = 10^4$ and vertical size $L_y = L_x/2$. Periodic boundary conditions are assumed in the horizontal direction with the rigid bottom and top boundaries. The no-slip condition, $u = 0$, is assumed at a rigid boundary. This condition is the simplest choice for the boundaries, which is also convenient from a numerical point of view. We stop our simulations before the mixing layer reaches the boundaries. The bounce-back relation [63] is used for the distribution function $f_i^s(\mathbf{x}, t)$ at the solid boundaries for modeling the no-slip condition.

The relaxation time $\tau = 0.53$ is chosen for both components, providing the kinetic viscosity $\nu = c_s^2(\tau - 1/2) = 0.01$. The value of τ was set as low as possible to provide the high Reynolds numbers needed to obtain the turbulent regime in RT systems. For

$\tau < 0.53$, the simulations become unstable.

We consider pure densities of both fluid components equal 1.10 and the gravity parameter $\tilde{g} = 9 \cdot 10^{-6}$. Since changes of the total density due to pressure variations and mixing are small, we approximate $\rho(\mathbf{x}, t) \approx \rho_0$ by a constant. In this case, the Boussinesq buoyancy force (2.6) agrees with our choice of the external force (3.110) for normalized values of the order parameter.

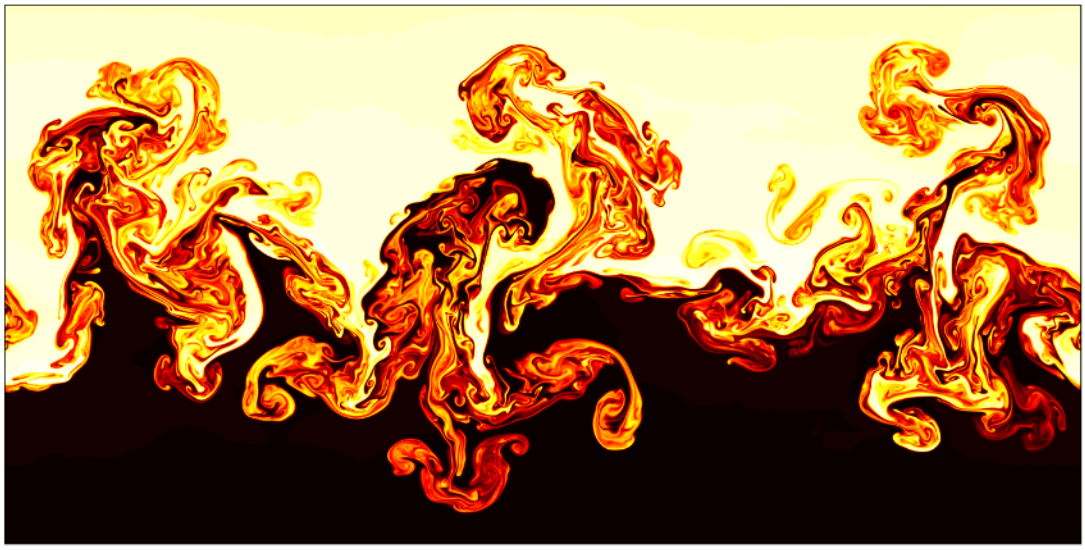

Figure 3.6: Miscible Rayleigh-Taylor turbulence for the time $t = 83.000$ corresponding to the fully developed turbulent phase showed in Figure 1.2 from Chapter 2.

The coupling constant G_{AB} has a critical value with the immiscible fluid for stronger couplings and miscible fluid for weaker couplings. For our immiscible and miscible models we select $G_{AB} = 0.1381$ and $G_{AB} = 0.0805$, respectively. In the interactions with the boundaries we use neutral wetting, i.e., $G_{Ab} = G_{Bb} = 0$, to minimize the influence of the boundaries.

In the immiscible model, two components are separated by a diffuse interface having a width of approximately $l_{int} \sim 3$ grid nodes [55]. This model approximates the Boussinesq system formed by (2.2) and (2.5) considered at scales much larger than l_{int} with the surface tension $\gamma = 0.0059$ obtained from pressure measurements for large bubbles. Similarly, one recovers the miscible Boussinesq system (2.38), (2.39) and (2.37) in the continuous limit for small gradients of the order parameter. The diffusion coefficient can be estimated roughly using (3.116) as $D_{AB} \simeq 0.002$ [5]. Though the

diffusion coefficient is a function of order parameter for a more accurate description, such dependence is not important for our study based on the phenomenological theory of turbulence.

We initialize the flow by using an equilibrium immiscible configuration and adding a small random (white-noise) deformation to the interface with an amplitude of 4 grid points. In this equilibrium configuration, the first phase consists primarily of component A with about 9% of component B, and vise versa for the second component.

The simulations are implemented on GPUs of the model NVIDIA Tesla V100 PCIe 32 GB with $n\_threads = 256$ and $n\_blocks = 1,9531 \cdot 10^5$ as input parameters for the main kernel functions. This choice of parameters verifies

$$\text{n\_threads} \times \text{n\_blocks} = L_x \times L_y. \tag{3.131}$$

The use of $n\_threads = 256$ provides an optimized performance for our applications in the mentioned GPUs. The simulations are performed in the cluster of computers Tsunami5 located at IMPA. In this cluster, processors of the model Intel Xeon Platinum 8160 (33M Cache, 2.10 GHz) are used.

For the statistics used in this thesis we collect ensambles with at least 10 simulations. Each simulation takes approximatelly 10 hours to perform 90.000 time steps on GPUs.

One of the main advantages of the method described is to provide access to hydrodynamic scales at an affordable computational cost, which is way beyond the capabilities of some other traditional methods to treat the same range of scales, like Molecular Dynamics or Monte Carlo simulations, for example [55, 89, 5]. The computational configuration described for the Rayleigh-Taylor in this thesis can be associated with different physical configurations. For a physical system with a given surface tension γ_{phys} and viscosity ν_{phys}, we can consider the following relations [55]

$$\gamma_{phys} \approx \gamma_{LB} \frac{k_B T}{(\Delta \overline{x})^2}, \qquad \nu_{phys} \approx \nu_{LB} \frac{(\Delta \overline{x})^2}{\Delta \overline{t}}, \tag{3.132}$$

where the subscript LB denotes the value in lattice Boltzmann units, k_B is the Boltzmann constant, T is the temperatures in Kelvin and $\Delta \overline{x}$ and $\Delta \overline{t}$ are the spatial and time step sizes in the physical domain in meters. For the parameters used for the simulations showed in Fig. 3.5, it is possible to obtain surface tensions characteristic of microemusions and viscosities with values close to the water viscosity. [5].

We the next chapters, we performed a number of numerical tests justifying the validity of the the lattice Boltzmann model to simulate the Rayleigh-Taylor instability. In particular, we showed that the numerical dispersion relations are in agreement with theoretical predictions showed in Chapter 2. Also, we verified that non-isotropic contributions to the stress tensor, caused by variations of order parameter, are small in the miscible case. In the immiscible flow, these contributions grow in time following the increase of the interface, but remain small compared to buoyancy and viscous contributions. Also, the numerical anisotropy of the Shan-Chen force generates spurious currents within thin diffuse interfaces, which do not affect most of our measurements, but may interfere in the results for enstrophy, as discussed at the end of Chapter 4.

Chapter 4

Numerical tests of the Shan-Chen multicomponent model

In this chapter, we show a series of basic experiments to test the validity and to check the limitations of the Shan-Chen multicomponent method discussed in the Chapter 3. In the first part, we analyze how to calculate the surface tension coefficient using the Shan-Chen multicomponent model. This coefficient is calculated using the so-called Laplace-Young test. The value obtained is also compared with an alternative method based on an analysis of the stress balance in a planar interface separating two immiscible fluids. Thereafter, we investigate the dispersion relation (2.36) analyzing the growth rate of single modes in lattice-Boltzmann simulations of the Rayleigh-Taylor instability. In the final part, we discuss some limitations of the Shan-Chen method associated to the appearance of the so-called spurious currents. For this purpose, we study the statistics of the velocity and vorticity fields of droplets in regions far and close to the interfaces. A similar analyses is also employed for the statistics of the vorticity fields in the late stages of the immiscible and miscible Rayleigh-Taylor turbulence.

4.1 The Laplace-Young test and the surface tension coefficient

The Laplace-Young test is a numerical experiment that consists of a way to calculate the surface tension between two fluids using the Laplace-Young equation for

bubbles in two dimensions given by

$$\Delta p_b = p_b^{inside} - p_b^{outside} = \frac{\gamma}{R}. \tag{4.1}$$

In this experiment, we simulate a liquid droplet of one component (component A) inside of the other component (component B), and from the plot of the difference of pressure Δp_b versus the inverse of the radius $1/R$ of the droplets, we obtain (analysing the inclination of the lines) the surface tension γ. The value of $p_b^{outside}$ is calculated by (3.120) outside the droplet far from the interface, and p_b^{inside} is calculated same way inside the droplet.

In Fig. 4.1, we show the Laplace-Young experiment for droplets simulations in grid 64x64. The values of p_b^{inside} and $p_b^{outside}$ are calculated according to the formula

$$p_b = c_s^2(\rho_A + \rho_B) + c_s^2 G_{AB}\rho_A\rho_B. \tag{4.2}$$

described in Chapter 3. Both components are initialized with the same densities $\rho_A = \rho_B = 1.10$. The radii of the droplets are collected after some time in the simulation necessary to reduce transient effects, which are detected by the analysis of the magnitude of the velocity fields. These effects are the result of the lattice Boltzmann initialization process due to the fact that sometimes the initial configuration is not the system's equilibrium solution. The blue line in Fig. 4.1 represents the Laplace-Young experiment for $G_{AB} = 0.1381$ and $\tau = 0.53$; and the red curve corresponds to $G_{AB} = 1.2200$ and $\tau = 1.00$. The parameters correspond to the same value of the effective interaction parameter

$$G_{AB}^{(\tau)} = \frac{\tau}{(\tau - 0.5)} G_{AB} = \frac{1.0}{(1.0 - 0.5)} 1.22 = \frac{0.53}{(0.53 - 0.5)} 0.1381 = 2.44. \tag{4.3}$$

This value of $G_{AB}^{(\tau)}$ corresponds to the spinodal decomposition shown in Fig. 3.4(a).

Alternatively, we compute the surface tension through the mismatch between the normal and transversal components of the pressure tensor P_{TOT}, integrated across a planar interface [55] in its normal direction as

$$\gamma = \int_{-\infty}^{\infty} (P_n^{TOT} - P_t^{TOT}) dn. \tag{4.4}$$

To be more precise, let us consider a planar interface located at $y = 0$ in a rectangular domain with periodic boundary conditions in the horizontal direction and vertical rigid

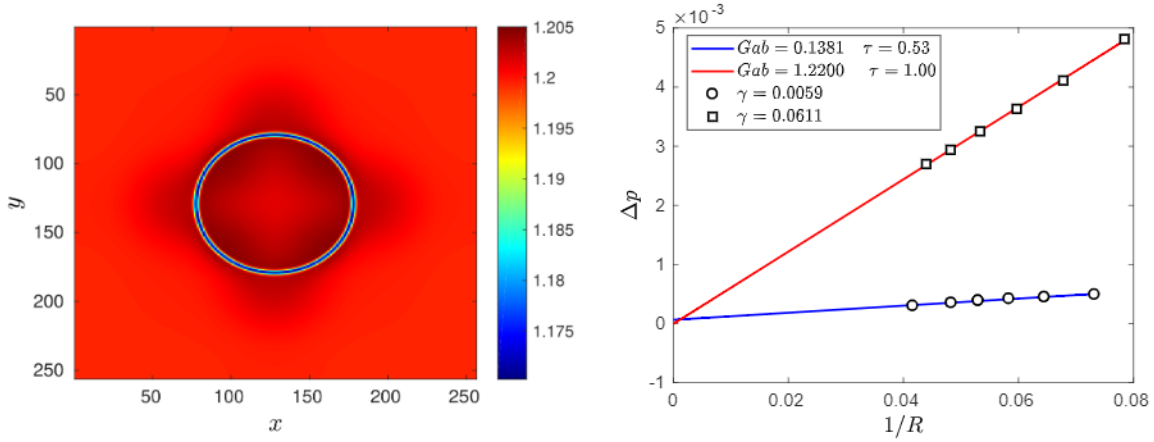

(a) (b)

Figure 4.1: (a) Total density field $\rho = \rho_A + \rho_B$ in a droplet with radius R=51.2 (b) Results of the Young-Laplace test for droplet of the fluid A in the fluid B for two different interaction parameters in a system with size 64x64. We can see that the pressure difference Δp_b across the droplet interface is proportional to the droplet's curvature radius $1/R$. The pressure difference and surface tension are shown in lattice units.

wall in the vertical direction. The walls must be located far from the interface to not generate any influence in the stress balance at the interface. Also, we consider no external forces acting on the system. In this case we consider y the parameter for the direction $P_n^{TOT} = P_{yy}^{TOT}$ and $P_t^{TOT} = P_{xx}^{TOT}$, where

$$P_{yy}^{TOT} = c_s^2 \left[\rho + \frac{G_{AB}}{4}(\rho^2 - \phi^2) - c_s^2 \frac{G_{AB}}{4}\phi\Delta\phi - c_s^2 \frac{G_{AB}}{8}|\nabla\phi^2| \right] \mathbf{I} \tag{4.5}$$

$$+ \; c_s^4 \frac{G_{AB}}{4} \left(\frac{\partial \phi}{\partial y} \right)^2, \tag{4.6}$$

$$P_{xx}^{TOT} = c_s^2 \left[\rho + \frac{G_{AB}}{4}(\rho^2 - \phi^2) - c_s^2 \frac{G_{AB}}{4}\phi\Delta\phi - c_s^2 \frac{G_{AB}}{8}|\nabla\phi^2| \right] \mathbf{I}. \tag{4.7}$$

This leads to the following surface tension coefficient

$$\gamma = \frac{c_s^4 G_{AB}}{4} \int_{-\infty}^{\infty} \left(\frac{\partial \phi}{\partial y} \right)^2 dy. \tag{4.8}$$

To prevent possible lattice discreetness effects [5], we add the contribution of the $\mathbf{K}^{(\tau)}$ in (4.8)

$$\gamma = \frac{c_s^4 G_{AB}}{4} \int_{-\infty}^{\infty} \left(\frac{\partial \phi}{\partial y} \right)^2 dy + \int_{-\infty}^{\infty} K_{yy}^{(\tau)} dy. \tag{4.9}$$

The formula (4.9) gives the value $\gamma = 0.0585$ for $G_{AB} = 1.2200$ and $\tau = 1.22$; and $\gamma = 0.0053$ for $G_{AB} = 0.1381$ and $\tau = 0.53$. We can see a good agreement with the values obtained by the Laplace-Young test in Fig. 4.1.

4.2 Linear stabiility analysis of the Rayleigh-Taylor instability

An important verification for parameters and accuracy for the lattice Boltzmann method consists in the verification of the dispersion relation for the Rayleigh-Taylor instability (2.36).

Consider the initial configuration for the immiscible RT instability presented in Chapter 2. The Boussinesq approximation is equivalent to the symmetric system shown in Fig. 4.2. In this system, both components have same density $\rho_0 = (\rho_A + \rho_B)/2$ and viscosity $\nu = (\nu_A + \nu_B)/2$, where ρ_A, ρ_B, ν_A and ν_B are the original densities and viscosities of the system that we are approximating with the Boussinesq equations. Analogously, for this symmetrical system an upper bound for the respective dispersion relation $\sigma(k)$ can be obtained by looking for a solution of the form $h(\mathbf{x}, t) \sim e^{ikx+\sigma(k)t}$ in the Boussinesq system [88, 15], which gives

$$\sigma(k) = -\nu k^2 + \sqrt{\tilde{g}k - \frac{\gamma}{2\rho_0}k^3 + (\nu k^2)^2}, \tag{4.10}$$

where $\tilde{g} = \mathcal{A}g$ is the effective gravity, $\mathcal{A} = (\rho_A - \rho_B)/(\rho_A + \rho_B)$ is the Atwood number and g is the usual gravity. This upper bound is know to be a good approximation of the actual value of the growth rate measured in the simulations [88, 15]. For the problem of the dispersion relation presented in Chapter 2, another solution for the system formed by (2.31) and (2.35) is given by

$$\overline{\sigma}(k) = -\nu k^2 - \sqrt{\tilde{g}k - \frac{\gamma}{2\rho_0}k^3 + (\nu k^2)^2}, \tag{4.11}$$

originating a stable solution in the perturbation analysis. This solution does not affect significantly the evolution of the perturbation $y = h(x, t)$, as we show in Fig. 4.3, and can be neglected.

Considering the viscous potential flow analysis employed in Chapter 2, we have

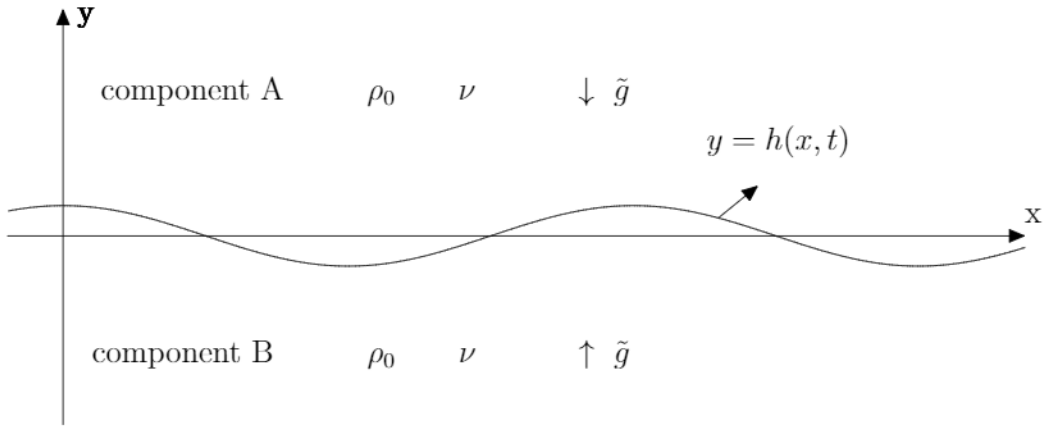

Figure 4.2: Unstable configuration characteristic of the Boussinesq approximation of the Rayleigh-Taylor instability. In this configuration, the components are accelerated against each other with the same buoyancy intensity $\tilde{g}$. In this configuration, any single mode perturbation $y = h(x,t)$, with a wave number smaller than some critical value can generate the instability.

the following potential functions for the velocity field of the system

$$\theta_A = \hat{\theta_A} e^{-ky} \cos(kx) e^{\sigma t} \text{ for } y > h, \tag{4.12}$$

$$\theta_B = \hat{\theta_B} e^{ky} \cos(kx) e^{\sigma t} \text{ for } y < h, \tag{4.13}$$

where $\hat{\theta_A}$ and $\hat{\theta_B}$ are the mode amplitudes. These potentials lead to the following vertical components of the velocities

$$u_y(x,y,t) = \begin{cases} -k\hat{\theta_A} e^{-ky} \cos(kx) e^{\sigma t} \text{ for } y > h \\ \\ k\hat{\theta_B} e^{ky} \cos(kx) e^{\sigma t} \text{ for } y < h, \end{cases} \tag{4.14}$$

Considering a perturbation of the form $h(x,t) = h_0 \cos(2\pi k/Nx)$, for $k \in \mathbb{N}$, in a domain with size $Nx \times Ny$, we have the following [25]

$$\langle u_y^2 \rangle = \frac{1}{NyNx} \int_{-Ny/2}^{0} dy \int_0^{Nx/2} (u_y)^2 dx + \frac{1}{NyNx} \int_0^{Ny/2} dy \int_0^{Nx/2} (u_y)^2 dx \tag{4.15}$$

$$= \frac{\overline{k}(\hat{\theta_A}^2 + \hat{\theta_B}^2)}{Ny} \left[1 - \frac{e^{-Ny\overline{k}}}{2} \right] e^{2\sigma(\overline{k})t}. \tag{4.16}$$

where $\overline{k} = \frac{2\pi k}{Nx}$. Applying logarithm in both sides of (4.16) the equation above we have

$$\ln \sqrt{\langle u_y^2 \rangle} \propto \sigma(\overline{k}) t. \tag{4.17}$$

It means that we can approximate the values of the dispersion relation (4.10) by analysing the mean square root of the vertical component of the velocity u_y. This procedure is employed in the experiments showed in the Figures 4.3(b) and 4.3(d), where we show the results of the dispersion relation analysis for a lattice Boltzmann simulation in a grid of size $Nx \times Ny = 256 \times 256$, relaxation time $\tau = 1.00$ and interaction parameter $G_{AB} = 1.22$. This choice of parameters provides the kinematic viscosity $\nu = 0.167$ and a surface tension coefficient $\gamma = 0.061$. The numerical data (blue and red circles) is obtained via best fit of $\ln \sqrt{\langle u_y^2 \rangle}$.

In Figures 4.3(a) and 4.3(c), the same experiment is repeated with the data for the dispersion relation obtained by measuring the exponential growth of the maximum interface displacement. We can see a good agreement between theoretical results and the lattice Boltzmann measurements. The best agreement comes from the analysis of the maximum interface displacement.

4.3 The anisotropy of the Shan-Chen model

Spurious currents are caused by numerical approximations of the surface tension force. If the numerical discretization is not perfectly isotropic then tangential force components originate spurious effects. In many cases, the spurious currents are significantly slower than the characteristic flow. In this situations, we may not need to take without additional care of the spurious currents [55]. For a better understanding of the reasons for the spurious currents we need to expand the Shan-Chen force as

$$\mathbf{F}_s^{SC}(\mathbf{x}) = -\rho_s(\mathbf{x}) G_{s\bar{s}} \sum_i w_i \rho_{\bar{s}}(\mathbf{x} + \mathbf{c}_i)\mathbf{c}_i, \tag{4.18}$$

and look to the high order terms. Analogously to what was done in chapter 2, let us expand each density $\rho_s(\mathbf{x} + \mathbf{c}_i\Delta t)$ about $\mathbf{x}$

$$\rho_s(\mathbf{x} + \mathbf{c}_i\Delta t) = \rho_s(\mathbf{x}, t) + c_i^a \partial_a \rho_s(\mathbf{x}, t) + \frac{1}{2} c_i^a c_i^b \partial_a \partial_b \rho_s(\mathbf{x}, t) + \frac{1}{6} c_i^a c_i^b c_i^c \partial_a \partial_b \partial_c \rho_s(\mathbf{x}, t) + \cdots \tag{4.19}$$

Including expansion terms from (4.19) up to fifth order, the continuum form of the total Shan-Chen force $\mathbf{F}^{SC} = \mathbf{F}_A^{SC} + \mathbf{F}_B^{SC}$ becomes

$$\begin{aligned} \mathbf{F}^{SC}(\mathbf{x}, t) &= \left(-c_s^2 G_{AB} \nabla(\rho_A \rho_B) - \frac{c_s^4}{2} \rho_A(x, t) \nabla \Delta \rho_B(x, t) - \frac{c_s^4}{2} \rho_B(x, t) \nabla \Delta \rho_A(x, t) \right) + \\ &+ \mathbf{F}^{aniso}. \end{aligned} \tag{4.20}$$

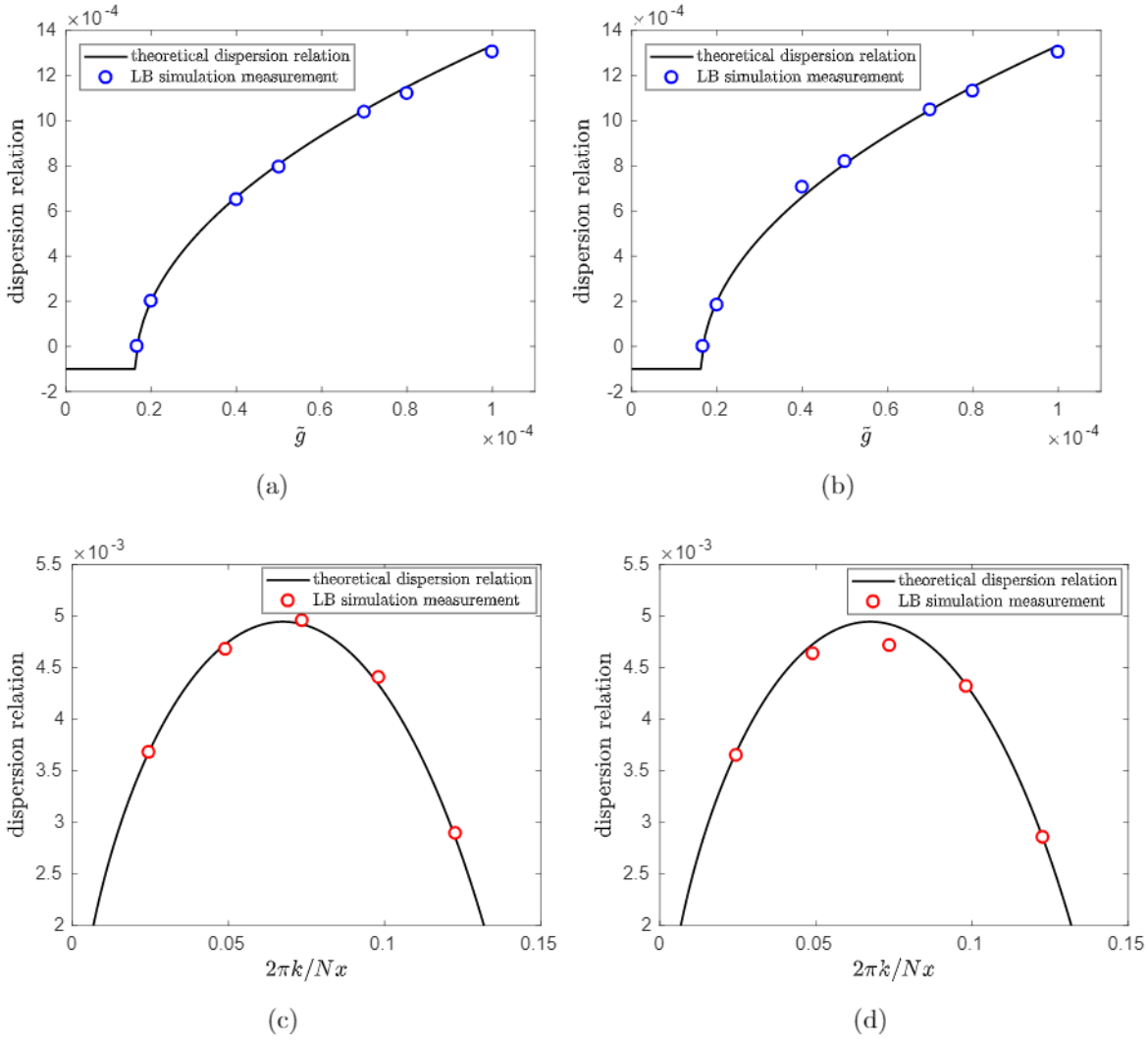

Figure 4.3: (a) Dispersion relation obtained by measuring exponential growth of the maximum interface displacement in a grid $Nx \times Ny = 256 \times 256$ for lattice Boltzmann simulations (blue circles) compared to the theoretical results for the immiscible RT system (black curve). This experiment considers different values of the effective gravity $\tilde{g} = \mathcal{A}g$ for a fixed $k = 2\pi/256$. In the picture (b) the same experiments is performed with the dispersion relation obtained from the root mean square of the vertical component of the velocity. In (c) the dispersion relation obtained by measuring exponential growth of the maximum interface displacement in a grid $Nx \times Ny = 256 \times 256$ for lattice Boltzmann simulations (red circles) compared to the theoretical results for the immiscible RT system (black curve). This experiment considers different wave numbers, $k = 1, 2, 3, 4, 5$, for a fixed effective gravity $\tilde{g} = 0.0006$. In picture (d) we repeat the experiment in (c) but calculating the dispersion relation using the root mean square of the vertical component of the velocity field. Error bars for fitting are approximately the size of the data symbols.

Up to the fourth-order, the isotropic terms lead to radial forces and the fifth-order term generates a tangential component [55]

$$\mathbf{F}^{aniso} \propto G_{AB}\rho_A(\partial_y^5\mathbf{e}_y + \partial_x^5\mathbf{e}_x)\rho_B + G_{AB}\rho_B(\partial_y^5\mathbf{e}_y + \partial_x^5\mathbf{e}_x)\rho_A \tag{4.21}$$

originates tangential force components responsible by the spurious currents showed in Fig. 4.4(b). Essentially, these currents are caused by limitation in the discretization of the interaction force $\mathbf{F}^{SC}$.

The effects of the anisotropy contributions can be reduced by a refinement of the curved interfaces [4], which helps to soften the local density gradients, or by improving the isotropy of the discretized pseudo-potential. The first method is considered more effective, leading to a numerical reduction of the maximal current up to a factor 10 with only a doubling in the grid resolution. The improvement of the isotropy can be archived by the using of a multirange interaction force scheme, which involves large numerical stancils involving lattice nodes at greater distances [55, 89]. An affect analogous to the stretching of the interface given by the grid refinement can be obtained by a simply rescaling of the coupling strengths with the reference density of the pseudopotential [80]. By this way, it is possible to achieve an adaptive form of local grid refinement without changing the structure of the lattice nodes.

In this thesis, we work mainly considering $\Delta x = \Delta y = \Delta t = 1$ for reasons associated with the stability of the numerical schemes, which is usually the main problem in simulations of the immiscible Rayleigh-Taylor systems for high Reynolds numbers. Discussion of grid refinements and multirange pseudopotential schemes are considered topics for future research in this thesis.

4.4 Spurious currents in the vorticity field

In our experiments of the Rayleigh-Taylor instability in Chapters 5 and 6, our focus is on the late stages of the instability characterized by high Reynolds numbers. In this context, we do not expect a significant influence of the spurious currents in the large scale statistics for the velocity field and order parameter, but we may have some influence in the small scale statistics, like those from the vorticity and enstrophy evolution. In Fig. 4.5, we show a comparison between the typical values of the spurious

vorticity and the characteristic vorticities in the miscible and immiscible Rayleigh-Taylor turbulence. It is possible to see that the spurious vorticity of a generic droplet is comparable to the vorticity in the miscible case.

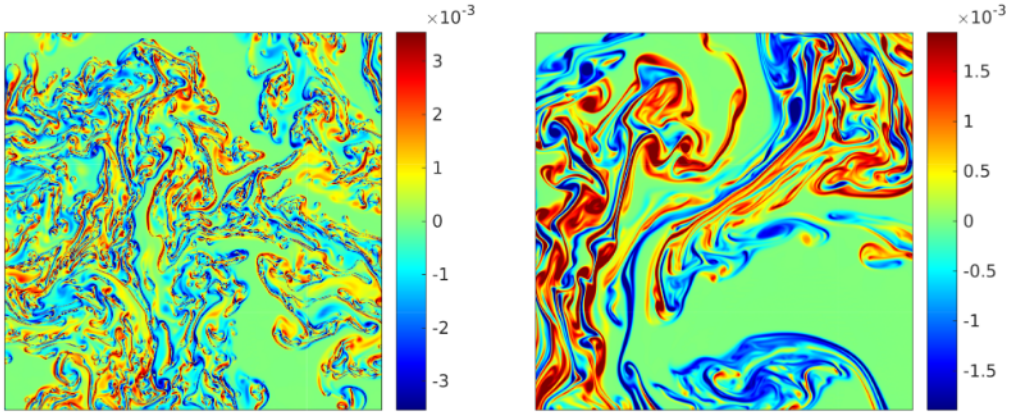

(a) (b)

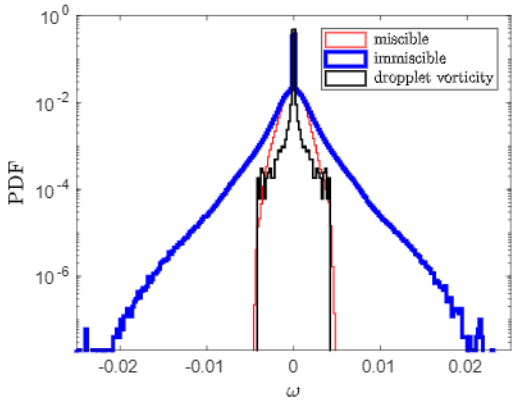

(c)

Figure 4.5: (a) Example of vorticity field for immiscible and (b) miscible flow described in Chapter 3. PDFs of the vorticity fields for immiscible (blue line) and miscible flows (red line) compared with the PDF of the spurious vorticity of the dropplet shown in Fig. 4.4(a). The region showed in pictures (a) and (b) corresponds to the time $t = 83.000$ in Figures 1.3 and 1.4.

To investigate the possible spurious influence we separate the bulk vorticity in the immiscible case by excluding small areas around the interface. This is done numerically by removing all nodes within squares of size 6×6, 8×8 and 10×10 at each point of the interface, as exemplified in Figures 4.6(a) and 4.7(a).

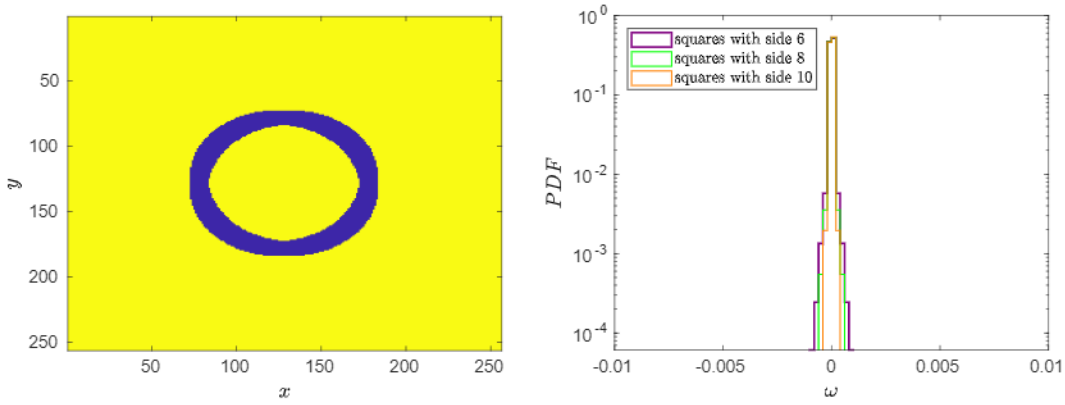

(a) (b)

Figure 4.6: (a) In blue we show an indication of the region excluded around the interface by removing all nodes within squares of size 10×10 at each point of the interface of the droplet in Fig. 4.4(a). In picture (b) we show the PDFs of the vorticity fields obtained by excluding squares of size 6×6, 8×8 and 10×10 around the interface of the same droplet.

The filtered vorticity for immiscible RT instability is plotted in Fig. 4.7(a). In Fig. 4.7(b) we plot PDFs of vorticity: one can see that the PDFs for the miscible (red) and filtered immiscible (purple, orange and green) flows are close, while the PDF for the full immiscible flow favors much larger values of vorticity characteristic of thin boundary layers. This observation also suggests that the immiscible flow in the regions away from the interface features turbulent statistics similar to the miscible flow. Even more, the normalized PDFs of vorticity shown in Fig. 4.7(c) reveals a distinctive shape of the tails for large ω, which is the same for the original and filtered fields in the immiscible flow.

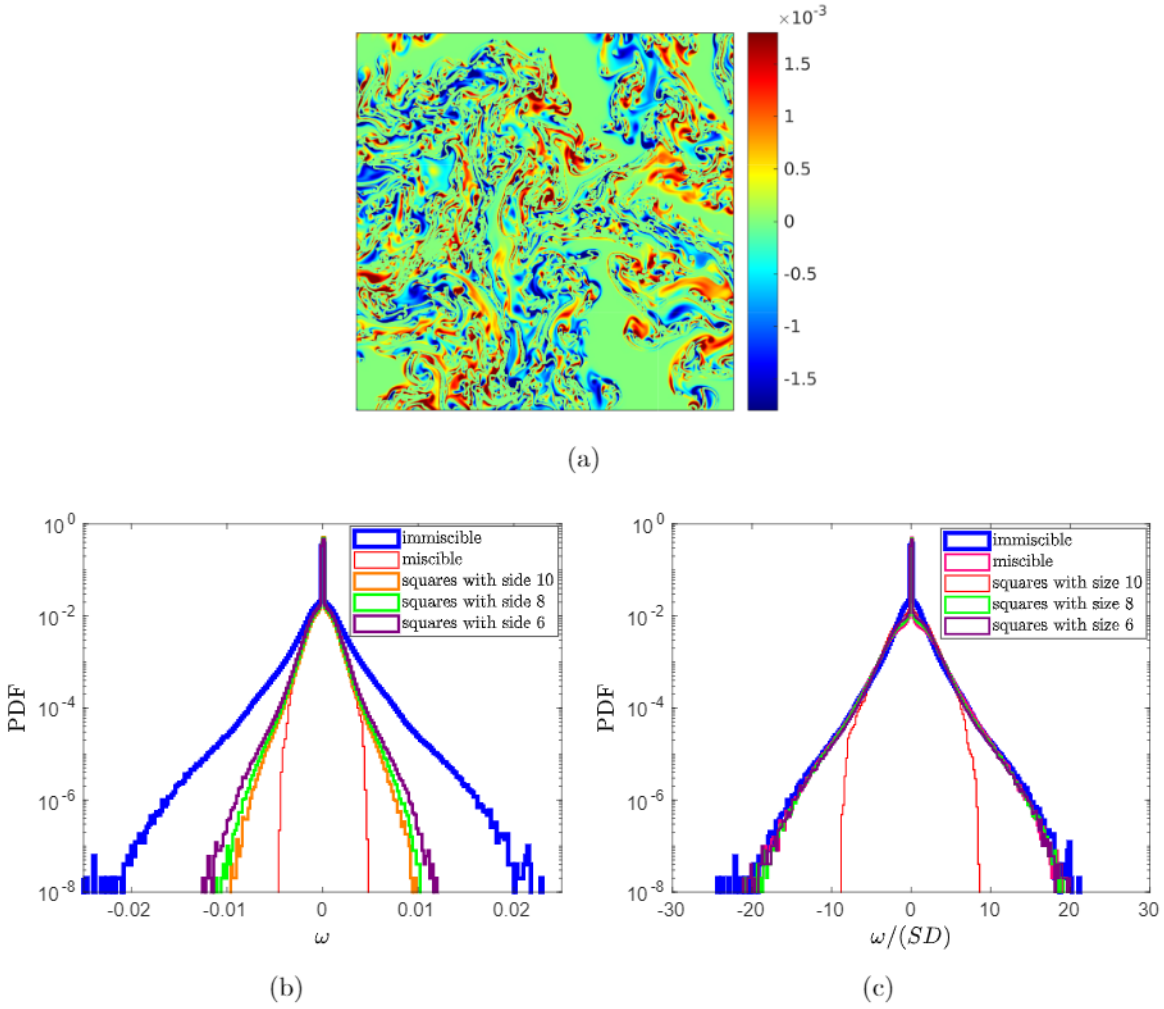

Figure 4.7: (a) Example of vorticity field for immiscible flow excluding a small region around the interface formed by removing all nodes within squares of size 8×8 at each point of the interface. (b) Comparison between PDFs of the miscible and immiscible RT turbulence and the PDFs of the filtered vorticity fields obtained by removing all nodes within squares of size 6×6, 8×8 and 10×10 at each point of the interface.

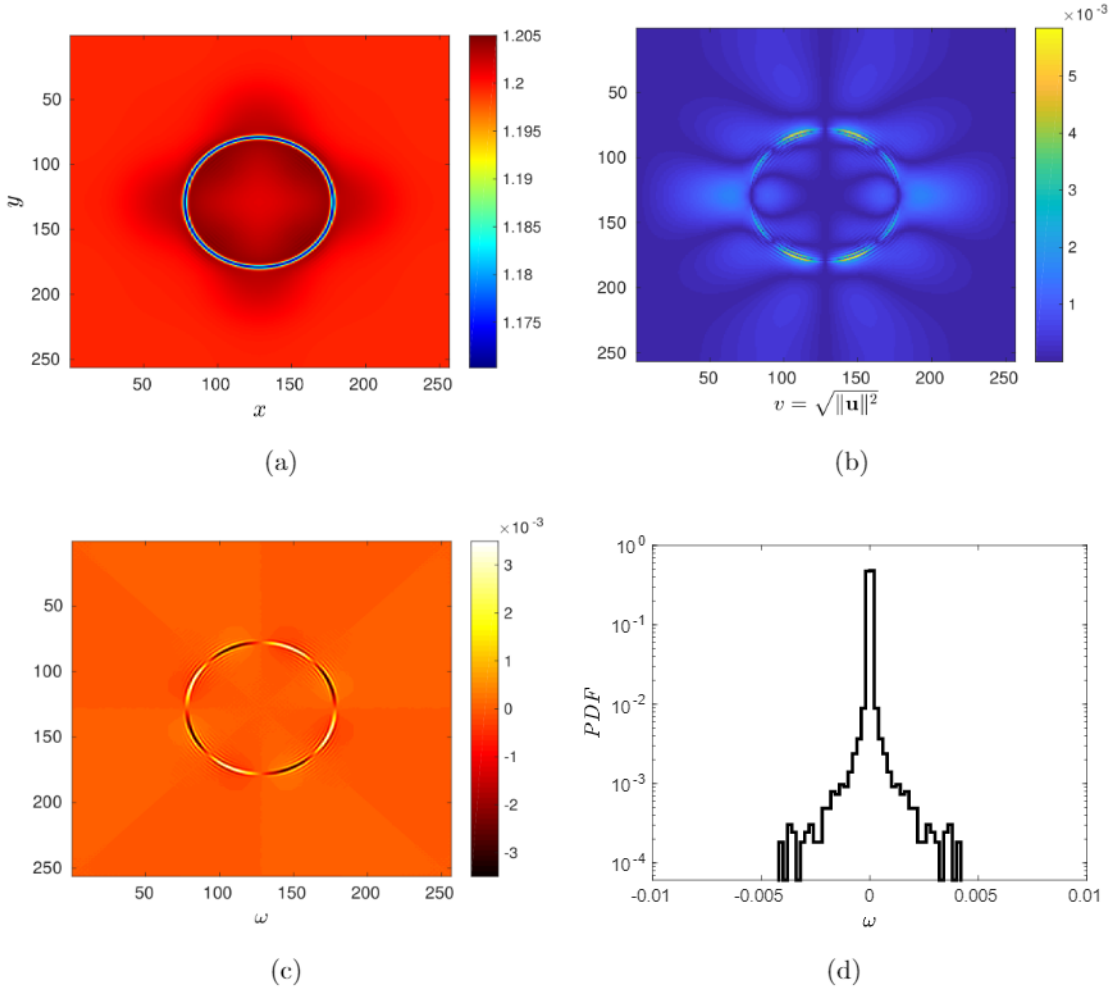

Figure 4.4: (a) Total density field $\rho = \rho_A + \rho_B$ in a droplet with radius R=51.2. In the pictures (b) and (c) we shown, respectively, the spurious velocities and vorticities of the droplet. In picture (d) we shown a pdf for the vorticity field showed in the picture (c). Simulations are performed on grids of size 256×256 with parameters corresponding to the relaxation time $\tau = 0.53$ and interaction parameter $G_{AB} = 0.1381$.

Chapter 5

Immiscible vs miscible Rayleigh-Taylor turbulence: comparing energy budgets

In this chapter, we study the energy budget for the miscible and immiscible RT systems described in the previous chapters. To the best of our knowledge, no such kind of numerical experiments comparing miscible and immiscible Rayleigh-Taylor turbulence have been done in the scientific literature of this phenomenons. Our results for the miscible case are in agreement with recent results for the miscible case done by [12]. The equations of motion considered in this chapter are mostly based on the Boussinesq system defined in Chapter 3, but the same results can be obtained as well if we consider any other diffuse interface formulation of the same system (see Appendix A).

In this chapter, we first analyze the potential and kinetic energies of the system and its variations. By comparing the components of the kinetic energy variation of the system, we verify the accuracy of the Schan-Chen multicomponent method for miscible and immiscible RT turbulence. Thereafter, we show that the main differences between miscible and immiscible RT flows are associated to the energy flux due to the Korteweg stress tensor (3.109) and the viscous dissipation. In subsequent subsections, we show that the such differences are connected to the energy needed to generate interfaces and the vorticity generated by them.

In the numerical experiments of this section, we consider ensembles with at least 10 simulations for the immiscible and miscible flows performed for different random initial disturbances as we explained in Chapter 3; see Figures 5.1 and 5.2. The choice of the size of the ensembles for out statistical analysis is motivated by small values of standard deviations verified in our numerical experiments, indicating a small dependence on the initial conditions for big computational grids like the ones used by us. For smaller grids and early stages of turbulence, the influence of initial conditions was studied in [69, 8].

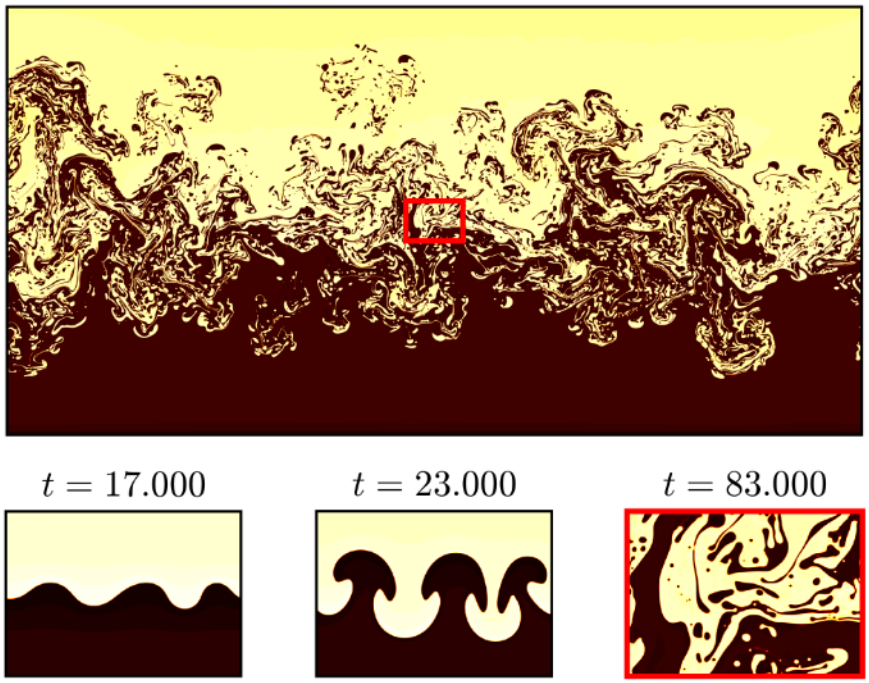

Figure 5.1: Mixing layer of the immiscible Rayleigh-Taylor turbulence, where the yellow color represents a heavier phase and the brown color corresponds to a lighter phase. Lower pictures show the phases in the small region (marked in the center of the main panel) for three different times: the initial linear growth, formation of nonlinear mushroom-like structures at intermediate times, and fully developed turbulent mixing at larger times. Simulations are performed on the grids 10.000×5.000 in lattice Boltzmann units (lbu), a simple artificial set of units with spatial and time steps verifying $\Delta t = \Delta x = \Delta y = 1$.

To avoid complications with the boundaries, the energy flows are calculated in a subdomain D obtained by cutting 10 rows close to the top and 10 rows close to the

bottom of the original computational domain. It means that D has the size $|D| = 10.000 \times 4.980$. The time derivatives and differential operators in the equations showed in this chapter are numerically calculated using centered finite difference schemes of second order.

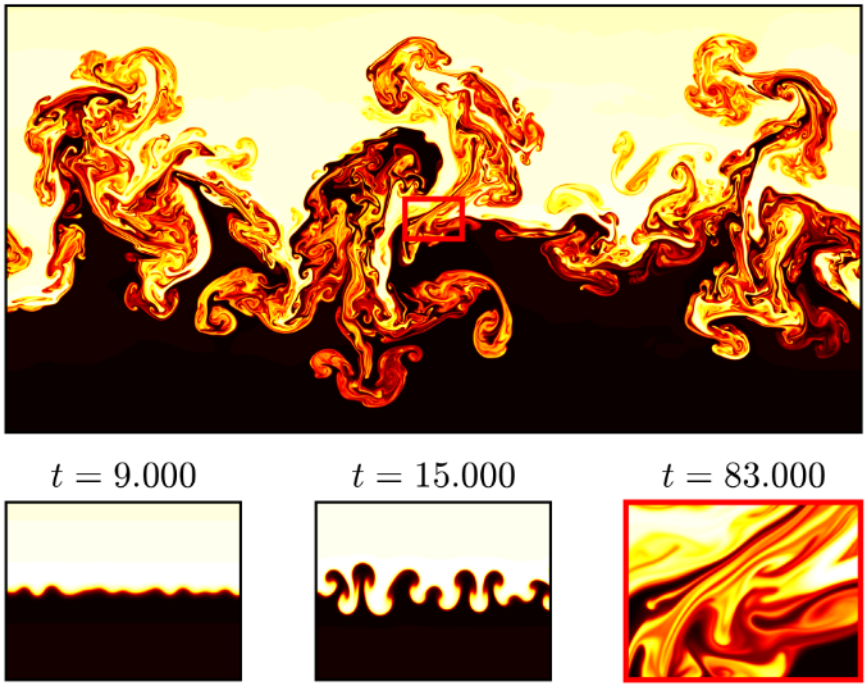

Figure 5.2: Mixing layer of the miscible Rayleigh-Taylor turbulence, where colors describe the fluid density; lighter colors represent a heavier fluid. Lower pictures show the densities in the small region (marked in the center of the main panel) for three different times: the initial linear growth, formation of nonlinear mushroom-like structures at intermediate times, and fully developed turbulent mixing at larger times. Simulations are performed on the grids 10.000×5.000 in lattice Boltzmann units (lbu), a simple artificial set of units with spatial and time steps verifying $\Delta t = \Delta x = \Delta y = 1$.

5.1 Potential and kinetic energy statistics

In this subsection, we develop the equation for the kinetic and potential energies of the system also showing the evolution of such energies for the immiscible and miscible RT system using numerical data from the Shan-Chen multicomponent method.

First, let us recall the equations for the Rayleigh-Taylor system developed in

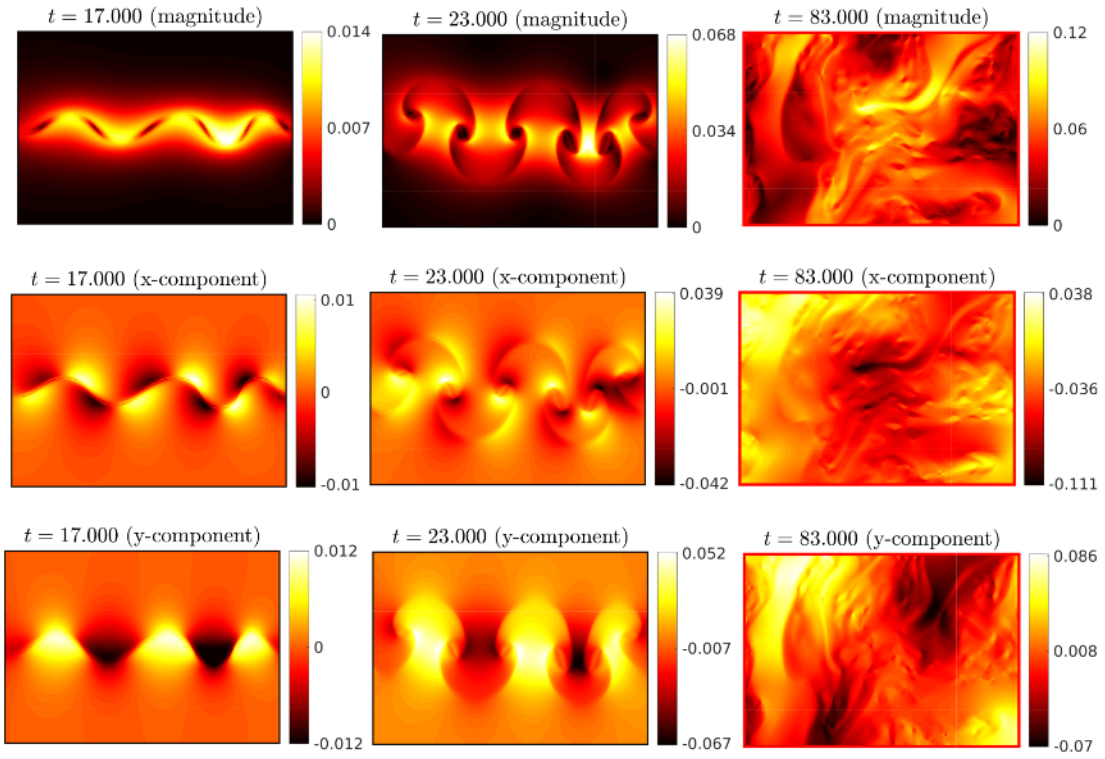

Figure 5.3: Components of the velocity field for the immiscible Rayleigh-Taylor flow shown in Fig 5.1. The velocities are indicated in simulation units.

Chapter 3:

$$\rho\left(\frac{\partial \mathbf{u}}{\partial t} + (\mathbf{u}\cdot\nabla)\mathbf{u}\right) = -\nabla\cdot\mathbf{P}^{(TOT)} + \nabla\cdot\left[\rho\nu(\nabla\mathbf{u} + \nabla\mathbf{u}^T)\right] - \phi\tilde{g}\mathbf{e}_y. \tag{5.1}$$

$$\nabla\cdot\mathbf{u} = 0, \tag{5.2}$$

$$\frac{\partial\phi}{\partial t} + \nabla\cdot(\phi\mathbf{u}) = \nabla\cdot\left[M\nabla\mu\right], \tag{5.3}$$

with $\mathbf{P}^{(TOT)}$ being the momentum-flux tensor

$$\mathbf{P}^{(TOT)} = p_b\mathbf{I} + \mathbf{P}^K + \mathbf{K}^{(\tau)} \tag{5.4}$$

where

$$p_b = c_s^2\rho + \frac{G_{AB}c_s^2}{4}(\rho^2 - \phi^2), \tag{5.5}$$

$$\mathbf{P}^K = \left[-\kappa\phi\Delta\phi - \frac{\kappa}{2}|\nabla\phi^2|\right]\mathbf{I} + \kappa\nabla\phi\otimes\nabla\phi, \tag{5.6}$$

$$\mathbf{K}^{(\tau)} = c_s^4\frac{\rho_A\rho_B}{\rho}\left(\tau - \frac{1}{2}\right)^2\left(\frac{\nabla\rho_A}{\rho_A} - \frac{\nabla\rho_B}{\rho_B}\right)\otimes\left(\frac{\nabla\rho_A}{\rho_A} - \frac{\nabla\rho_B}{\rho_B}\right). \tag{5.7}$$

and $k = c_s^4\dfrac{G_{AB}}{4}$ for the Shan-Chen method. The part $\mathbf{P}^k$ is called the Korteweg stress tensor [3, 50, 49]. By the definition of the potential energy (per unit of area) [25], we

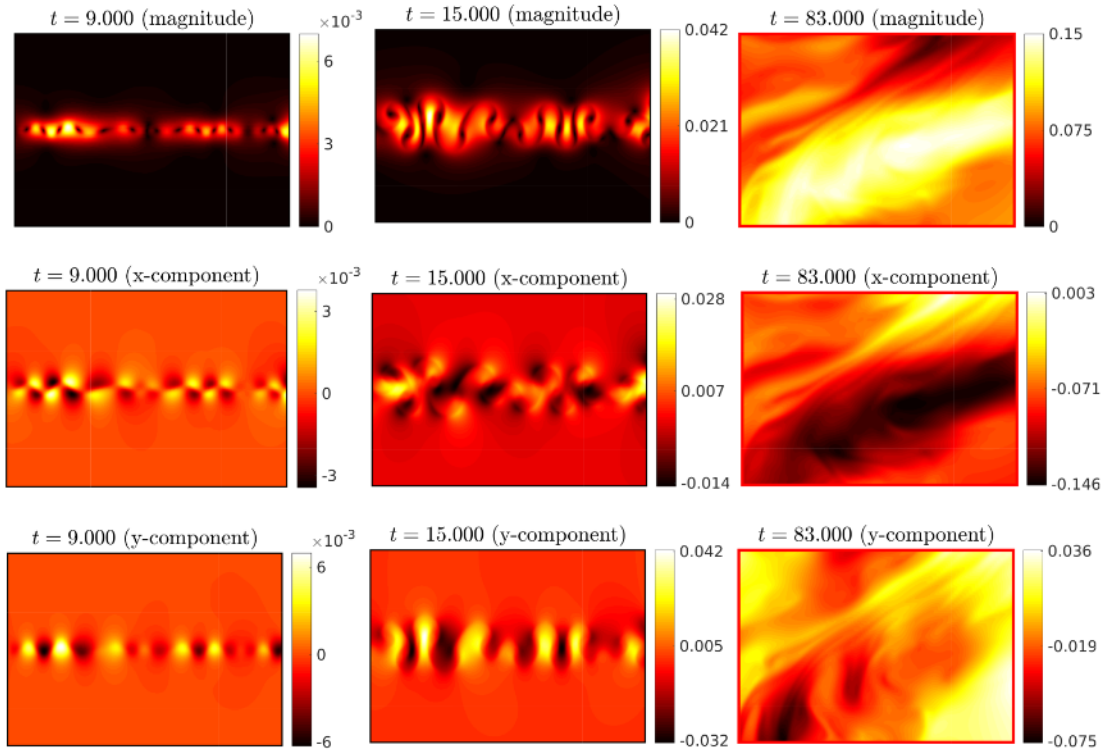

Figure 5.4: Components of the velocity field for the miscible Raleigh-Taylor flow shown in Fig. 5.2. The velocities are indicated in simulation units.

have

$$\begin{aligned} E_p &= \frac{1}{|D|}\int\int \rho_A \tilde{g} y dx dy - \int\int \rho_B \tilde{g} y dx dy \\ &= \tilde{g}\,\langle y\phi\rangle\,. \end{aligned} \tag{5.8}$$

where the brackets denotes spacial averages calculated in the subdomain D.

For the variation of the potential energy, we have

$$\begin{aligned} \partial_t E_p &= \frac{1}{|D|}\int\int \tilde{g} y \frac{\partial \phi}{\partial t} dx dy \\ &= \frac{1}{|D|}\int\int \tilde{g} y(-\nabla\cdot(\phi\mathbf{u}) + \nabla\cdot(M\nabla\mu)) dx dy \\ &= \tilde{g}\,\langle \phi\mathbf{u}\cdot\mathbf{e}_y\rangle\,. \end{aligned} \tag{5.9}$$

In the integration by parts, we consider the no-slip condition $\mathbf{u} = 0$ at the boundaries in the vertical direction and periodic boundary conditions in the horizontal direction.

In Fig. 5.5, we show a numerical verification of the relations (5.8) and (5.9). It is possible to see that no significant difference is observed in the potential energy statistics between miscible and immiscible flows.

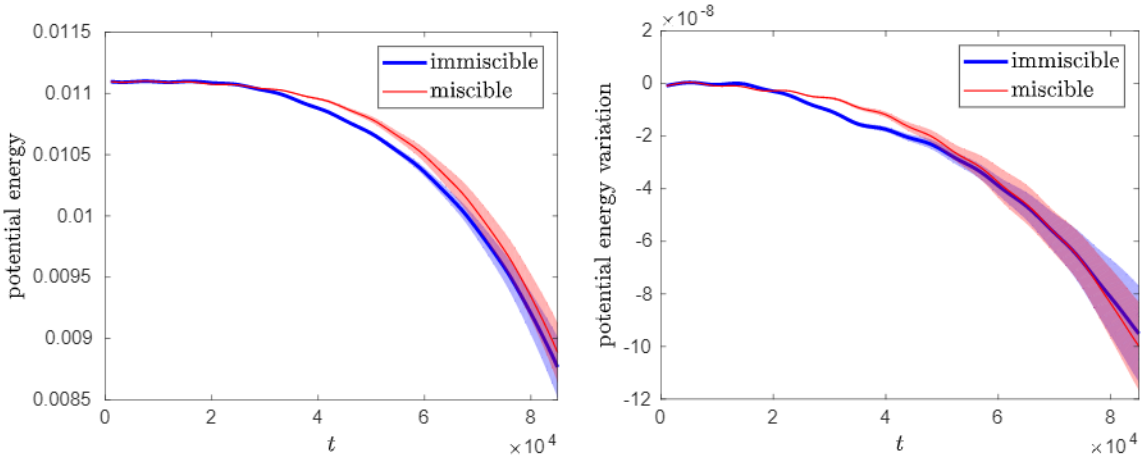

(a) (b)

Figure 5.5: (a)Evolution of the potential energy for miscible and immiscible flows. (b) Variation of the potential energy for miscible and miscible flows. The shaded regions corresponds to standard deviation values.

Analogously, the kinetic energy per unit of area can be defined as

$$E_K = \frac{1}{|D|}\int\int \rho_A \frac{\mathbf{u}^2}{2} dxdy + \frac{1}{|D|}\int\int \rho_B \frac{\mathbf{u}^2}{2} dxdy = \frac{1}{|D|}\int\int \rho \frac{\mathbf{u}^2}{2} dxdy, \tag{5.10}$$

where $\rho = \rho_A + \rho_B$. The respective variation will be given by

$$\begin{aligned}
\partial_t E_K &= \frac{1}{|D|}\int\int \left[\frac{\partial \rho}{\partial t}\frac{|\mathbf{u}|^2}{2} + \rho\mathbf{u}\cdot\frac{\partial \mathbf{u}}{\partial t}\right] dxdy \\
&= \frac{1}{|D|}\int\int \Big[-\nabla\cdot(\rho\mathbf{u})\frac{|u|^2}{2} + \rho\mathbf{u}\cdot(-(\mathbf{u}\cdot\nabla)\mathbf{u} - \\
&- \nabla\cdot\mathbf{P}^{(TOT)} + \nabla\cdot\left(\eta\nabla\mathbf{u} + \eta\nabla^T\mathbf{u}\right) + \phi\overrightarrow{g}\Big)\Big] dxdy \\
&= \frac{1}{|D|}\int\int \left[-\nabla(\rho\mathbf{u})\frac{|\mathbf{u}|^2}{2} - \rho\mathbf{u}\cdot(\mathbf{u}\cdot\nabla)\mathbf{u}\right] dxdy - \\
&- \left\langle\mathbf{u}\cdot(\nabla\cdot\mathbf{P}^{(TOT)})\right\rangle + \left\langle\mathbf{u}\cdot\nabla\cdot\left(\eta\nabla\mathbf{u} + \eta\nabla\mathbf{u}^T\right)\right\rangle + \left\langle\mathbf{u}\cdot\phi\overrightarrow{g}\right\rangle
\end{aligned} \tag{5.11}$$

where $\eta = \rho\nu$ is the dynamic viscosity. Using that

$$\mathbf{u}\cdot(\mathbf{u}\cdot\nabla)\mathbf{u} = \mathbf{u}\cdot\nabla\frac{|\mathbf{u}|^2}{2}, \tag{5.12}$$

we have

$$\int\int \left[-\nabla(\rho\mathbf{u})\frac{|\mathbf{u}|^2}{2} - \rho\mathbf{u}\cdot(\mathbf{u}\cdot\nabla)\mathbf{u}\right] dxdy = \int_{\partial\Omega} -\rho\frac{|\mathbf{u}|^2}{2}\mathbf{u}\cdot d\mathbf{s} = 0,$$

as a consequence of the boundary conditions considered. We can see three different

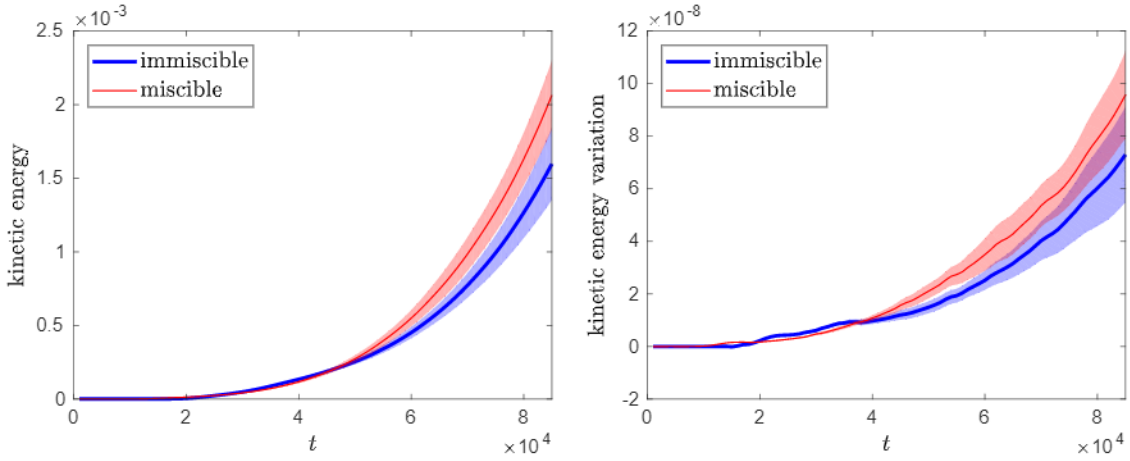

(a) (b)

Figure 5.6: (a)Evolution of the kinetic energy of for miscible and immiscible flows. (b) Variation of the kinetic energy for miscible and miscible flows. The shaded regions corresponds to standard deviation values.

contributions to the kinetic energy variation:

$$\begin{aligned} &- \text{Contribution of the momentum-flux tensor} = -\left\langle \mathbf{u} \cdot (\nabla \cdot \mathbf{P}^{(TOT)}) \right\rangle, \\ &- \text{Contribution of the viscous term} = \left\langle \mathbf{u} \cdot (\nabla \cdot \left(\eta \nabla \mathbf{u} + \eta \nabla \mathbf{u}^T\right)) \right\rangle, \\ &- \text{Contribution of the buoyancy term} = \left\langle \mathbf{u} \cdot \phi \tilde{g} \mathbf{e}_y \right\rangle. \end{aligned} \tag{5.13}$$

A direct comparison between the kinetic energy statistics miscible and immiscible can be seen in Fig. 5.7. It is possible to see that the kinetic energy in the miscible case grows faster than in the immiscible case. In Fig. (5.8) we can see that this difference associated with the contribution of the terms $\nabla \cdot \mathbf{P}$ and $\nabla \cdot \left(\eta \nabla \mathbf{u} + \eta \nabla \mathbf{u}^T\right)$. In Figures 5.7(c) and 5.7(d), we verify the balance (5.11), giving strong indications that the solutions for the order parameter ϕ and the velocity field $\mathbf{u}$ given by the Shan-Chen multicomponent method, satisfy accurately the proposed system (5.1), (5.2) and (5.3).

The contribution of the momentum flux tensor, responsible for the effects of the surface tension in the immiscible Rayleigh-Taylor system, is negligible in comparison with the contribution of the buoyancy and the viscous terms. This result has important implications in the analysis of the long time behavior of Rayleigh-Taylor systems, as we show in the Chapter 6.

The components of the kinetic energy variation (5.13) are analyzed in Fig. 5.8. In these figures, it is possible to observe that the main differences between miscible

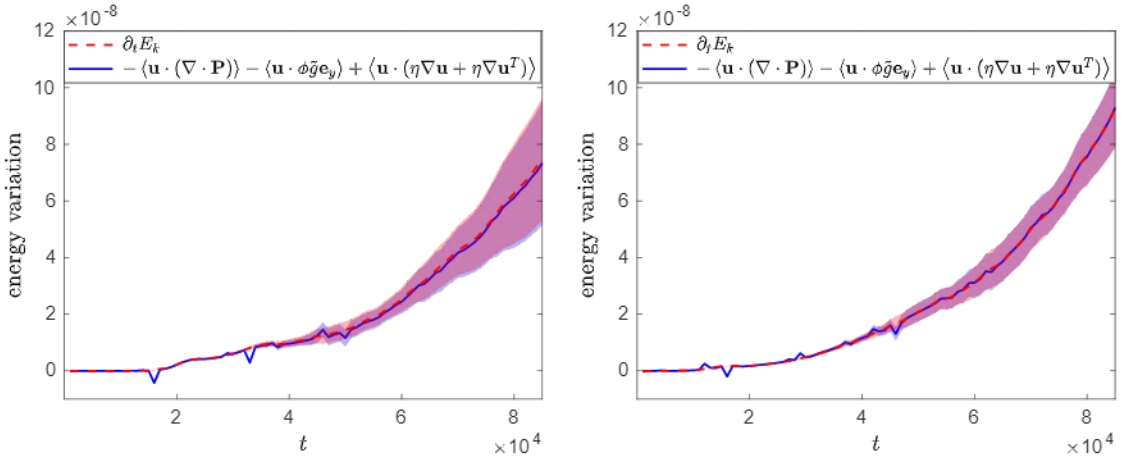

Figure 5.7: (a) Evolution of the kinetic energy of the for miscible and immiscible flows. (b) Variation of the kinetic energy of the for miscible and miscible flows. Verification of the kinetic energy balance (5.11) for immiscible (c) and miscible (d) flows. The shaded regions corresponds to standard deviation values.

and immiscible flows are associated with the terms $\nabla\cdot\mathbf{P}$ and $\nabla\cdot\left(\eta\nabla\mathbf{u}+\eta\nabla\mathbf{u}^T\right)$.

In Fig. 5.15, we analyze the decomposition

$$\left\langle \mathbf{u}\cdot(\nabla\cdot\mathbf{P}^{(TOT)})\right\rangle = \langle \mathbf{u}\cdot\nabla p_b\rangle + \left\langle \mathbf{u}\cdot(\nabla\cdot\mathbf{P}^{k})\right\rangle + \left\langle \mathbf{u}\cdot(\nabla\cdot\mathbf{K}^{(\tau)})\right\rangle, \tag{5.14}$$

showing that the contribution of the spurious term $\mathbf{K}^{(\tau)}$ is negligible in comparison with all the other contributions and does not generate a significant impact in the measurements of the energy flux. Another significant difference between miscible and immiscible flows is related to the Korteweg stress tensor $\mathbf{P}^K$. In the next subsections we show that this difference is connected to the portion of kinetic energy which is converted into the energy of interface. The energy flux $\langle \mathbf{u}\cdot\nabla p_b\rangle$ is similar between miscible and immiscible flows, and the oscillatory aspect is essentially caused by density fluctuations due to the initialization process of the lattice-Boltzmann algorithm.

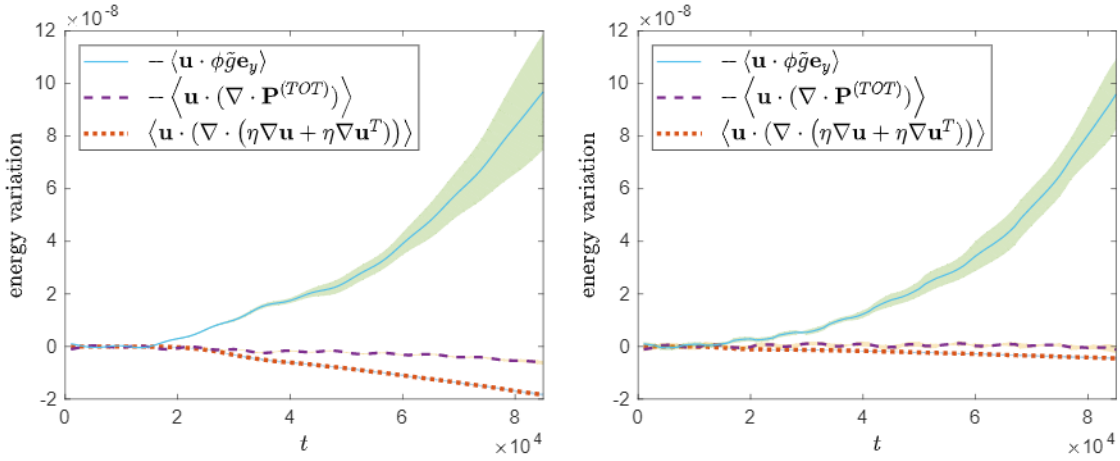

(a) (b)

Figure 5.8: (a) Components of the kinetic energy variation for (a) immiscible flows and for (b) the miscible flows. The shaded regions corresponds to standard deviation values.

5.2 Energy of the interface

If we ignore the gradients of the total density and the spurious contribution $\mathbf{K}^{(\tau)}$, we can simplify the contribution of the momentum-flux tensor in (5.13) as

$$\begin{aligned}\left\langle \mathbf{u}\cdot(\nabla\cdot\mathbf{P}^{(TOT)})\right\rangle &= \langle \mathbf{u}\cdot\nabla p_b\rangle - \langle \mathbf{u}\cdot(\phi\nabla(\Delta\phi))\rangle \\ &= -\langle(\nabla\cdot\mathbf{u})p_b\rangle + \langle \mathbf{u}\cdot\nabla\phi\Delta\phi\rangle + \langle(\nabla\cdot\mathbf{u})\phi\Delta\phi\rangle \\ &= \langle \mathbf{u}\cdot\nabla\phi\Delta\phi\rangle\,.\end{aligned} \tag{5.15}$$

In this subsection, we analyze the right hand side of (5.15), showing that this flux corresponds to the variation of the total energy of the interface. For this purpose, we first need to introduce some concepts of differential geometry of plane regular closed curves.

5.2.1 Some general results about plane regular curves

Consider initially a closed, simple and regular curve in $\mathbb{R}^2$ parametrized by some function $\mathbf{R} = \mathbf{R}(s),\ s \in I \subset \mathbb{R}$. Let us introduce a normal coordinates system that moves with the interface [32], i.e.,

$$\mathbf{x}(s,u) = \mathbf{R}(s) + u\mathbf{n}(s), \tag{5.16}$$

where $\mathbf{R}(s)$ indicates the positions of the interface, s is the arc length parameter, $\mathbf{n}(s)$ is the unit vector normal to the interface calculated at s and u is a parameter related to the distance with respect to the interface in the normal direction. Naturally, the center of the interface is given by $\mathbf{x}(s,0) = \mathbf{R}(s)$, and we define

$$\mathbf{t} \equiv \frac{d\mathbf{R}}{ds}, \tag{5.17}$$

as the unit tangent vector to the interface at s. It also implies $\mathbf{t}\cdot\mathbf{n} = 0$. The relationship between the fields $\mathbf{t}$ and $\mathbf{n}$ and the curvature K is given by the Frenet formulas [34]

$$\frac{d\mathbf{t}}{dt} = K\mathbf{n}, \quad \frac{d\mathbf{n}}{dt} = -K\mathbf{t}. \tag{5.18}$$

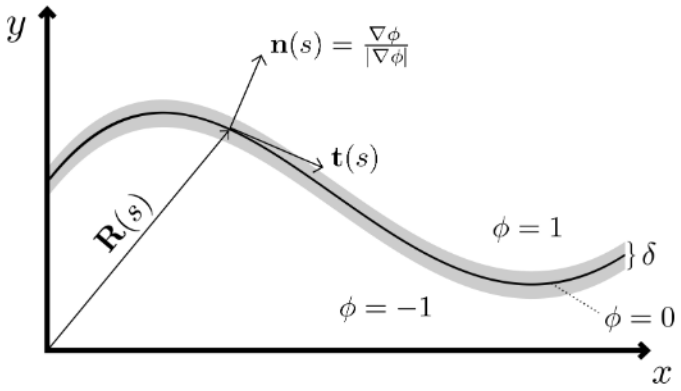

Figure 5.9: Schematic representation of the normal coordinates system. The indication of the components is indicated by values of the function ϕ. The length δ is the interface width (see Appendix A). If the curve is the the level set of some function ϕ then we can represent the normal to the curve by the field $\mathbf{n} = \nabla\phi/|\nabla\phi|$.

A very important consequence of the Frenet formulas is the following relation

$$\nabla\cdot\mathbf{n} = \left(\mathbf{n}\frac{\partial}{\partial u} + \mathbf{t}\frac{\partial}{\partial s}\right)\cdot\mathbf{n} = \mathbf{t}\cdot\frac{\partial\mathbf{n}}{\partial s} = -\mathbf{t}\cdot K(s)\mathbf{t} = -K(s). \tag{5.19}$$

If the interface is an implicit planar curve $\phi(x,y) = 0$, then the normal field can be defined as $\mathbf{n} = \frac{\nabla\phi}{|\nabla\phi|}$, which gives

$$K(s) = -\nabla\cdot\left(\frac{\nabla\phi}{|\nabla\phi|}\right). \tag{5.20}$$

5.2.2 Evolution of time dependent plane curves

To study the evolution of the energy of the interface in the immiscible Rayleigh-Taylor turbulence is useful to understand some concepts of differential geometry of families of plane closed curves that evolve in time.

Consider a family of closed smooth plane curves. In this case we can consider a time dependent parametrization $\mathbf{R} = \mathbf{R}(s,t)$ for the family, where s is the time-dependent arc length parameter and t indicates the time parameter defined for some interval $[0,T)$. Analogously, the tangent to a curve at s is given by $\mathbf{t}(s,t) = \partial\mathbf{R}(s,t)/\partial s$, with the variations of the tangent and normal with the arc length given by

$$\partial\mathbf{t}(s,t)/\partial s = K(s,t)\mathbf{n}(s,t), \tag{5.21}$$

$$\partial\mathbf{n}(s,t)/\partial s = -K(s,t)\mathbf{t}(s,t), \tag{5.22}$$

where $K = K(s,t)$ is the time-dependent scalar curvature. The fact that $\mathbf{t}\cdot\frac{\partial\mathbf{t}}{\partial t} = 0$ and $\mathbf{n}\cdot\frac{\partial\mathbf{n}}{\partial t} = 0$, leads to [32]

$$\frac{\partial\mathbf{t}(s,t)}{\partial t} = \alpha\mathbf{n}(s,t), \quad \frac{\partial\mathbf{n}(s,t)}{dt} = -\alpha\mathbf{t}(s,t), \tag{5.23}$$

where α is proportionality function.

The velocity $\partial\mathbf{R}(s,t)/\partial t$ can be decomposed into normal $v_N(s,t)$ and tangential $v_T(s,t)$ components, i. e.,

$$\frac{\partial\mathbf{R}(s,t)}{\partial t} = v_N(s,t)\mathbf{n}(s,t) + v_T(s,t)\mathbf{t}(s,t). \tag{5.24}$$

Define $\Gamma^t = \text{Image}(R(\cdot,t))$ as the evolution of some initial closed curve $\Gamma = \Gamma^0 = \text{Image}(R(\cdot,0))$. The variation of the total length $\mathcal{L}^t = \mathcal{L}(\Gamma^t)$ of the curve Γ^t can be associated with the curvature K and the normal velocity v_N by the following equation [84]

$$\frac{d}{dt}\mathcal{L}_t + \int_{\Gamma^t} K(s,t)v_N(s,t)ds = 0. \tag{5.25}$$

This formula can be is naturally generalized for interfaces with many closed components.

In the following calculations we give an idea on how to derive the relation (5.25). Let us reparametrize Γ^t by a difeomorfism Φ such that $s = \Phi(u)$, where $u \in [0,1)$ such

that $ds/du = |R_u|$, for any $t > 0$ [84] (since we are considering the evolution of closed curves). We have

$$\frac{\partial}{\partial t} R_u = \frac{\partial}{\partial u} R_t. \tag{5.26}$$

The left hand side of (5.26) gives

$$\begin{aligned} \frac{\partial}{\partial t} R_u &= \frac{\partial}{\partial t}(|R_u|\mathbf{t}) \\ &= \frac{\partial |R_u|}{\partial t}\mathbf{t} + |R_u|\frac{\partial \mathbf{t}}{\partial t}, \\ &= \frac{\partial |R_u|}{\partial t}\mathbf{t} + |R_u|\alpha\mathbf{n}. \end{aligned} \tag{5.27}$$

and from the right hand side of (5.26), we have [32]

$$\begin{aligned} \frac{\partial R_t}{\partial u} &= \frac{\partial R_t}{\partial s}\frac{\partial s}{\partial u} \\ &= \frac{\partial R_t}{\partial s}|R_u| \\ &= \left(\frac{\partial v_N}{\partial s}\mathbf{n} + v_N\frac{\partial \mathbf{n}}{\partial s} + \frac{\partial v_T}{\partial s}\mathbf{t} + v_T\frac{\partial \mathbf{t}}{\partial s}\right)|R_u| \\ &= \left(\frac{\partial v_N}{\partial s}\mathbf{n} - v_N K\mathbf{t} + \frac{\partial v_T}{\partial s}\mathbf{t} + v_T K\mathbf{n}\right)|R_u| \end{aligned} \tag{5.28}$$

Comparing (5.28) and (5.27) in the tangential direction $\mathbf{t}$, we obtain

$$\frac{\partial |R_u|}{\partial t} + v_N K|R_u| = \frac{\partial v_T}{\partial s}|R_u|. \tag{5.29}$$

By integrating (5.29) over the interval $[0, 1)$ and taking into account that $\partial v_T/\partial s$ satisfies periodic boundary conditions, we obtain the total length equation (5.25).

The relation (5.25) will be useful in the next subsections to establish a clear link between the variation of the total length of the interface and the energy flux associated with the Korteweg stress tensor $\mathbf{P}^K$.

In the next subsections, for the seek of clarity, we omit the time dependence of the developed equations. This dependence will be given by the context of the calculations.

5.2.3 Cauchy-Crofton formula and total length of plane curves

The total energy of the interface in the immiscible Raleigh-Taylor flows is calculated by the product between the surface tension coefficient γ and the total length of the interface $\mathcal{L}$ [12]. Numerically, we calculate the total length of the interface using a numerical implementation of the Cauchy-Crofton formula [34, 61]. Specifically,

suppose that the interface forms a rectifiable plane curve Γ (or a union of rectifiable curves). Given an oriented line l, define $n(p,\xi)$ as the number of points where Γ intersects a given straight line C, where C is parametrized by the direction ξ with respect to the horizontal axis and by its signed distance p from the origin. The Crofton formula expresses the total length $\mathcal{L}(\Gamma)$ of the interface thought the following integral

$$\mathcal{L}(\Gamma) = \frac{1}{2}\int\int n(p,\xi)d\xi dp, \tag{5.30}$$

i.e., an integral over the space of all oriented lines. In the following calculations, we demonstrate the formula (5.30) for interfaces that are formed by polygonal lines.

In more specific terms, in $\mathbb{R}^2$ we can determine a strait line M by a unit vector $\mathbf{v} = (\cos\xi, \sin\xi)$ and the inter product $p = \mathbf{v}\cdot\alpha$ of $\mathbf{v}$ and the position $\alpha = (x,y)$ of L. To associate M with (p,ξ) we must identify $(p,\xi) \sim (p,\xi+2\pi k)$, $k \in \mathbb{Z}$, and $(p,\xi) \sim (-p,\xi)$. Thus, the set of all strait lines in $\mathbb{R}^2$ is represented by

$$\Lambda = \left\{(p,\xi) \in \mathbb{R}^2; (p,\xi) \sim (p,\xi+2\pi k) \text{ and } (p,\xi) \sim (-p,\xi)\right\}. \tag{5.31}$$

It is possible to define a measure for any subset $\Sigma \in \Lambda$ as

$$\int\int_{\Sigma} dpd\xi, \tag{5.32}$$

and it is possible to prove that this formula is, up to a constant factor, the only measure on Λ that is invariant under rigid motions [34].

Consider a curve C which is a segment of a straight line with length $\mathcal{L}$. Assume that the coordinate system has its origin 0 in the middle point of C and that the horizontal axis is in the direction of C. This assumption is a consequence of the fact that (5.32) is invariant under rigid motions. The measure of the set of straight lines that meet C is given by

$$\int\int dpd\xi = \int_0^{2\pi}\left(\int_0^{|\cos\xi|(l/2)} dp\right)d\xi = \int_0^{2\pi}\frac{l}{2}|\cos\xi|d\xi = 2\mathcal{L}. \tag{5.33}$$

Next, consider the situation where C is a polygonal line formed by a finite number of segments C_i with length $\mathcal{L}_i$ such that $\sum_i \mathcal{L}_i = \mathcal{L}$. Consider again $n(\xi,p)$ as the number of intersection points of the straight line with C. Then, applying (5.33) to each segment and summing up the results, we obtain

$$\int\int dpd\xi ndpd\xi = 2\sum_i \mathcal{L}_i = 2\mathcal{L}, \tag{5.34}$$

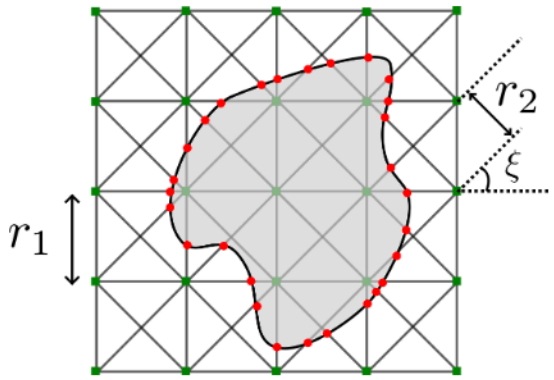

Figure 5.10: Schematic representation of the intersection of a curve with four families of straight lines. The intersections with these families are indicated by the red points. The grid points of the computational fluid domain are indicated by the points in green. Within the gray region limited by the interface, we have one fluid component, and outside, the other component. We count the number of intersections by looking for sign changes in the values of the order parameter ϕ between different grid points. Numerically, the four families of straight lines are families of sub-vectors formed by points of the computational grid. Every variation of the sign of ϕ in a sub-vector is counted as an intersection.

originating the Cauchy-Crofton formula for a polygonal line. By a limiting process, the formula (5.34) can be extended to any regular curve [34].

The formula (5.34) has interesting applications in numerical analysis. Consider a given family of horizontal straight lines, rotate this family by the angles $\pi/4, 2\pi/4, 3\pi/4$ to obtain, for example, four families of straight lines. Consider that the families with inclinations $\pi/4$ and $3\pi/4$ are distanced by r_2 and indicate the number of intersections with them by n_1. The other families have straight lines distanced by r_1, with the number of intersections with them being denoted by n_2. An schematic representation of this configuration is shown in Fig 5.10. We have

$$\frac{1}{2}n_1 r_1 \frac{\pi}{4} + \frac{1}{2}n_2 r_2 \frac{\pi}{4} \simeq \frac{1}{2}\int\int n dp d\xi = \text{length of C.} \tag{5.35}$$

5.2.4 The Korteweg stress tensor and energy flux at the interface

In this subsection, we show that the energy flux $\left\langle (\nabla \cdot P^K) \cdot \mathbf{u} \right\rangle$ due to the Korteweg stress tensor is directly connected with the variation of the total energy of the interface defined as the product between the total length $\mathcal{L}$ of the interface and the surface tension γ.

Using the relation (5.15), we have

$$\begin{aligned}
\left\langle (\nabla \cdot \mathbf{P}^K) \cdot \mathbf{u} \right\rangle &= -\frac{1}{|D|}\int \phi \nabla(\Delta\phi)\cdot \mathbf{u} d\mathbf{x} = \frac{1}{|D|}\int k\nabla\cdot(\nabla\phi)(\nabla\phi\cdot\mathbf{u})d\mathbf{x} \qquad (5.36)\\
&= \frac{1}{|D|}\int k\nabla\cdot(\mathbf{n}|\nabla\phi|)(\nabla\phi\cdot\mathbf{u})d\mathbf{x}\\
&= \frac{1}{|D|}\int k\left((\nabla\cdot\mathbf{n})|\nabla\phi| + \frac{\nabla\phi}{|\nabla\phi|}\cdot\nabla|\nabla\phi|\right)(\nabla\phi\cdot\mathbf{u})d\mathbf{x}\\
&= \frac{1}{|D|}\int k|\nabla\phi|^2(\nabla\cdot\mathbf{n})(\mathbf{n}\cdot\mathbf{u})d\mathbf{x} + \frac{1}{|D|}\int k\left[\mathbf{n}\cdot\nabla\left(\frac{|\nabla\phi|^2}{2}\right)\right](\mathbf{n}\cdot\mathbf{u})d\mathbf{x}\\
&= -\frac{1}{|D|}\int k|\nabla\phi|^2 K(\mathbf{n}\cdot\mathbf{u})d\mathbf{x} + \frac{1}{|D|}\int k\left[\mathbf{n}\cdot\nabla\left(\frac{|\nabla\phi|^2}{2}\right)\right](\mathbf{n}\cdot\mathbf{u})d\mathbf{x},
\end{aligned}$$

where $k = c_s^A G_{AB}/4$ for the Shan-Chen method. Considering the system of normal coordinates given by (5.16), we have

$$\nabla\phi = \mathbf{n}\left(\frac{\partial\phi}{\partial u}\right) + \mathbf{t}\left(\frac{\partial\phi}{\partial s}\right). \qquad (5.37)$$

For small curvatures we can neglect the derivative of ϕ with respect to the arc length [32], which leads to the approximation

$$|\nabla\phi|^2 = \left(\frac{\partial\phi}{\partial u}\right)^2 + \left(\frac{\partial\phi}{\partial s}\right)^2 \approx \left(\frac{\partial\phi}{\partial u}\right)^2. \qquad (5.38)$$

Considering the same hypothesis, we can assume [3]

$$\left[\mathbf{n}\cdot\nabla\left(\frac{|\nabla\phi|^2}{2}\right)\right]\mathbf{n} \simeq \nabla\left(\frac{|\nabla\phi|^2}{2}\right), \qquad (5.39)$$

i.e., the variations of the function $|\nabla\phi|^2/2$ are dominated by the variations in the normal direction of the interface. The approximation (5.39) is better if the interface becomes sharper [65, 96]. Thus, we have

$$\begin{aligned}
\int k\left[\mathbf{n}\cdot\nabla\left(\frac{|\nabla\phi|^2}{2}\right)\right](\mathbf{n}\cdot\mathbf{u})\,d\mathbf{x} &\simeq \int \nabla\left(\frac{|\nabla\phi|^2}{2}\right)\cdot\mathbf{u}d\mathbf{x} \qquad (5.40)\\
&= -\int k\frac{|\nabla\phi|^2}{2}(\nabla\cdot\mathbf{u})d\mathbf{x} = 0,
\end{aligned}$$

considering the incompressibility condition $\nabla \cdot \mathbf{u} = 0$. Therefore

$$\left\langle (\nabla \cdot \mathbf{P}^K) \cdot \mathbf{u} \right\rangle = -\frac{1}{|D|} \int k |\nabla \phi|^2 K (\mathbf{n} \cdot \mathbf{u}) d\mathbf{x} \simeq -\frac{1}{|D|} \int \gamma K (\mathbf{n} \cdot \mathbf{u}) ds, \tag{5.41}$$

where we used the approximation

$$\int k |\nabla \phi|^2 du \simeq \int k \left(\frac{\partial \phi}{\partial u} \right)^2 du \simeq \gamma. \tag{5.42}$$

In the last equality, we used the surface tension relation (4.8).

The normal velocity of the fluid $\mathbf{n} \cdot \mathbf{u}$ in the interfacial region corresponds to the normal velocity of the interface v_N, described by the formula (5.24), which implies in

$$\left\langle (\nabla \cdot \mathbf{P}^K) \cdot \mathbf{u} \right\rangle \simeq -\frac{1}{|D|} \int \gamma K v_N ds, \tag{5.43}$$

and by the formula (5.25), we have

$$\left\langle (\nabla \cdot \mathbf{P}^K) \cdot \mathbf{u} \right\rangle \simeq \frac{1}{|D|} \frac{d(\gamma \mathcal{L})}{dt}. \tag{5.44}$$

This formula implies that the energy flux due to the Korteweg stress tensor (3.109) corresponds directly to the variation of the energy of the interface.

We studied the flux $\left\langle (\nabla \cdot \mathbf{P}^K) \cdot \mathbf{u} \right\rangle$ for miscible and immiscible RT flows in the Figures 5.15(b) and 5.15 (d). In Fig. 5.15(b) is possible to see a significant difference in the energy flows. In Fig. 5.15(d) we verify the relation (5.44) showing that the difference in miscible and immiscible is associated with the appearance of the interface in the immiscible flows. The energy of the interface is calculated by the product between the surface tension γ and the total length of the interface $\mathcal{L}_{tot}$, and the result is shown in Fig. 5.15(c), with the total length calculated by the Cauchy-Crofton formula (5.35). A possible explanation for the difference between the two curves in Fig. 5.15(d) can be attributed to the diffuse interface assumption in the lattice-Boltzmann algorithms and the appearance of high values of curvatures in the late stages of the immiscible Rayleigh-Taylor turbulence.

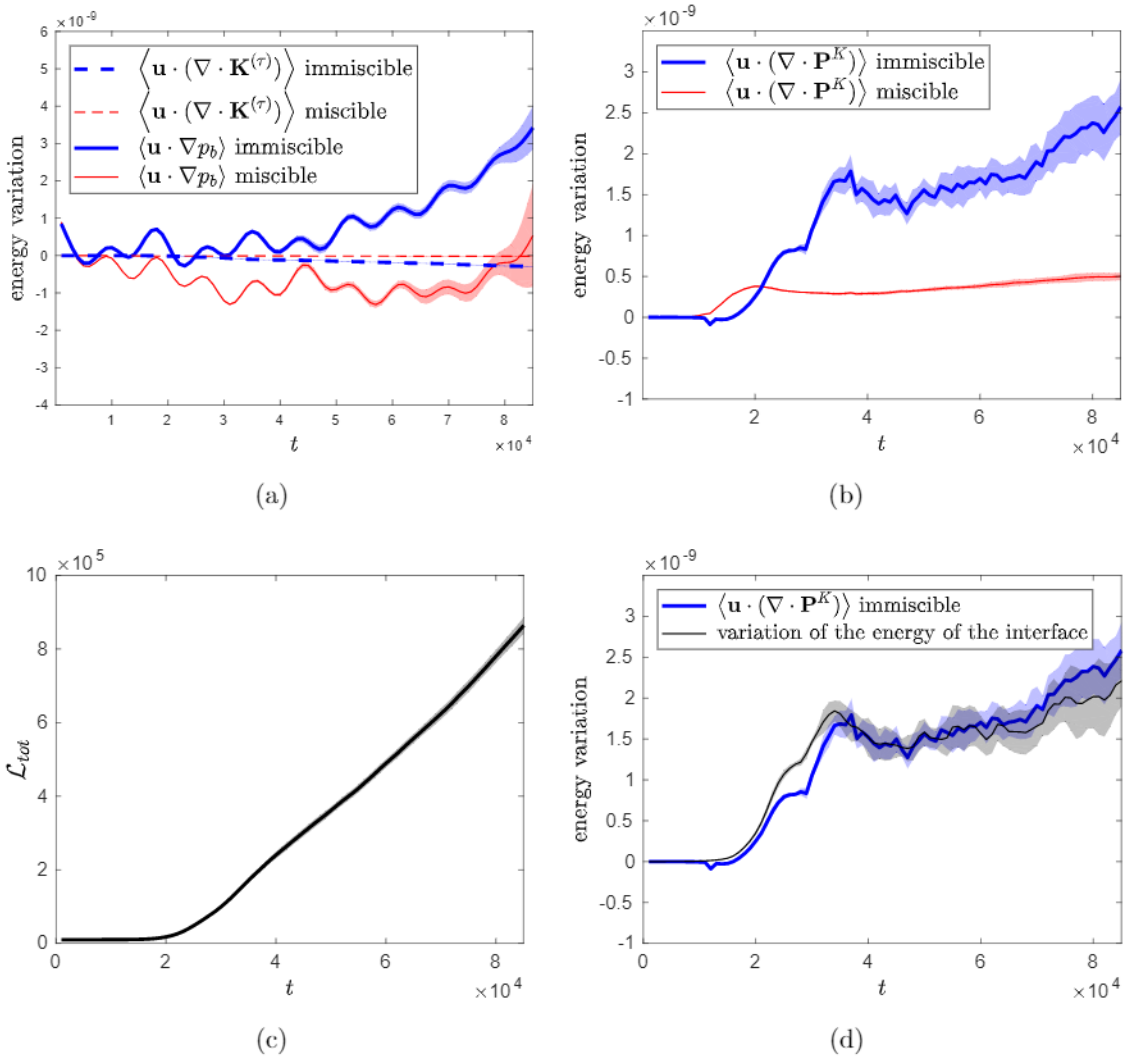

Figure 5.11: (a) Comparison between the energy flux due to the bulk pressure and spurious term. (b) Comparisson between the energy flux due to the Korteweg stresses. (c) Evolution of the total length. (d) Comparisson between the energy flux due to the Korteweg stresses and the right hand side of (5.44) indicated as the variation of the energy of the interface.

5.3 Viscous dissipation and enstrophy

In this subsection, we analyze the flux $\left\langle \mathbf{u} \cdot (\nabla \cdot \left(\eta \nabla \mathbf{u} + \eta \nabla \mathbf{u}^T\right)) \right\rangle$ showing direct connections with the evolution of the enstrophy of the system, defined as

$$\Omega = \frac{1}{2} \int |\boldsymbol{\omega}|^2 d\mathbf{x}, \tag{5.45}$$

where $\boldsymbol{\omega} = \nabla \times \mathbf{u}$ is the vorticity. In the next calculations, we consider the scalar vorticity $\omega = \boldsymbol{\omega} \cdot \mathbf{k}$, where $\mathbf{k}$ is a unit vector perpendicular to the plane of the flow.

Neglecting the density variation, we have

$$\begin{aligned} \left\langle \mathbf{u} \cdot \left(\nabla \cdot \left(\eta \nabla \mathbf{u} + \eta \nabla \mathbf{u}^T\right)\right)\right\rangle &= \eta \left\langle \mathbf{u} \cdot \nabla^2 \mathbf{u} \right\rangle, \qquad (5.46) \\ &= -\eta \left\langle \mathbf{u} \cdot (\nabla \times (\nabla \times \mathbf{u}))\right\rangle \\ &= -\eta \left\langle |\nabla \times \mathbf{u}|^2 \right\rangle + \eta \left\langle \nabla \cdot (\mathbf{u} \times (\nabla \times \mathbf{u}))\right\rangle. \\ &= -\eta \left\langle |\nabla \times \mathbf{u}|^2 \right\rangle \\ &= -\frac{2\eta}{|D|}\Omega, \end{aligned}$$

where we used the following identities [43]

$$\nabla^2 \mathbf{u} = -\nabla \times (\nabla \times \mathbf{u}) + \nabla(\nabla \cdot \mathbf{u}) \qquad (5.47)$$

$$\nabla \cdot (\mathbf{u} \times (\nabla \times \mathbf{u})) = |\nabla \times \mathbf{u}|^2 - \mathbf{u} \cdot (\nabla \times (\nabla \times \mathbf{u})), \qquad (5.48)$$

and the incompressibility condition, $\nabla \cdot \mathbf{u} = 0$. In the integration by parts, we assumed the periodic boundary conditions in the horizontal direction and the no-slip condition in the walls in the vertical directions. A verification of the relation (5.46) is shown in Figures. 5.12(a) and 5.12(b). It is possible to see a significant difference in the evolution of the viscous dissipation between miscible and immiscible flows.

It is apparent from Fig. 5.14(a), that the values of the enstrophy are considerably larger for the immiscible flow. We now argue that this difference can be attributed to the flow in a small neighborhood of the interface. Figure 5.14(b) shows the vorticity field for the immiscible flow; it corresponds to the a small area of 667×467 lattice points marked by the rectangle in the center of Fig. 5.1 and amplified in its right small panel corresponding to $t = 83000$. Visually, it is clear that a considerable part of high vorticity is concentrated near the interface. For comparison, we present the vorticity field for the miscible case in Fig. 5.14(c), which corresponds to a small area from Fig. 5.2. In the miscible case, the vorticity is more dispersed and its amplitude is roughly twice smaller (notice the difference of color scales).

Part of the enstrophy may have a numerical origin coming from spurious currents of the lattice Boltzmann method (see Chapter 4); however, the experiments suggest that this numerical contribution is not large enough to account for all the vorticity generated by the interface.

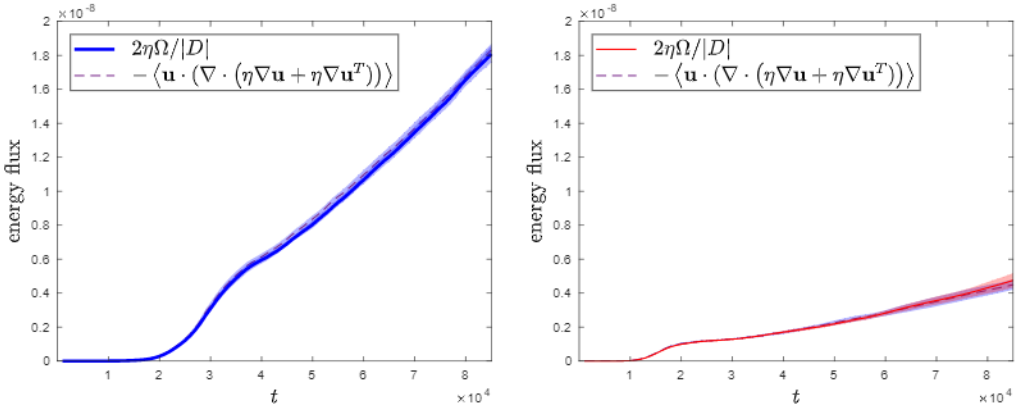

(a) (b)

Figure 5.12: (a) Comparison between the evolution of the enstrophy and dissipation function for immiscible flows. (b) Comparison between the evolution of the enstrophy and dissipation function for miscible flows.

In the following, we analyze some theoretical developments analysing the possible *sources of vorticity* the immiscible RT turbulence.

Applying the curl operator in the momentum equation (5.1), we obtain the following vorticity equation equation [25]

$$\frac{\partial \omega}{\partial t} + (\mathbf{u}\cdot\nabla)\omega = -\frac{k}{\rho_0}(\nabla\times(\Delta\phi\nabla\phi)) + \nu\Delta\omega - \frac{\tilde{g}}{\rho_0}(\nabla\phi\times\mathbf{e}_y). \tag{5.49}$$

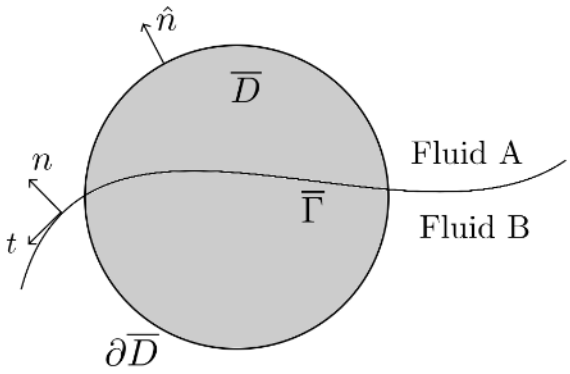

Figure 5.13

Let us consider a control area $\overline{D}\subset D$ which contains part of the interface denoted by $\overline{\Gamma}$, see Fig. 5.13. In this subdomain, the integral form of (5.49) is given by

$$\begin{aligned}\frac{d}{dt}\int_{\overline{D}}\omega d\mathbf{x} &= \oint_{\partial\overline{D}}\nu\nabla\omega\cdot\hat{\mathbf{n}}ds + \oint_{\partial\overline{D}}\hat{\mathbf{n}}\cdot(\mathbf{v}_b-\mathbf{u})ds - \\ &- \int_{\overline{D}}\frac{k}{\rho_0}(\nabla\times(\Delta\phi\nabla\phi))d\mathbf{x} - \int_{\overline{D}}\frac{\tilde{g}}{\rho_0}(\nabla\phi\times\mathbf{e}_y)d\mathbf{x}.\end{aligned} \tag{5.50}$$

where $\mathbf{v}_b$ is the velocity of the boundary $\partial\overline{D}$ of the control volume. The term

$$\int_{\overline{D}} \frac{k}{\rho_0}(\nabla \times (\Delta\phi\nabla\phi))d\mathbf{x}. \tag{5.51}$$

is negligible for miscible flows; see Fig. 5.15, but for immiscible flows this term accounts for part of the vorticity generated at the interface, which also has a contribution of the term

$$\int_{\overline{D}} \frac{\tilde{g}}{\rho_0}(\nabla\phi \times \mathbf{e}_y)d\mathbf{x}, \tag{5.52}$$

as we show in the next calculations.

In the sharp interface formulation (see Appendix A) the vorticity generated by the interface is represented by a source of vorticity σ located at the interface in such a way that

$$\frac{d}{dt}\int_{\overline{D}} \omega dx \;=\; \oint_{\partial\overline{D}} \nu\nabla\omega\cdot\hat{\mathbf{n}}ds + \oint_{\partial\overline{D}} \hat{\mathbf{n}}\cdot(\mathbf{v}_b - \mathbf{u})ds + \int_{\overline{\Gamma}} \sigma ds \tag{5.53}$$

For no-slip viscous fluid–fluid interfaces [54], an explicit expression for σ is given by [93]

$$\sigma = -\frac{\partial}{\partial s}\left[\left[\frac{p}{\rho}\right]\right] - \frac{\partial}{\partial s}[[\Phi_g]] \tag{5.54}$$

with p and $\mathbf{u}$ satisfying the equations (2.5) and (2.4), and Φ_g is a potential function for the body forces. As in [20] we use symbol $[[\beta]] = \beta_A - \beta_B$ to indicate the jump across the interface of the value of some function β, where β_s indicates the values of the function β in the component s. In formula (5.54), the viscosity does not appear in the vorticity generation terms, and *circulation may only be generated on the interface by pressure jumps and body forces.* Still, according to [93], the viscous forces produce a flux of vorticity into the fluid interior, so that all circulation generated by the inviscid mechanism appears as a boundary flux on the interface.

For viscous interfaces, the continuity of the normal stress across the interface implies in the following [93]

$$[[p]] = -2\left[\left[\eta\left(\frac{\partial(\mathbf{u}\cdot\mathbf{t})}{\partial s} + K(\mathbf{u}\cdot\mathbf{n})\right)\right]\right] - \gamma K, \tag{5.55}$$

considering the no-slip condition at the interface, the jump in pressure becomes

$$[[p]] = -2[[\eta]]\left(\frac{\partial v_T}{\partial s} + K v_N\right) - \gamma K, \tag{5.56}$$

where v_T and v_N are tangential and normal velocities of the interface, see (5.24). In the Boussinesq approximation for the Rayleigh-Taylor systems, we have

$$\frac{\partial}{\partial s}\left[\left[\frac{p}{\rho}\right]\right] \simeq \frac{1}{\rho_0}\frac{\partial [[p]]}{\partial s} = -2\frac{[[\eta]]}{\rho_0}\left(\frac{\partial^2 v_T}{\partial s^2} + \frac{\partial (K v_N)}{\partial s}\right) - \frac{1}{\rho_0}\frac{\partial}{\partial s}(\gamma K) \tag{5.57}$$

and

$$[[\eta]] = 0, \qquad [[\Phi_g]] = -2\rho_0 y\tilde{g}, \tag{5.58}$$

where in the last relation we used (2.6). Thus,

$$\sigma \simeq \frac{1}{\rho_0}\frac{\partial}{\partial s}(\gamma K) + \frac{1}{\rho_0}\frac{\partial}{\partial s}(2y\rho_0\tilde{g}). \tag{5.59}$$

In the following, we show that

$$\int_{\overline{D}} \frac{k}{\rho_0}(\nabla \times (\Delta\phi\nabla\phi))d\mathbf{x} \quad \xrightarrow{\delta\to 0} \quad -\frac{1}{\rho_0}\int_{\overline{\Gamma}} \frac{\partial(\gamma K)}{\partial s} ds \tag{5.60}$$

and

$$\int_{\overline{D}} \frac{\tilde{g}}{\rho_0}(\nabla\phi \times \mathbf{e}_y)d\mathbf{x} \quad \xrightarrow{\delta\to 0} \quad -\frac{1}{\rho_0}\int_{\overline{\Gamma}} \frac{\partial(2\rho_0 y\tilde{g})}{\partial s} ds, \tag{5.61}$$

where $\delta \to 0$ indicates the sharp interface limit (see Appendix A). Consider the following

$$\begin{aligned}
\frac{1}{\rho_0}\int_{\overline{D}} (\nabla \times (k\Delta\phi\nabla\phi))d\mathbf{x} &= \frac{1}{\rho_0}\int \nabla \times (k\nabla\phi\nabla\cdot(\nabla\phi))d\mathbf{x} \\
&= \frac{1}{\rho_0}\int \nabla \times \left(k\frac{\nabla\phi}{|\nabla\phi|}|\nabla\phi|\nabla\cdot\left(\frac{\nabla\phi}{|\nabla\phi|}|\nabla\phi|\right)\right)d\mathbf{x} \\
&= \frac{1}{\rho_0}\int \nabla \times (k\mathbf{n}|\nabla\phi|\nabla\cdot(\mathbf{n}|\nabla\phi|))\,d\mathbf{x} \\
&\simeq \frac{1}{\rho_0}\int \nabla \times \left(-k|\nabla\phi|^2 K\mathbf{n} + k\nabla\left(\frac{|\nabla\phi|^2}{2}\right)\right)d\mathbf{x} \\
&\simeq -\frac{1}{\rho_0}\int \nabla \times \left(k|\nabla\phi|^2 K\mathbf{n}\right)d\mathbf{x} \\
&\simeq -\frac{1}{\rho_0}\int (\nabla(k|\nabla\phi|^2 K)\times\mathbf{n})d\mathbf{x} - \frac{1}{\rho_0}\int k|\nabla\phi|^2 K(\nabla\times\mathbf{n})d\mathbf{x}.
\end{aligned} \tag{5.62}$$

Now, define the auxiliary function $\overline{\phi} = \phi/|\nabla\phi|$, we have

$$\nabla\overline{\phi} = \frac{\nabla\phi}{|\nabla\phi|} - \frac{\phi\nabla\phi\cdot\nabla^2\phi}{|\nabla\phi|^3} = \frac{\nabla\phi}{|\nabla\phi|} \tag{5.63}$$

where we considered $\phi = 0$ at the interface. Thus,

$$\nabla\times\mathbf{n} = \nabla\times\left(\frac{\nabla\phi}{|\nabla\phi|}\right) = \nabla\times(\nabla\overline{\phi}) = 0. \tag{5.64}$$

Consequently,

$$\begin{aligned}
\frac{1}{\rho_0}\int_{\overline{D}}(\nabla\times(k\Delta\phi\nabla\phi))d\mathbf{x} &\simeq -\frac{1}{\rho_0}\int(\nabla(k|\nabla\phi|^2K)\times\mathbf{n})d\mathbf{x} \\
&\simeq -\frac{1}{\rho_0}\int(\nabla(k|\nabla\phi|^2K)\cdot\mathbf{t})d\mathbf{x} \\
&\simeq -\frac{1}{\rho_0}\int\int\frac{\partial(k|\nabla\phi|^2K)}{\partial s}dsdu \\
&\simeq -\frac{1}{\rho_0}\int\frac{\partial(\gamma K)}{\partial s}ds
\end{aligned} \tag{5.65}$$

verifying (5.60). Note that we used again the approximation (5.42) and normal system of coordinates defined by (5.16).

Now, consider the following

$$\begin{aligned}
\int_{\overline{D}}\tilde{g}(\nabla\phi\times\mathbf{e}_y)d\mathbf{x} &= \int\tilde{g}\nabla\phi\cdot\mathbf{e}_x d\mathbf{x} \\
&= \int\tilde{g}|\nabla\phi|\mathbf{n}\cdot\mathbf{e}_x d\mathbf{x} \\
&= -\int\int\tilde{g}|\nabla\phi|\mathbf{t}\cdot\mathbf{e}_y dsdu,
\end{aligned} \tag{5.66}$$

where we used $\mathbf{n}\cdot\mathbf{e}_x = -\mathbf{t}\cdot\mathbf{e}_y$. It is possible to show that [18]

$$\int|\nabla\phi|du \simeq 2\rho_0, \tag{5.67}$$

since we have ϕ varying between ρ_0 and $-\rho_0$ in the definition of the order parameter for the solutions given by Shan-Chen method. Consequently, from (5.66), we have

$$\begin{aligned}
\int_{\overline{D}}\tilde{g}(\nabla\phi\times\mathbf{e}_y)d\mathbf{x} &\simeq -\int 2\rho_0\tilde{g}\mathbf{t}\cdot\mathbf{e}_y ds \\
&\simeq -\int 2\rho_0\tilde{g}\frac{\partial\mathbf{R}(s)}{\partial s}\cdot\mathbf{e}_y ds \\
&\simeq -\int 2\rho_0\tilde{g}\frac{\partial(\mathbf{R}(s)\cdot\mathbf{e}_y)}{\partial s}ds \\
&\simeq -\int 2\rho_0\tilde{g}\frac{\partial y(s)}{\partial s}ds \\
&\simeq -\int\frac{(2\rho_0\tilde{g}y)}{\partial s}ds,
\end{aligned} \tag{5.68}$$

demonstrating (5.61), where $y(s)$ is the vertical coordinate of the interface position $\mathbf{R}(s)$; see Fig. 5.9.

For quantification of the interface contribution, we separate the bulk enstrophy in the immiscible case by excluding small areas around the interface. This is done

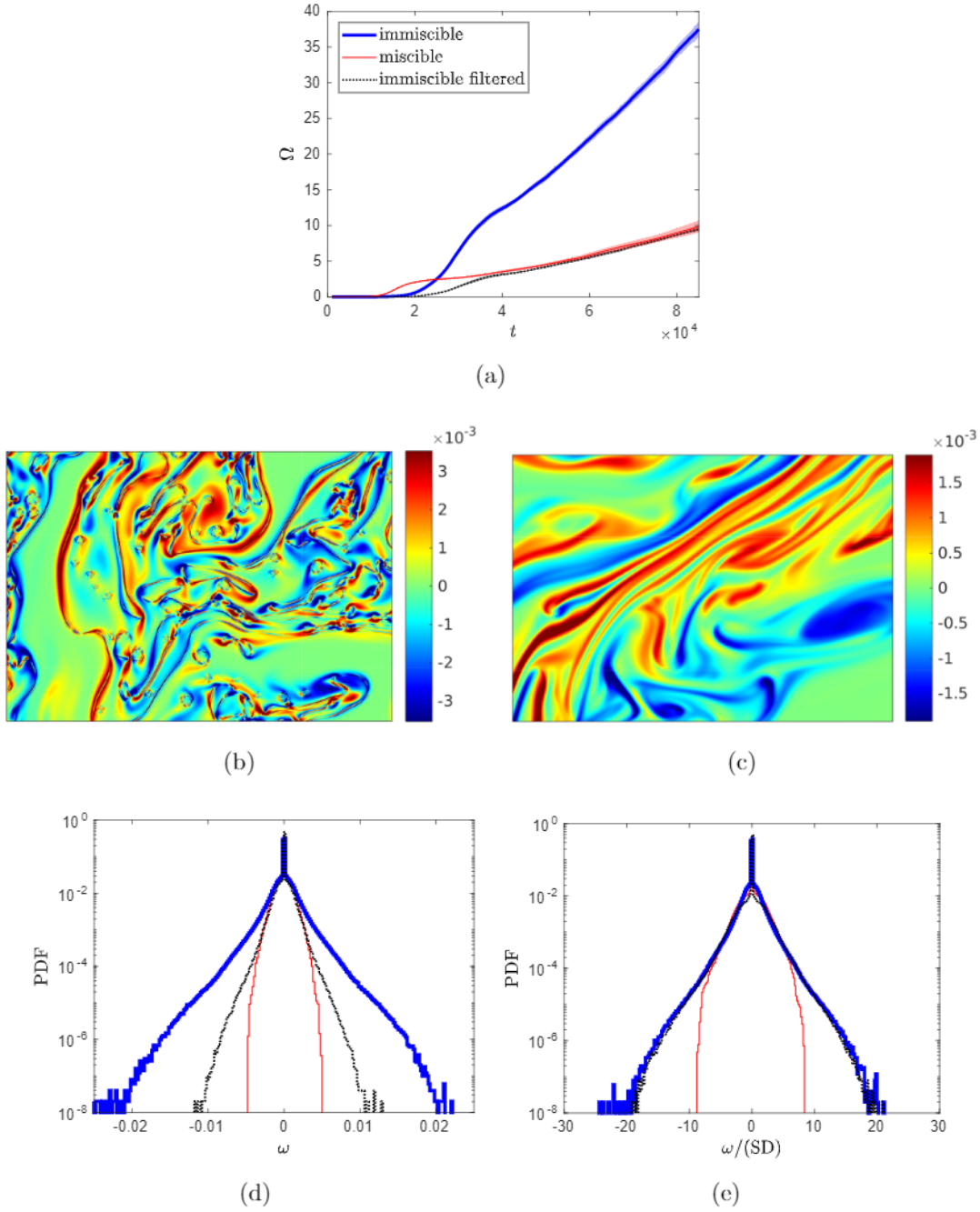

Figure 5.14: (a) Evolution of total enstrophy averaged over 10 realizations for the immiscible (bold blue) and miscible (thin red) simulations; shaded regions indicate standard deviations. The dashed black line corresponds to the filtered enstrophy of the immiscible flow, by excluding small neighborhoods of the interface. (b) Example of vorticity field for immiscible and (c) miscible flow. (d) PDFs of the vorticity fields. (e) PDFs of the vorticity fields normalized by the respective standard deviations (SD).

numerically by removing all nodes within squares of size 8×8 at each point of the interface (see Chapter 3). This size is much smaller than the typical drop for the late turbulent times ($\ell \sim 50$) and roughly twice larger than the expected viscous scale η (in Chapter 6 we estimate $\eta \sim 4$) and the numerical interface width ($l_{int} \sim 3$).

The filtered enstrophy is plotted in Fig. 5.14(a) by the dotted black curve, which agrees very well with the miscible data for the times corresponding to turbulent mixing. Though such a fine agreement may partially be attributed to the chosen filter, removing larger areas around the interface yields only a moderate effect, as shown in Chapter 4. This observation suggests that the immiscible flow in the regions away from the interface features turbulent statistics similar to the miscible flow. This conclusion is also justified in Fig. 5.14(d), where we plot PDFs of vorticity: one can see that the PDFs for the miscible (red) and filtered immiscible (dotted black) flows are very close, while the PDF for the full immiscible flow favors much larger values of vorticity characteristic of thin boundary layers. Still, normalized PDFs of vorticity shown in Fig. 5.14(c) reveal a distinctive shape of the tails for large ω (rare events), which is the same for the original and filtered fields in the immiscible flow.

5.4 First topology changes and critical velocities

The graphs in Fig. (d) mark a transition to a new regime starting at times close to $t = 30.000$, at which the variation of interface energy attains a local maximum. We argue that this transition indicates the moment when the interface becomes disconnected generating small drops and large disconnected clusters. This behavior is clearly seen in Fig. 5.15, where we plot the density profiles at four different times. These figures show the process of how the interface becomes disconnected after $t = 30.000$. A similar phenomenon was observed in [6] for the one-dimensional convective Cahn-Hilliard equation, where, for some particular examples of velocity fields, it has been shown the existence of critical velocities such that steady states in a form of droplets exist for velocity values smaller than a given critical velocity. When the velocity is slowly increased past the critical values, the droplet splits in the middle and break up into two droplets and no such steady state exists for the system.

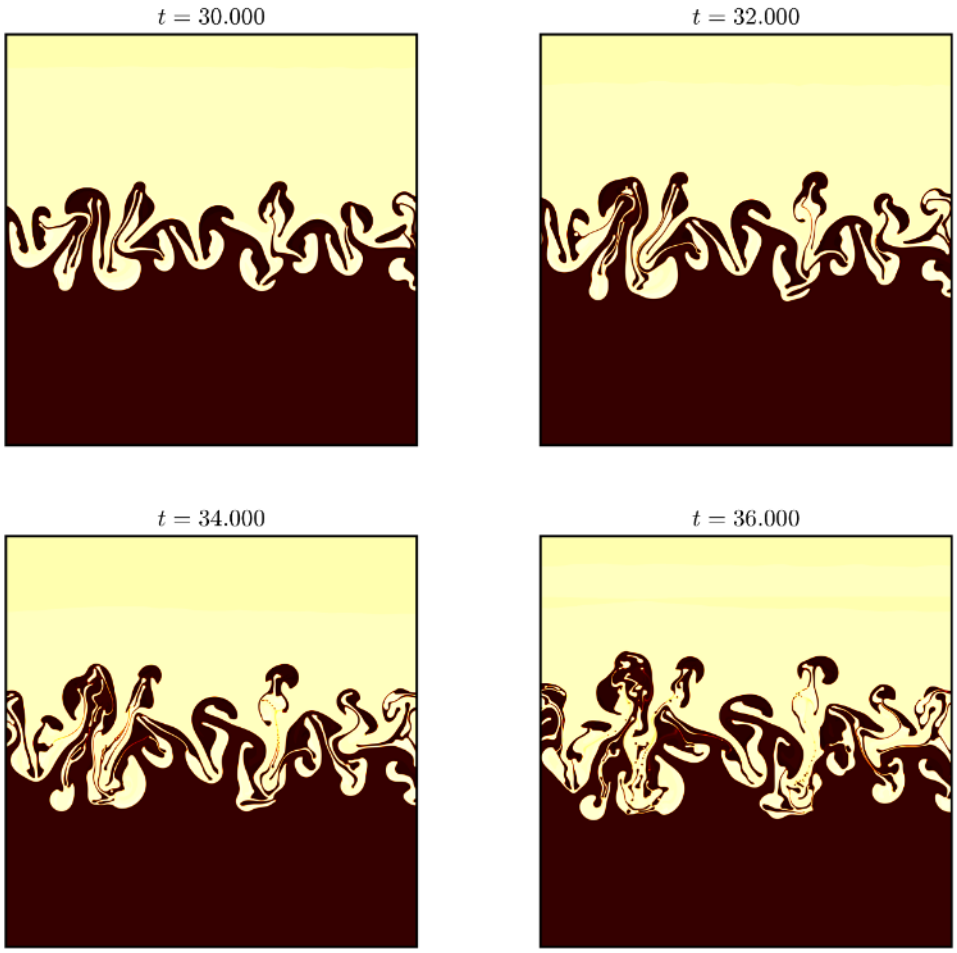

Figure 5.15: Evolution of the interface profile for times close to the local maximum for the total interface energy; see also Fig. (d). For time $t = 30.000$ the interface has only one component, while in the next few times the first topology changes take place leading to the first drops and large disconnected clusters.

5.5 Concluding remarks

In this chapter, we provided a study of the energy budget of the Rayleig-Taylor systems in the linear, non-linear and turbulent regimes. We focused in the immiscible case, where according to (5.46) and (5.25), we expected to obtain

$$\partial_t(E_k + E_p) = -\frac{1}{|D|}\frac{d(\gamma \mathcal{L}_{tot})}{dt} - \frac{2\eta}{|D|}\Omega \tag{5.69}$$

The dissipation in the total energy budget for the miscible case corresponds only to the generation of the enstrophy of the system.

With respect to the numerical investigation, we can highlight the following results:

- The potential energy statistics are similar between miscible and immiscible.

- Kinetic energy statistics show significant differences between miscible and immiscible flows. Analyzing the components of the kinetic energy variations, we found that the differences are connected to the energy flux due to the stress tensor $\left\langle \mathbf{u} \cdot (\nabla \cdot \mathbf{P}^{(TOT)}) \right\rangle$ and the viscous dissipation $\left\langle \mathbf{u} \cdot \nabla(\eta \nabla \mathbf{u} + \eta(\nabla \mathbf{u})^T) \right\rangle$.

- The verification of the balance (5.11) and the fact that the spurious contribution $\left\langle \mathbf{u} \cdot (\nabla \cdot \mathbf{K}^{(\tau)}) \right\rangle$ is negligible, show that the solutions provided by the Shan-Chen multicomponent method solve accurately the equations for the proposed RT systems.

- We verify the expected connection between the flux due to the Korteweg stress tensor $\mathbf{P}^k$ and the variation of the total length of the interface, calculated numerically by the Cauchy-Crofton formula.

- We show indications that the interface acts as a source of vorticity, which can explain part of the difference in the viscous dissipation statistics verified between miscible and immiscible flows.

- Analyzing the variation of the total energy of the interface, we verify the existence of a critical time in the transition to turbulence. The analyses of the density profiles close to this critical point show that the fast variation is associated to the first topology changes that leads to the appearance of the first drops and large disconnected clusters.

Chapter 6

Immiscible vs miscible Rayleigh-Taylor turbulence: testing phenomenologies with lattice Boltzmann simulations

6.1 The 1941 Kolmogorov's theory (K41)

In this section, following [38, 74, 33, 53], we briefly discuss a phenomenological theory for the turbulent motion of homogeneous (translational invariance), isotropic (rotationally invariant) and stationary turbulence of free shear flows.

In this type of flow, the turbulent motion range in size from the characteristic length of the flow to much smaller scales. In the paper [53], Kolmogorov proposed a scenario where the flow is assumed to be homogeneous and isotropic and is left alone to slowly dampen out by viscosity, configuring the so-called decaying turbulence. In this section, we consider a flow maintained by a force active on large scales of the flow and is kept in a state of statistical equilibrium in the sense that on average of the kinetic energy injected by the external force is balanced by the energy dissipated by viscosity [33].

The central ideas in the Kolmogorov's theory of turbulence are the energy cascades and the Kolmogorov hypothesis. The energy cascades correspond to the idea

that the energy is injected in the turbulent motion flow at the largest scale L of the motion (associated to the typical size of the mechanism responsible for generating the turbulent flow [38]) and transferred to smaller and smaller scales of motion without dissipation, at a constant rate ε, until be dissipated in some small scale η by viscous action [74]. In this picture, there is a range of scales r such $\eta \ll r \ll L$ and such that the energy is not injected either dissipated, such range is called the *inertial range*. For every scale $r \ll L$, it is possible to associate a typical velocity $\delta_r u$ defined as

$$\delta_r u \sim \sqrt{\left\langle \left| (\mathbf{u}(\mathbf{x}+\mathbf{r}) - \mathbf{u}(\mathbf{x})) \cdot \frac{\mathbf{r}}{r} \right|^2 \right\rangle} \tag{6.1}$$

where the symbol ' $\sim$ ' means proportionality [33], $\mathbf{r}$ is any vector with length $|\mathbf{r}| = r$ (since we consider an isotropic flow) and $\langle \cdot \rangle$ denotes the ensemble average (or time average considering the ergodic hypothesis). The respective typical time scale τ_r (or eddy turn over time) is defined as

$$\tau_r \sim \frac{r}{\delta_r u}. \tag{6.2}$$

Some natural questions are related to the what is typical size of the smallest eddies responsible for the dissipation of the energy, and how $\delta_r u$ and τ_r changes if r decreases. These questions were partially answered by the theory of Kolmogorov, which can be stated, according to [38], in the form of three hypothesis:

> **(H1)** In the limit of infinite Reynolds number, all possible symmetries of the Navier-Stokes equation, usually broken by the mechanism producing the turbulent flow, are restored in a statistical sense at small scales and away from any boundaries.
>
> **(H2)** Under the same assumptions as in (H1), the turbulent flow is self-similar.
>
> **(H3)** Under the same assumptions as in (H1), the turbulence has a finite non vanishing mean rate of dissipation ε per unit of mass.

By small scales we mean scales such that $r \ll L$. The hypothesis (H2) implies that the typical velocities are related by $\delta_{r_1} u = f(r_2/r_1)\delta_{r_2} u$, where f is some universal

function [33] to be obtained later in this section. For (H3), in the limit of infinite Reynolds number, we must keep the integral scale L and the typical velocity U constant, and let $\nu \to 0$.

Considering the characteristic quantities defined previously and the Kolmogorov's hypothesis, we now approach the phenomenology of turbulence in the sense of Kolmogorov. By phenomenology we mean a kind of shorthand system whereby the same results can be recovered in a much simpler way, and naturally, at the price of less rigorous arguments [38]. The phenomenology of the fully developed turbulence is generally associated to some mental visualization, like the idea of the Richardson cascade, which considers that the turbulent flow is composed of eddies of different sizes. The eddies of size r have a characteristic velocity $\delta_r u$ and timescale τ_r. By 'eddy' it is understood a turbulent motion, localized within a region of size r, that is at least moderately coherent over this region [74]. The eddies in the largest size range are characterized by the lengthscale r, which is comparable to the flow scale L and their characteristic velocity U. The Reynolds number in the biggest eddies (given by $Re = UL/\nu$) is large, with the direct effects of the viscosity being negligible. In the Richardson notion, the biggest eddies are unstable and break up into smaller eddies. Those eddies undergo to a similar break up process, transferring their energies to yet smaller eddies. This process continues until a Reynolds number small enough to make the eddies stable, and the viscosity is effective in the dissipation of the energy [74, 38].

The time scale τ_r is also a typical time for the energy transfer between scales in the inertial range. Thus, the energy flux, denoted by Π_r, can be estimated by

$$\Pi_r \sim \frac{(\delta_r u)^2}{\tau_r} \sim \frac{(\delta_r u)^3}{r}. \tag{6.3}$$

In the inertial range, there is no injection and no dissipation of energy, which implies that the energy flux should be independent of the scale r and equal to the mean energy dissipation rate ε, which leads to

$$\frac{(\delta_r u)^3}{r} \sim \varepsilon, \quad \text{for} \quad \eta \ll r \ll L. \tag{6.4}$$

Thus

$$\delta_r u \sim \varepsilon^{1/3} r^{1/3}, \tag{6.5}$$

in the inertial range. The respective time scale is given by

$$\tau_r \sim \varepsilon^{1/3} r^{2/3}. \tag{6.6}$$

At the top of the inertial range, we have

$$U \sim \varepsilon^{1/3} L^{1/3}. \tag{6.7}$$

The bottom of the inertial range, where the viscous effect becomes significant, can be estimated as follows. The typical time for viscous diffusion to attenuate the energy flux on the scale $\sim r$ is given by [74]

$$t_r^{diff} \sim \frac{r^2}{\nu}, \tag{6.8}$$

and the match between (6.6) and (6.8) happens at a scale η given by

$$\eta \sim \left(\frac{\nu^3}{\varepsilon}\right)^{1/4}, \tag{6.9}$$

which is the so-called Kolmogorov scale.

Naturally, more phenomenological predictions can be computed; see [38]. The results obtained by the phenomenology are compatible with well established results in 3D turbulence, like the two-thirds and four-fifths laws. In some experimental results [33], deviations from the phenomenological predictions were found, characterizing, for example, the phenomenon of intermittency [38, 74].

For a flow constrained in two dimensions, the scenario is significantly different from what is observed in 3D turbulence. In two dimensions, the vorticity acts as a passive advected quantity and the enstrophy is an inviscid invariant of the flow, like the energy. For an unforced flow with high Reynolds number, the enstrophy must grow in order to dissipate the energy at small scales, which is impossible, since the enstrophy can only decrease from its initial value due to dissipation. It implies that a cascade of energy for small scales (direct cascade) does not happens in the 2D turbulence [33], and what actually happens is an inverse cascade of energy, i.e., kinetic energy flowing to the biggest scales. The scale relationships of Kolmogorov's phenomenological theory are also expected in two dimensions, since the scale arguments used do not assume a specific direction of the energy cascade.

In the next sections, we study a two-dimensional extension of the Komolgorov's phenomenology for the context of complex fluids. Specifically, we approach a phenomenological theory for the Rayleigh-Taylor turbulence described in Chapter 2. The predictions then are tested using numerical results obtained by using the Shan-Chen multicomponent method shown in Chapter 3.

6.2 Rayleigh-Taylor turbulence and numerics

6.2.1 Evolution and shape of the mixing layer

In this subsection, we investigate the large-scale dynamics of the RT mixing layer, comparing its development in immiscible and miscible flows. We consider ensembles with at least 15 simulations for the immiscible and miscible flows performed for different random initial disturbances, as described in Chapter 3. Recall that the choice of the size of the ensembles is motivated by small values of standard deviations verified in our numerical experiments, indicating a small dependence on the initial conditions.

Development of the mixing layer from a small initial perturbation of the straight interface line are presented in Fig. 5.1 (immiscible) and Fig. 5.2 (miscible). The panels in the bottom of these figures correspond to zooms of a small region in the middle of the computational domain (red rectangles in the main plots) at different times. They illustrate the initial linear growth of perturbations, which develop to nonlinear quasi-periodic pattern with mushroom-like structures. For later times, these structures break down, forming a fully developed turbulent mixing layer.

Macroscopic properties of the turbulent mixing layer are described by its width $L(t)$ and the large-scale velocity fluctuation $U(t)$. To estimate the evolution of mixing layer $L(t)$, we consider a simplified version of the Boussinesq approximation showed in Chapter 2. In this simplification, the energy relations are obtained by analyzing the movement of plumes with fixed base B (for simplicity) and height given by the $L(t)$ [13]. The variation of the potential energy of the plumes, with densities ρ_1 and ρ_2, is approximated by

$$\Delta P = (\rho_1 - \rho_2) L^2 B g, \tag{6.10}$$

and the kinetic energy change by

$$\Delta E = (\rho_1 + \rho_2) LB \frac{dL}{dt}^2 , \tag{6.11}$$

where g is the gravity acceleration. Using Euler-Lagrange equation for the Lagrangian $\mathcal{L} = E - 2\alpha_L P$, we obtain

$$\frac{d^2 L}{dt^2} L + \frac{1}{2} \frac{dL}{dt}^2 = 4\alpha_L \mathcal{A} g L, \tag{6.12}$$

where the dimensionless parameter α_L characterize the efficiency of the conversion of potential energy into kinetic energy [15]. The solution of the equation (6.12), for a initial condition $L(0) = L_0$ associated with the first times of the appearance of self-similar profiles, is given by

$$L(t) = L_0 + 2(\alpha_L \mathcal{A} g L_0)^{1/2} t + \alpha_L \mathcal{A} g t^2 \tag{6.13}$$

Extending this analysis from a single plume to the whole interface, it is possible to show the growth of the mixing layer for late times follows asymptotically the law [13]

$$L((t) \sim \alpha_L \tilde{g} t^2. \tag{6.14}$$

Recall that the Atwood number $\mathcal{A}$ characterizes typical density variations, and we denoted $\tilde{g} = \mathcal{A} g$ in the Boussinesq approximation and the lattice Boltzmann method.

The Figure 5.8 from Chapter 5 shows that the energy flows at the large scales due to the viscous term $\nabla \cdot (\eta \nabla \mathbf{u} + \eta (\nabla \mathbf{u})^T))$ and momentum flux tensor $-\nabla \cdot \mathbf{P}^{(TOT)}$ are negligible in comparison to the flux of the buoyancy term $-\phi \tilde{g} \mathbf{e}_y$, for miscible and immiscible flows. It implies in following phenomenological relation for the large scales energy balance

$$\frac{dE}{dt} \sim -\frac{dP}{dt}, \tag{6.15}$$

which describes the transfer of potential energy $P \propto -\mathcal{A} g L$ into kinetic energy $E \propto U^2$. This energy balance provides the relation

$$\frac{dU}{dt} \sim \mathcal{A} g \tag{6.16}$$

which gives

$$U(t) \approx \alpha_U \mathcal{A} g t, \tag{6.17}$$

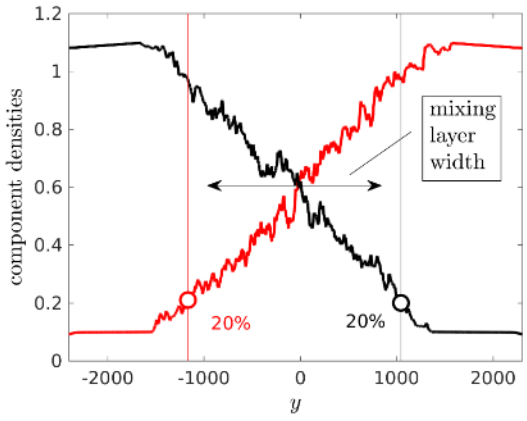

Figure 6.1: Definition of the mixing layer as the region between two points, where the averaged component densities ρ_A (red) and ρ_B (black) attain 20% of the total density.

where the dimensionless parameter α_U is also related to the efficiency of the conversion of potential into kinetic energy.

The numerical procedure for the analysis of mixing layer is illustrated in Fig. 6.1. Here the red and black lines show the dependence on the vertical coordinate y for the component densities $\rho_A(\mathbf{x}, t)$ and $\rho_B(\mathbf{x}, t)$ averaged with respect to the horizontal coordinate x. We define the mixing layer as the region between two points, at which the averaged density of each component reaches 20% of the total density. This definition separates the central region of the mixing layer, cutting off its most non-homogeneous outer parts. Then, the large-scale velocity fluctuation is introduced as

$$U^2 = \langle \|\mathbf{u}\|^2 \rangle_{\mathrm{ML}}, \tag{6.18}$$

where the averaging is performed within the central region of the mixing layer.

Numerical measurements for the width $L(t)$ and speed $U(t)$ of the mixing layer, averaged with respect to ensembles of realizations, are presented in Fig. 6.2 for both immiscible and miscible flows. We associate the beginning of turbulent mixing with the time when mushroom-like structures break down into a chaotic multi-scale mixing layer; see Figs. 5.1 and 5.2. In our simulations, turbulent mixing layers develop roughly at the times $t \gtrsim 4 \times 10^4$ in the immiscible case and $t \gtrsim 3 \times 10^4$ in the miscible case. The difference between these initial times can be attributed to the resistance caused by the surface tension in immiscible flows. All simulations are stopped at times $t \approx 8.5 \times 10^4$. For larger times, the mixing layer may be affected considerably by the top and bottom

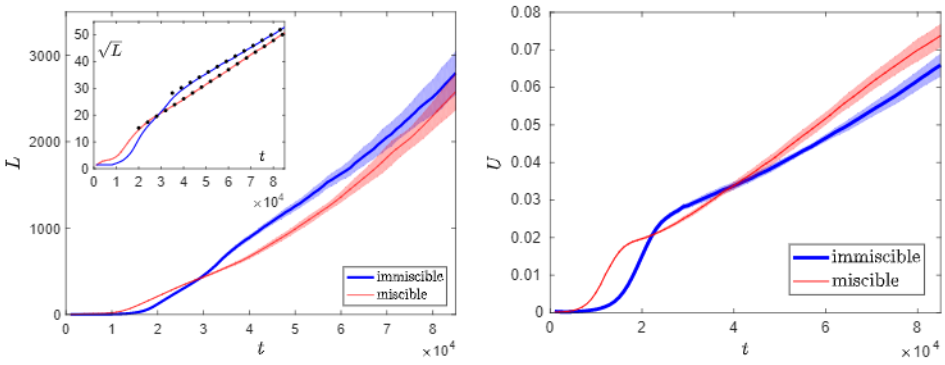

(a) (b)

Figure 6.2: (a) Width of the mixing layer $L(t)$ and (b) large-scale velocity fluctuation $U(t)$ depending on time for immiscible (bold blue) and miscible (thin red) flows. Shaded areas indicate standard deviations. The inset in figure (a) compares the graphs $\sqrt{L(t)}$ in the region of turbulent mixing with the estimated slopes (6.20) shown by dotted lines.

rigid boundaries. In terms of the Reynolds number, defined as

$$\mathrm{Re} = UL/\nu, \tag{6.19}$$

the developed turbulent regime corresponds to $(0.3 \sim 2.1) \times 10^4$ for the immiscible flow and $(0.1 \sim 2.1) \times 10^4$ for the miscible flow.

In order to verify the phenomenological predictions (6.14) and (6.17), we estimate

$$\alpha_L = \frac{1}{4\mathcal{A}gL}\left(\frac{dL}{dt}\right)^2, \quad \alpha_U = \frac{1}{\mathcal{A}g}\frac{dU}{dt}, \tag{6.20}$$

where the derivatives are computed by centered finite differences of second order. Such relations are more robust numerically because they are insensitive to shifts of the initial time, $t \mapsto t - t_*$, accounting for the early non-turbulent development of the mixing layer. Results of computations with formulas (6.20) are shown in Fig. 6.3 demonstrating clear tendencies to constant values in the regions of developed turbulent mixing. The estimated values are $\alpha_L = 0.027 \pm 0.005$ and $\alpha_U = 0.083 \pm 0.007$ for immiscible and $\alpha_L = 0.033 \pm 0.004$ and $\alpha_U = 0.1 \pm 0.005$ for miscible flows; see also the direct comparison in the inset of Fig. 6.2(a). Notice that previous experiments [30, 81, 26, 13] reported the pre-factors α_L between 0.01 and 0.06 for the miscible mixing layer, which are compatible with our estimates taking into account that we use a

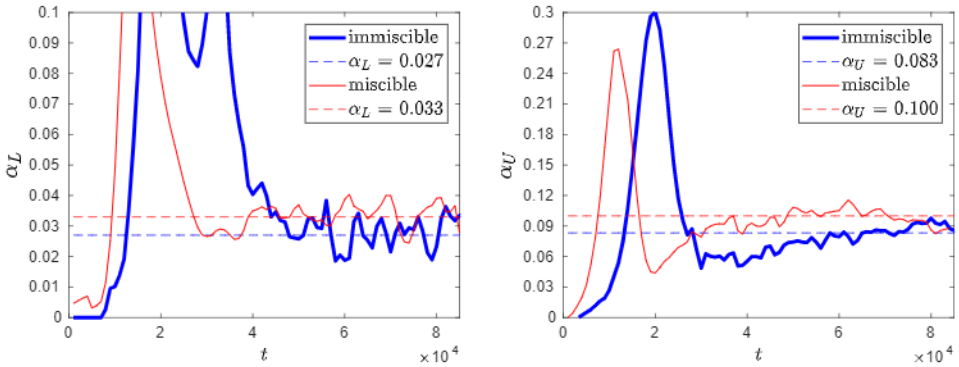

(a) (b)

Figure 6.3: Measurement of the dimensionless pre-factors for the immiscible (bold blue) and miscible (thin red) flows: (a) α_L for the mixing layer width and (b) α_U for the large-scale velocity fluctuation. Constant values (dashed lines) are estimated in the regions of turbulent mixing.

different definition of L. Our results provide a value of α_L in the immiscible case slightly lower than those in the miscible situation, see Fig. 6.3(a), indicating that the immiscible RT turbulence may be less efficient in the conversion of potential into kinetic energy; the same conclusions are valid for the other pre-factor α_U. However, the differences are small (comparable to standard deviations), which does not exclude the possibility that they are actually equal for immiscible and miscible flows in the asymptotic limit of infinitely large domain. Analogous universality of the mixing layer pre-factors with respect to small-scale physics was observed recently for the Kelvin–Helmholtz instability [94], where Navier–Stokes flows were compared to a point-vortex model.

A different model for the typical large-scale velocity is proposed by [13], which here we call $\overline{U}$, considering only the vertical component of the velocity field, i.e.,

$$\overline{U}^2 = \langle \|\mathbf{u} \cdot \mathbf{e}_y\|^2 \rangle_{\mathrm{ML}} \tag{6.21}$$

where $\mathbf{e}_y$ is the unit vector in the normal direction. The result is shown in Fig. 6.4. For this experiment, the values of α_U are slightly smaller than the values shonw in Fig. (6.3)(b), but it is still possible to observe the horizontal shape of the curve of the curve for $\alpha_{\overline{U}}$ for late times, indicating the linear growth of the respective typical velocity. The estimated values are $\alpha_U = 0.068 \pm 0.007$ for immiscible and $\alpha_U = 0.08 \pm 0.005$ for

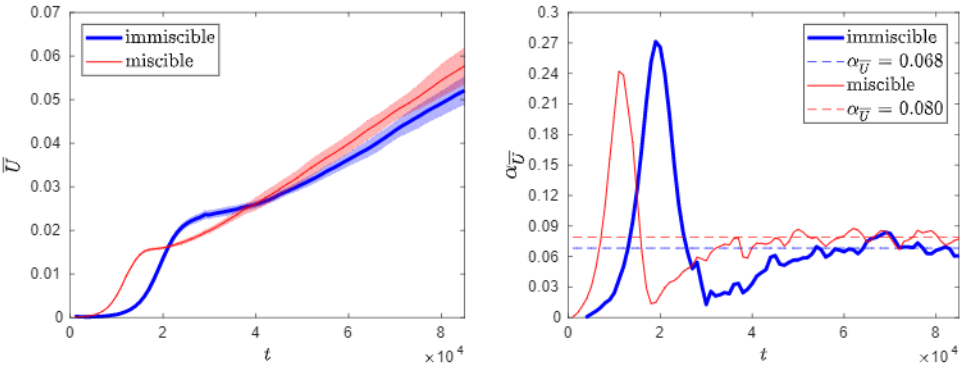

(a) (b)

Figure 6.4: (a) Large-scale velocity fluctuation $\overline{U}(t)$ depending on time for immiscible (bold blue) and miscible (thin red) flows. (b) $\alpha_{\overline{U}}$ for the large-scale velocity fluctuation. Constant values (dashed lines) are estimated in the regions of turbulent mixing.

miscible flows.

The Figure 6.5 shows profiles for the density ρ_A of component A averaged with respect to the horizontal coordinate x and ensemble of realizations. The figure (a) shows profiles at three consecutive times both for immiscible (bold blue) and miscible (thin red) flows. By the dimensional argument leading to power laws (6.14) and (6.17), one can also conjecture that the averaged density profiles are self-similar in the regime of developed turbulent mixing, with the dependence only on the ratio $y/L(t)$. This conjecture is supported by Fig. 6.5(b), where the graphs from the left panel collapse into a single curve when plotted with respect to the rescaled coordinate $y/L(t)$. The graphs suggest hat the inner region of the mixing layer develops a linear average density profile with a slope decreasing proportionally to $1/L(t) \propto t^{-2}$. This linear profile implies statistical homogeneity inside the mixing layer [13]. Notice that, up to numerical fluctuations, the self-similar profiles are indistinguishable for the immiscible and miscible cases. This provides further evidence for the universality of large-scale properties in the RT turbulence for immiscible and miscible flows.

Self-similarity, homogeneity and isotropy in the statistical sense [38] are important assumptions for phenomenological theories derived similarly to the Kolmogorov's theory of turbulence (K41) [53]. For miscible Rayleigh-Taylor systems, the tendency toward isotropy restoration of small-scale fluctuations has been numerically verified by [10, 14, 16] and experimentally by [75]. The similarities of the statistics between

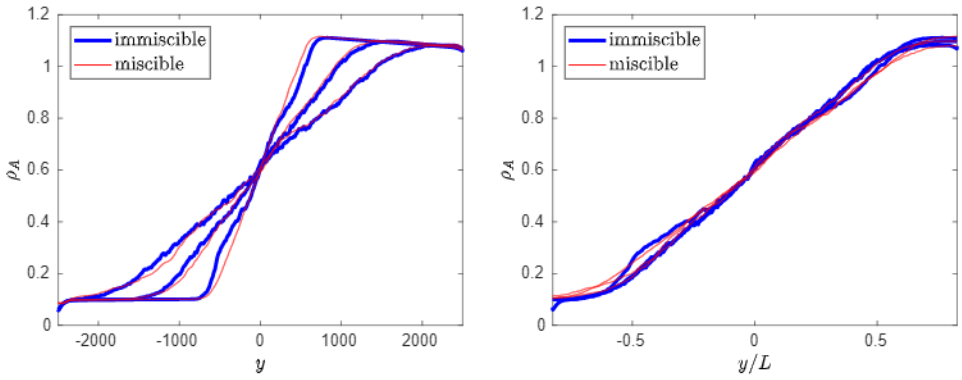

(a) (b)

Figure 6.5: Density profiles for the component A averaged with respect to horizontal coordinate x and ensemble of realizations. The results are shown at three consecutive times $t = 4.5 \times 10^4$, 7×10^4 and 8.9×10^4. (a) Dependence on the vertical coordinate y. (b) Dependence on the rescaled vertical coordinate $y/L(t)$ demonstrates self-similarity and universality of the density profile for immiscible and miscible flows.

miscible and immiscible RT flows in our experiments indicate that the same tendency may also happen for the immiscible Rayleigh-Taylor systems, which motivates the definition of turbulence for the observed late time behavior. Notice that, though numerical simulations confirm self-similar RT dynamics, some experiments report on departures from the canonical turbulence scenario with strong sensitivity to initial conditions; see e.g. [69, 68, 77].

6.2.2 Evolution of interface in the immiscible RT turbulence

An intricate evolution of the interface between two phases is the most distinctive feature of immiscible RT turbulence. In this section, we study statistical properties of the interface depending on time and scale, distribution of drops with respect to their size, and the effects of the interface on the flow.

The interface evolution with the formation of drop-rich (emulsion) regions is driven by the velocity fluctuations at small scales. In the RT turbulence, such fluctuations can be described phenomenologically assuming that the dynamics at small scales adjusts in a quasi-stationary (adiabatic) manner to the large-scale growth of the mixing layer described by the width $L(t)$ and velocity $U(t)$. In two-dimensional flows,

statistics at small-scales follows the so-called Bolgiano–Obukhov scenario [17, 71, 85], which assumes the balance of buoyancy and nonlinear terms with density fluctuations cascading toward small scales at a constant rate. For equations (2.5)–(2.6), this balance reads

$$\frac{\delta_r u}{r} \sim \mathcal{A} g \delta_r \theta, \tag{6.22}$$

where we denoted coarse-grained velocity fluctuations at scales r by $\delta_r u$ and analogous fluctuations of the order parameter by $\delta_r \theta$. With the estimate

$$\varepsilon_\theta \sim \frac{(\delta_r \theta)^2 \delta_r u}{r} \tag{6.23}$$

for the flux of order-parameter fluctuations. These laws are valid at scales of the inertial interval $\eta \ll r \ll L$ limited from below by the viscous (Kolmogorov) scale η, at which viscous forces must be taken into account. There is also a limitation caused by the interface introducing the scale ℓ of a typical drop size. We will see later that the interface affects the turbulent fluctuations considerably at scales $r \lesssim \ell$.

The change of fluctuations in time is derived using the conditions $\delta_r u \sim U(t)$ and $\delta_r \theta \sim 1$ at the scales r comparable to the size of the mixing layer $L(t)$. From (6.23), we have

$$\frac{(\delta_r \theta)^2 \delta_r u}{r} \sim \frac{U}{L} \tag{6.24}$$

combining with (6.22), we obtain [28]

$$\begin{aligned} \delta_r u &\sim \left(\frac{\alpha_L}{\alpha_U^2}\right)^{2/5} U(t) \left(\frac{r}{L(t)}\right)^{3/5} \sim \left(\frac{\alpha_U}{\alpha_L}\right)^{1/5} (\mathcal{A} g)^{2/5} \frac{r^{3/5}}{t^{1/5}}, \\ \delta_r \theta &\sim \left(\frac{\alpha_U^2}{\alpha_L}\right)^{1/5} \left(\frac{r}{L(t)}\right)^{1/5} \sim \left(\frac{\alpha_U}{\alpha_L}\right)^{2/5} (\mathcal{A} g)^{-1/5} \frac{r^{1/5}}{t^{2/5}}, \end{aligned} \tag{6.25}$$

where we used relations (6.14) and (6.17). Note that this derivation yields the well-known Bolgiano–Obukhov scaling laws $\delta_r u \propto r^{3/5}$ and $\delta_r \theta \propto r^{1/5}$. It is also important to note that these scaling laws are only approximate due to the expected intermittency [13]. The prefactors $(\alpha_U/\alpha_L)^{1/5}$ and $(\alpha_U/\alpha_L)^{2/5}$ in (6.25) are close to 1 for the experimental values of α_U and α_L shown in Figures 6.4 and 6.3, and do not generate a significant effect in the phenomelological predictions. For the sake of simplicity, these prefactors are omitted in the next calculations of this chapter.

The scale $r \sim \eta(t)$ at which viscous and nonlinear terms become comparable is found as

$$\nu \frac{(\delta_r u)}{r^2} \sim \frac{(\delta_r u)^2}{r}. \tag{6.26}$$

With the use of (6.25), this yields [28]

$$\eta(t) \sim \frac{\nu^{5/8}}{(\mathcal{A}g)^{1/4}}\, t^{1/8}. \tag{6.27}$$

In our simulation, the viscous scale computed by expression (6.27) stays close to the value $\eta \approx 4$ (four lattice distances) at all times corresponding to turbulent mixing.

Let us denote by ℓ the size of a typical drop (or the typical size of small interface structures) in the emulsion-like state; see Fig. 6.6(a). It can be estimated as the scale where kinetic and surface energy densities are of the same order [28, 72],

$$\rho_0 (\delta_\ell u)^2 \sim \frac{\gamma}{\ell}. \tag{6.28}$$

where γ is the surface tension. Using (6.25), we find

$$\ell(t) \sim \frac{\gamma^{5/11}}{\rho_0^{5/11} (\mathcal{A}g)^{4/11}}\, t^{2/11}. \tag{6.29}$$

This formula is derived under assumption that the typical drop size $\ell(t)$ exceeds the viscous scale $\eta(t)$ given by expression (6.27). As we show later in Fig. 6.6(c), a typical drop size in our simulations is about $\ell \sim 50$, which is an order of magnitude larger than the viscous scale. Therefore, ℓ belongs to the inertial interval at times corresponding to turbulent mixing.

If typical-size drops are dense (distances among drops are comparable to their sizes) in the mixing layer of width $L(t)$ and horizontal length L_x, the total number of drops is estimated as

$$\mathcal{N}_\ell(t) \sim \frac{L_x L(t)}{\ell^2(t)}. \tag{6.30}$$

This yields an estimate for the maximum total length of the interface as

$$\mathcal{L}_{tot}(t) \sim \mathcal{N}_\ell(t) \ell(t) \sim \frac{L_x L(t)}{\ell(t)}. \tag{6.31}$$

Using relations (6.14), (6.17) and (6.29), we obtain

$$\frac{\mathcal{L}_{tot}(t)}{L_x} \sim \frac{\rho_0^{5/11} (\mathcal{A}g)^{15/11}}{\sigma^{5/11}}\, t^{20/11}. \tag{6.32}$$

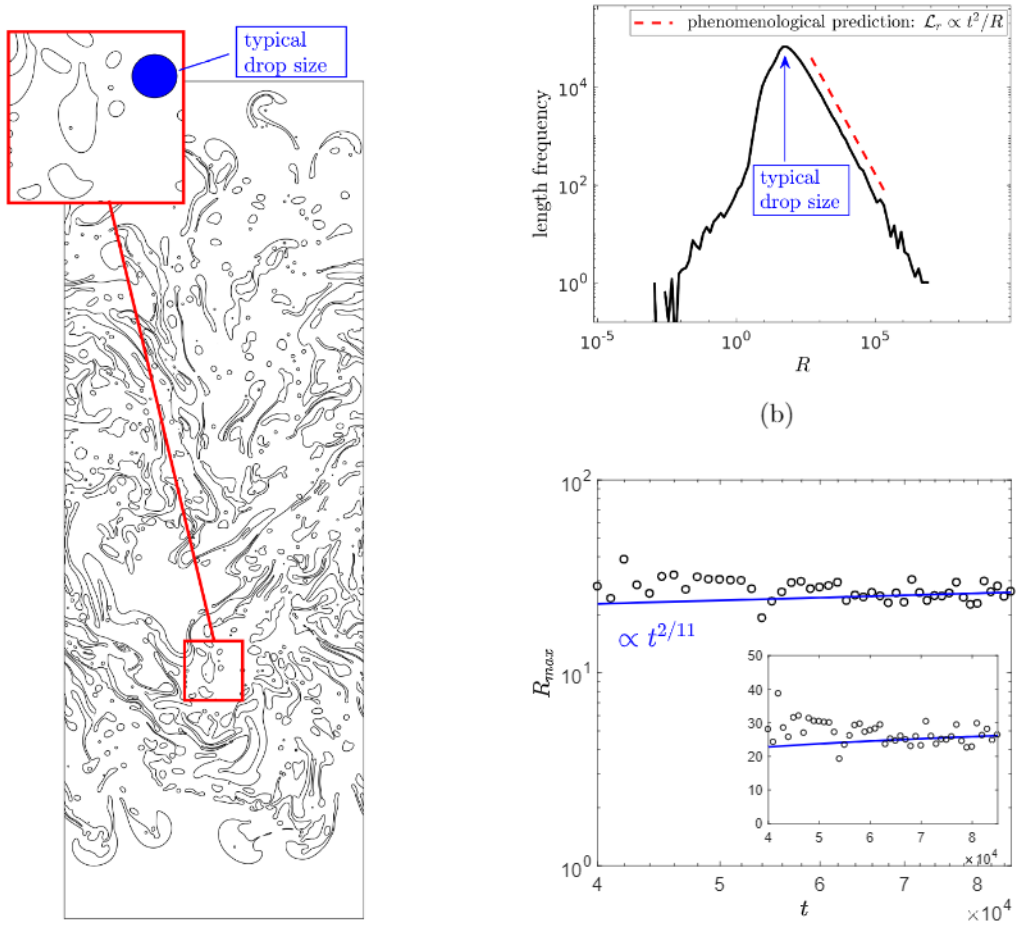

Figure 6.6: (a) Interface between two phases defined as the line of equal component densities, $\rho_A = \rho_B$, for a typical simulation of immiscible RT turbulence. The inset compares typical drops and their statistical size estimate (blue circle). (b) Length frequencies for different values of curvature radius R along the whole interface at a fixed time. We use the logarithmic binning, which corresponds to constructing the PDF for $\log R$. The PDF maximum determines a typical drop size as $\ell = 2R_{\max}$. The dashed red line corresponds to the theoretical prediction (6.34) for the dependence of interface structures on scale, i.e., $\mathcal{L}_r \propto 1/R$. (c) Temporal dependence of the typical curvature radius for times corresponding to turbulent mixing, shown in logarithmic scales; the inset shows the same graph in linear scales. The blue line corresponds to the theoretical prediction $\ell = 2R_{\max} \propto t^{2/11}$.

This expression provides, up to a dimensionless coefficient, a phenomenological estimate for the growing length of the interface.

At smaller scales, the mean kinetic energy is insufficient for forming a drop. Therefore, drops of sizes $r \ll \ell$ are very rare, being induced by extreme velocity fluctuations. On the contrary, drops can form freely at larger scales $r \gg \ell$. Let us denote by $\mathcal{N}_r$ the total number of drops having size of order r. It is estimated similarly to typical-size drops as

$$\mathcal{N}_r(t) \sim \frac{L_x L(t)}{r^2}. \tag{6.33}$$

The total interface of such drops $\mathcal{L}_r(t) \sim \mathcal{N}_r(t) r$ is expressed using relations (6.14) and (6.17) as

$$\frac{\mathcal{L}_r(t)}{L_x} \sim \mathcal{A}g \frac{t^2}{r}. \tag{6.34}$$

Naturally, this length decreases for larger r and, therefore, the total length of the interface is dominated by drops of typical size $r \sim \ell$.

In the numerical simulations, as in Chapter 5, the interface is determined as the curve, at which densities of the two components A and B are equal; see Fig. 6.6(a). Then, the typical drop size can be accessed through the measurements of the interface curvature radius $R = 1/K$, the inverse of the curvature K. Recall that we define the typical drop size as two times the most frequent curvature radius. We numerically computed the curvature radius for each adjacent pair of small interface segments at a given time t, and also associated weight using the lengths of the corresponding interface segments. More specifically, the curvatures are calculated using the following expression [34]

$$K(s) = \frac{|x'(s)y''(s) - y'(s)x''(s)|}{((x'(s))^2 + (y'(s))^2)^{2/3}}, \tag{6.35}$$

where $x(s)$ and $y(s)$ are coordinate functions of some parametrization $\mathbf{R}(s) = (x(s), y(s))$ of the interface (see Figure 5.9), and in this particular formula s is not necessarily the arc length parameter. Numerically, we can fit polygons to the vertices of the numerical interface in the form

$$x(s) = a_3 s^2 + a_2 s + a_1, \tag{6.36}$$

$$y(s) = b_3 s^2 + b_2 s + b_1, \tag{6.37}$$

where $V = (x(0), y(0))$ corresponds to the vertice. By this way, for every vertice, we fit different polygons. Then, from (6.35) follows that the curvature of at the vertice V

is given by

$$K(s) = \frac{|a_2 b_3 - b_2 a_3|}{((a_2)^2 + (b_2)^2)^{2/3}}. \tag{6.38}$$

The data for curvature for all the points of the interface is represented in the form of a histogram with logarithmic binning for the curvature radius R; see Fig. 6.6(b). This histogram approximates the (not normalized) probability density function (PDF) for the values of $\log R$ within the interface. The histogram in Fig. 6.6(b) has the well defined maximum at $R = R_{\max}(t)$, and we define the typical drop size as $\ell(t) = 2R_{\max}(t)$. The measured value is demonstrated in the inset of Fig. 6.6(a) by a blue circle of diameter ℓ, providing a visual validation of our numerical approach. The Figure 6.6(c) presents the measurements of typical drop sizes at different times shown in logarithmic scale, with the straight line corresponding to the phenomenological prediction (6.29). In addition to having a good agreement between theory and numerical simulations, we are able to estimate the dimensionless pre-factor in the expression (6.29) as 6.7 ± 0.7. Notice also that the slope of the histogram in Fig. 6.6(b) to the right of the maximum value (dashed red line) confirms our prediction (6.34) for the distribution of drops with respect to their size. This slope extends to the integral-scale structures with $R \sim L(t) \sim 10^4$. At larger values of $R \gtrsim 10^5$, Fig. 6.6(b) measures the increased probability of almost flat interfaces segments; such segments can be recognized both in Fig. 2.3 and Fig. 6.6(a).

Fig. 6.7(a) presents the temporal dependence of the total interface length in our simulations, which is computed using the Cauchy–Crofton formula [34, 61]. Its logarithmic derivative is shown in Fig. 6.7(b) demonstrating a well-established power law in the regime of turbulent mixing. The measured exponent of this power law is equal to 1.64 ± 0.07 (dashed horizontal line), which is rather close to and slightly below its theoretical estimate of $20/11$ (solid horizontal line) from Eq. (6.32). The difference between these exponents may be attributed to our theoretical assumption that typical-size drops are dense in the mixing layer. The lower numerical value of the exponent implies that typical-size drops get more sparse at larger times.

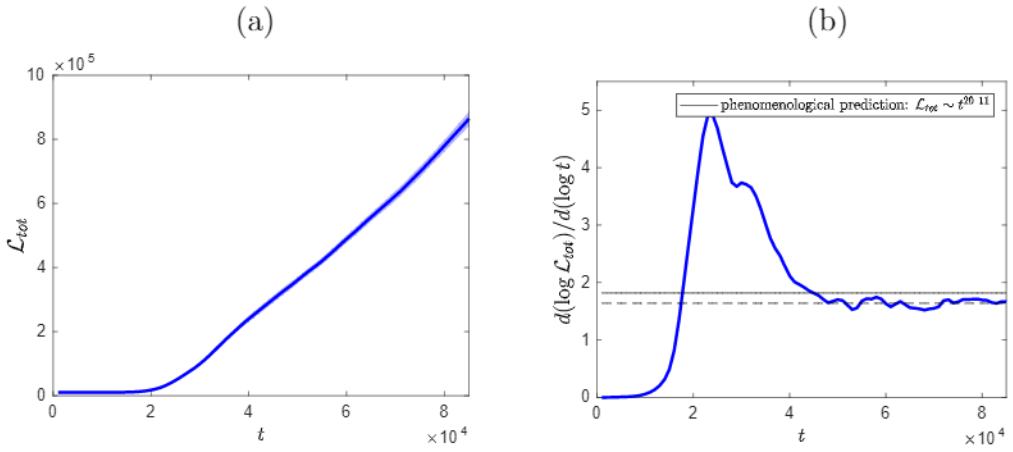

Figure 6.7: (a) Time dependence for the total interface length $\mathcal{L}_{tot}$ averaged over ensemble of 10 immiscible RT simulations; the shaded region shows standard deviations. (b) Logarithmic derivative of the previous graph, $d(\log \mathcal{L}_{tot})/d(\log t)$, indicating the power-law dependence in the turbulent regime ($t \gtrsim 4.5 \times 10^4$) with the exponent 1.64 ± 0.07 shown by a dashed horizontal line. The solid horizontal line shows the phenomenological estimate (upper bound) 20/11 for the same exponent.

6.2.3 Enstrophy and vorticity statistics

In this subsection, we study the influence of the interface on properties of the flow. Namely, we will show that the immiscible RT turbulence generates a considerable larger enstrophy compared to the miscible flow, and that the source of this extra enstrophy is confined within a small neighborhood of the interface.

The phenomenological estimate for fluctuations of the scalar vorticity $\omega = (\nabla \times \mathbf{u}) \cdot \mathbf{k}$ (where $\mathbf{k}$ is a unit vector perpendicular to the plane of the flow) in the inertial range is obtained using expression (6.25) as

$$\delta_r \omega \sim \frac{\delta_r u}{r} \sim \frac{(\mathcal{A}g)^{2/5}}{r^{2/5} t^{1/5}}. \tag{6.39}$$

Vorticity fluctuations increase at smaller scales and attain the maximum at the viscous scale $r \sim \eta(t)$. Thus, the total enstrophy of the flow $\Omega(t)$ can be estimated as a product of $(\delta_\eta \omega)^2$ and the size of the mixing layer $L(t)L_x$. Using expression (6.14) for $L(t)$ and (6.27) for $\eta(t)$, we derive the power law for the enstrophy Ω in the form

$$\frac{\Omega}{L_x} \sim (\delta_\eta \omega)^2 L(t) \sim \frac{(Ag)^2}{\nu^{1/2}} t^{3/2}. \tag{6.40}$$

Numerical verification of this relation is presented in Figs. 6.8(a,b). In the first figure, we plot the total enstrophy as a function of time for the immiscible (bold blue) and miscible (thin red) flows, and the second figure shows their logarithmic derivatives demonstrating a good agreement with the phenomenological exponent 3/2 (a horizontal line). Note that $\nu \approx 0.01$ and $D \sim 0.002$ in our miscible simulations, which implies that the particle diffusion does not affect the inertial range.

It is apparent from Fig. 6.8(a) that, despite the power-law exponents being the same in both immiscible and miscible cases, the dimensionless pre-factor is considerably larger for the immiscible flow. In Chapter 5 we argue that this difference can be attributed to the flow in a small neighborhood of the interface.

It is remarkable that the filtered part of enstrophy, which is concentrated in a thin neighborhood of the interface, follows the same power law as its bulk value, Fig. 6.8(b). We conjecture, however, that this similarity is coincidental, because the vorticity generation by the interface is not described by the Bolgiano–Obukhov scenario. The enstrophy corresponding to the interface can be estimated as a product of the total interface lengths and the linear enstrophy density; see (5.49) and (5.59). The former grows as a power law with the measured exponent 1.64 ± 0.07; see Fig. 6.7(b). The latter may depend on the drop size and velocity fluctuations, both change very slowly in time; see Eqs. (6.25) and (6.29). These estimates suggest that a power law for the enstrophy growth generated by the interface may have the exponent close to 3/2, i.e. very similar to the prediction (6.40) following from the Bolgiano–Obukhov theory.

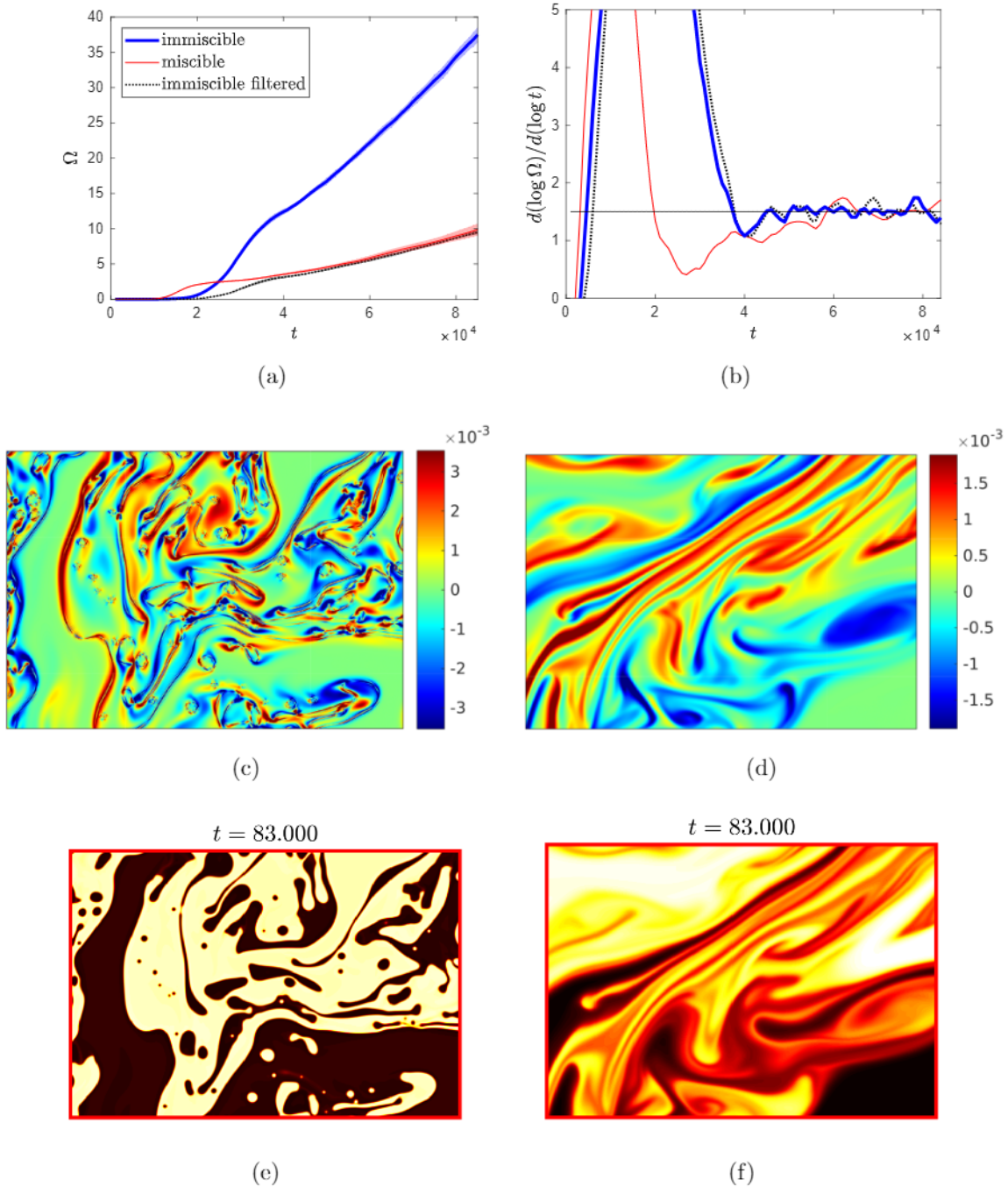

Figure 6.8: (a) Evolution of total enstrophy averaged over 10 realizations for the immiscible (bold blue) and miscible (thin red) simulations; shaded regions indicate standard deviations. The dashed black line corresponds to the filtered enstrophy of the immiscible flow, by excluding small neighborhoods of the interface. (b) Logarithmic derivatives, $d(\log \Omega)/d(\log t)$, of the same graphs compared with the theoretical power law exponent (horizontal line). (c) Example of vorticity field for immiscible and (d) miscible flow, with the respective density fields indicated in (e) for immiscible and in (f) for the miscible flow. The density field correspond to the final times in the Figures 5.1 and 5.2

6.3 Concluding remarks

In this chapter, we provided a series of phenomenological predictions for the miscible and immiscible Rayleigh-Taylor systems in the turbulent regime. We focused in the immiscible case, studying the structures of the interfaces and the evolution of the enstrophy. In this study, we can highlight the following new predictions:

$$\ell(t) \sim \frac{\gamma^{5/11}}{\rho_0^{5/11}(\mathcal{A}g)^{4/11}}\, t^{2/11}, \qquad \text{(typical drop size)} \tag{6.41}$$

$$\frac{\mathcal{L}_{tot}(t)}{L_x} \sim \frac{\rho_0^{5/11}(\mathcal{A}g)^{15/11}}{\sigma^{5/11}}\, t^{20/11}, \qquad \text{(total length of the interface)} \tag{6.42}$$

$$\frac{\mathcal{L}_r(t)}{L_x} \sim \mathcal{A}g\,\frac{t^2}{r}, \qquad \text{(total length for structures with size } r \gg \ell) \tag{6.43}$$

$$\frac{\Omega}{L_x} \sim \frac{(Ag)^2}{\nu^{1/2}}\, t^{3/2}. \qquad \text{(enstrophy)} \tag{6.44}$$

With respect to the numerical investigation, we can highlight the following results:

- We simulated the first high resolution study of the developed immiscible RT turbulence in 2D using the Shan-Chen multicomponent method.
- The large-scale statistics for mixing layer, typical velocity and average density profile have been compared with the miscible case and found to have very similar power law behaviors.
- In the immiscible case, the presence of the interface affects the small-scale statistics, leading to a significant difference, with respect to the miscible RT, in the evolution of the enstrophy.
- The evolution of the typical drop size and the total length of the interface in the emulsion-like state of developed RT turbulence are measured and shown to be compatible with our phenomenological predictions.

Chapter 7

Conclusions

We have presented the first high resolution study of the developed immiscible RT turbulence in 2D using the Shan-Chen multicomponent method. Through an appropriate choice of parameters, forcing scheme and initial configuration, we were able to simulate the Boussinesq approximation for the miscible and immiscible RT systems. The simulation of the Shan-Chen multicomponent method in GPUs made it possible to collect a robust set of statistics, allowing direct verifications of phenomenological predictions for the RT turbulence.

With the numerical results provided by the Shan-Chen model, we analyzed the energy budget of the RT turbulence (miscible and immiscible). In this analysis we found that the potential energy statistics are similar between miscible and immiscible. Significant differences were found in the kinetic energy statistics, and analyzing the components of the kinetic energy variations, we found that the differences are associated with the energy flux due to the momentum flux tensor and the viscous dissipation. We show that the flux due to the Korteweg stress tensor is corresponds to the variation of the total length of the interface, calculated numerically by the Cauchy-Crofton formula. We show indications that the interface acts as a source of vorticity, which can explain a significant part of the difference in the viscous dissipation statistics verified between miscible and immiscible flows. The results for the miscible case are in line with the current studies about energy balance found in the scientific literature [101].

Analyzing the variation of the total energy of the interface, we verify the existence of a critical time in the transition to turbulence. The analyses of the density profiles

close to this critical point show that the fast variation is associated to the first topology changes that leads to the appearance of the first drops and large disconnected clusters. This phenomenon shows similarity with similar phenomena associated with bifurcation points observed in the context of the one-dimensional Cahn-Hilliard equation. [6].

In the final part of the thesis, supported by the results of the energy budget analysis, we approach a phenomenological theory for the 2D Rayleigh-Taylor turbulence. In the numerical verifications of this phenomenology, we showed that the large-scale statistics for mixing layer, typical velocity and average density profile have been compared with the miscible case and found to have very similar power law behaviours with close overall prefactors but different transient behavior. In the immiscible case, the presence of the interface affects the small-scale statistics, leading to a significant difference, with respect to the miscible RT, in the evolution of the enstrophy. The Bolgiano–Obukhov assumption generates a valid prediction for the power law behaviour of the temporal evolution of total enstrophy also for the immiscible case (see eq. (6.40)), but does not account for the big change in the prefactor, which could be affected by extra vorticity induced by the interface. The evolution of the typical drop size and the total length of the interface in the emulsion-like state of developed RT turbulence are measured and shown to be compatible with our phenomenological predictions.

A natural question that can be addressed in the future is about the statistics of the structures with a typical size smaller then the typical drop size. In this range of scales, the presence of capillary waves propagating along the interfaces of the drops is expected [29]. The developed numerical scheme can also be applied to the problem of fragmentation and whitecapping at the surface of breaking waves, which involves a complex process with formation of drops and bubbles; see e.g. [35, 67]. It is also important to note that most of the numerical procedures presented in this article are naturally extendable for the three-dimensional immiscible Rayleigh-Taylor turbulence, which is a more suitable configuration for experimental procedures, although such an extension of the present GPU code, with appropriate optimizations to obtain affordable statistics, can be a non-trivial task. Some laboratory experiments for the two-dimensional case may be conducted in thin liquid films [102, 22] using, for example, aqueous gelatin solutions with very high concentration [69]. The corresponding extension of the lattice Boltzmann method to these case seems feasible, but requires further study.

Appendices

Appendix A

Diffuse interface models

In this appendix, we briefly discuss the general equations of the so-called diffuse interface methods for multicomponent flows. The Shan-Chen method described in Chapter 3 is included in this class of methods. In the two-dimensional sharp interface models, the interface is a 1D boundary which is mostly represented by an the order parameter ϕ (see Chapter 2) which is discontinuous at the interface. In the numerical methods based on this formulation, the motion of the interface need to be explicit tracked, requiring extra solvers on either side of the boundary [55]. Such numerical methods have well known problems associated with topological changes in the fluid domains [100].

In the diffuse interface approach, the main idea is to replace the sharp interface with a diffuse one in such a way that the computation of the interface dynamics can be performed on fixed grids [25]. In this approach, the order parameter smoothly varies across the interface between the two bulk values. The length scale that characterizes the variation in the density profile across the interface is called the interface width, to be defined with precision later in this appendix.

In the first part of this appendix we consider, like in Chapter 3, a mixture of two components A and B with the respective the number of molecules per unit of volume given by n_A and n_B. The smoothness of the macroscopic quantities of the fluid system at the interface can be obtained by taking mesoscopic averages over a large enough local volume in the fluid domain. This leads to a set of equations for mixtures of incompressible Newtonian fluids that corresponds to almost the same equations of

motion obtained by the lattice-Boltzmann method in Chapter 3. Thereafter, we characterize the sharp interface limit, and in the final section, we approach the relationship between the free-energy of the RT system and the other forms of energy described in Chapter 5.

A.1 Diffuse interface formulation

In this section, we approach the formulation of equations of motion of the Rayleigh-Taylor system described in the Chapter 2 assuming a diffuse interface. This formulation is essentially a coarse-graining analysis of the dynamics of the system. Consider the following definition for the order parameter [23]

$$\phi(\mathbf{x}) = \frac{\langle n_A - n_B \rangle_{meso}}{\langle n_A + n_B \rangle_{meso}} \tag{A.1}$$

where $n_{A,B}$ denotes the number of molecules of the components A and B per unit of volume locally, respectively. For the sake of simplicity, we assume the molecules of the of the components A and B have the same constant molecular volume; the mesoscopic average is taken over a large enough local volume V_{meso} of a region with geometrical center in a point $\mathbf{x}$ of the fluid domain Ω. By this way the order parameter vary smoothly across the interface between the two bulk values such that $-1 \leq \phi \leq 1$, with $\phi = \pm 1$ within the bulk regions. Different ways to smooth the interface can also be used [18].

The diffuse-interface models can be viewed as a physically motivated methods, describing the interface dynamics by the idea of mixing energy. The structure of the interface is determined by molecular forces; the tendencies for mixing and demixing are balanced through the non-local mixing energy [100]. The idea of mixing energy can be formalized by the assumption of the Girzburg-Landau-Wilson [32] (GLW) free energy given by

$$F[\rho, \phi] = \int_{\Omega} \left[V(\rho, \phi) + \frac{k}{2} |\nabla \phi|^2 \right] d\mathbf{x}, \tag{A.2}$$

where Ω is the region occupied by the system, $V(\rho, \phi)$ is the bulk potential and drives the system towards demixing while the term $k\frac{|\nabla\phi|^2}{2}$ favors a perfect mixing. The non-trivial equilibrium state is the result of this competition [26]. The GLW functional is originated from a mean field analysis of the configurational partition function of the

system [45, 59]. For the Shan-Chen method described in Chapter 3, we have

$$k \sim \frac{G_{AB} c_s^4}{4}. \tag{A.3}$$

for $\tau \gg 1/2$.

The equilibrium state is the minimizer of the free-energy F, i.e., a configuration such that

$$\mu = \frac{\delta F}{\delta \phi} = \frac{\partial V}{\partial \phi} - k\Delta\phi = 0 \tag{A.4}$$

where μ is the chemical potential. If we impose a perturbation of the equilibrium configuration of the system, this perturbation will displace the phase field to a new configuration for which in general $\mu \neq 0$. The system will try to react in a such way to reach again an equilibrium configuration [25]. The approach to equilibrium for the system implies that the free-energy F steadily decreases to approaches a minimum. The conservation of mass in the system implies that the evolution of the phase field is subject to the constraint

$$\int_\Omega \phi(\mathbf{x}, t) d\mathbf{x} = 0. \tag{A.5}$$

for a symmetric binary mixture. In the RT systems, we also consider periodic boundary conditions in the horizontal direction and vanishing derivatives in the vertical direction as boundary conditions for the order parameter. One solution for the phase field dynamics is given in terms of gradient flow of F. i.e.,

$$\frac{\partial \phi}{\partial t} + \nabla \cdot (\mathbf{u}\phi) = -M \mathrm{grad}_0 F(\phi) \tag{A.6}$$

M is a coefficient called mobility and the symbol grad_0 represents the sense of the Gâteaux derivative on the subspace of $H^1(\Omega)$ given by the mass-conserving functions(see [36]) satisfying (A.5) [37]. As a consequence of the Lax–Milgram theorem [60], we have $\mathrm{grad}_0 F[\phi] = -\Delta\mu$, where $\mu = \frac{\delta F}{\delta \phi}$ is the chemical potential of the system. Thus, the equation (A.6) becomes

$$\frac{\partial \phi}{\partial t} + \nabla \cdot (\mathbf{u}\phi) = M\Delta\mu, \tag{A.7}$$

this is the so-called the Cahn-Hilliard equation. For a mixture of incompressible miscible fluids, it is possible to approximate $\Delta\mu$ by $\Delta\phi$ up to a multiplicative constant, obtaining the transport equation (2.37), as shown with more details in Chapter 3 in the context of the lattice Boltzmann method.

Momentum balance equation and Boussinesq approximation

The functional (A.2) also gives information about the momentum balance equation of the system by the introduction of the action functional [65]

$$A(\mathbf{x}) = \int_0^T \int_{\Omega_0} \left\{ \frac{\rho}{2} |\mathbf{x}_t(\mathbf{X},t)|^2 - F[\rho(\mathbf{x}(\mathbf{X},t), \phi(\mathbf{x}(\mathbf{X},t)] \right\} d\mathbf{X}dt \tag{A.8}$$

where $\mathbf{X}$ is the initial Lagrangian material coordenate and $\mathbf{x}(\mathbf{X},t)$ is the Eulerian coordinate. The set Ω_0 is the initial domain occupied by the fluids, which is constant for the applications under consideration in this theses. For incompressible materials, we look at the volume preserving flows such that

$$\mathbf{x}_t(\mathbf{X},t) = \mathbf{u}(\mathbf{x}(\mathbf{X},t)), \quad \mathbf{x}(\mathbf{X},0) = \mathbf{X}. \tag{A.9}$$

By the least action principle [65, 100, 19], the linear momentum balance equation shall be the least action state in a system without viscosity. As a result, we obtain the following Euler equation

$$\rho \left(\frac{\partial \mathbf{u}}{\partial t} + \mathbf{u} \cdot \nabla \mathbf{u} \right) = -\nabla \cdot \mathbf{P} \tag{A.10}$$

where $\mathbf{P}$ is a second order stress tensor given by

$$\mathbf{P} = \left[\phi \frac{\partial V(\phi,\rho)}{\partial \phi} + \rho \frac{\partial V(\phi,\rho)}{\partial \rho} - V(\phi,\rho) - k\phi\Delta\phi - \frac{k}{2}|\nabla\phi|^2 \right] \mathbf{I} + k \nabla\phi \otimes \nabla\phi. \tag{A.11}$$

This tensor is analogous to the pressure tensor $\mathbf{P}^{(TOT)}$ obtained Chapter 3 for the Shan-Chen method.

We can separate two part in the stress tensor (A.11)

$$p_b = \phi \frac{\partial V(\phi,\rho)}{\partial \phi} + \rho \frac{\partial V(\phi,\rho)}{\partial \rho} - V(\phi,\rho), \tag{A.12}$$

$$\mathbf{P}^K = \left[-k\phi\Delta\phi - \frac{k}{2}|\nabla\phi|^2 \right] \mathbf{I} + k \nabla\phi \otimes \nabla\phi, \tag{A.13}$$

where p_b is called the *bulk pressure* and $\mathbf{P}^K$ is so-called the *Korteweg stress tensor* [95].

The tensor $\mathbf{P}^K$ accounts for the effects of the interface and surface tension [3], incorporating the kinematic boundary conditions (2.4) by replacing the pressure tensor $p\mathbf{I}$ by the smooth anisotropic stress tensor (A.11) in the Navier-Stokes equation (2.1). Including the effects of the viscosity and the gravitational force, the equation (A.10) becomes

$$\rho \left(\frac{\partial \mathbf{u}}{\partial t} + \mathbf{u} \cdot \nabla \mathbf{u} \right) = -\nabla \cdot \mathbf{P} + \nabla \cdot [\eta(\nabla \mathbf{u} + \nabla \mathbf{u}^T)] - \rho g \mathbf{e}_y. \tag{A.14}$$

In the Boussinsq approximation, the density fluctuations affects only the buoyancy term [56, 51]. Considering (2.6), the Boussinesq approximation leads to

$$\rho_0\left(\frac{\partial \mathbf{u}}{\partial t}+\mathbf{u}\cdot\nabla\mathbf{u}\right)=-\nabla\cdot(\mathbf{P}+\rho_0 gy\mathbf{I})+\nabla\cdot[\eta(\nabla\mathbf{u}+\nabla\mathbf{u}^T)]-\mathcal{A}g\phi\mathbf{e}_y, \tag{A.15}$$

where $\mathcal{A}$ is the Atwood number (see Chapter 2) and $\rho_0=(\rho_A+\rho_B)/2$ is the background density. Denoting $\mathcal{A}g=\tilde{g}$ as the buoyancy intensity and $\overline{\mathbf{P}}=\mathbf{P}+\rho_0 gy\mathbf{I}$, we obtain the equations of motion of the system

$$\begin{aligned}\rho_0\left(\frac{\partial \mathbf{u}}{\partial t}+\mathbf{u}\cdot\nabla\mathbf{u}\right) &= -\nabla\cdot\overline{\mathbf{P}}+\nabla\cdot[\eta(\nabla\mathbf{u}+\nabla\mathbf{u}^T)]-\phi\tilde{g}\mathbf{e}_y, &\text{(A.16)}\\ \nabla\cdot\mathbf{u} &= 0, \quad \text{on} \quad \Omega. &\text{(A.17)}\end{aligned}$$

Considering also the equation (A.7) and the boundary conditions, we obtain the diffuse interface formulation of the Rayleigh-Taylor systems for small Atwood numbers described in Chapter 2.

A.2 The sharp interface limit

A common form for the bulk potential $V(\rho,\phi)$ in the functional (A.2) is given by the Helmholtz free energy for binary mixtures [32]:

$$V(\rho,\phi)=k_BT\left(\frac{\rho+\phi}{2}\right)\log\left(\frac{\rho+\phi}{2}\right)+k_BT\left(\frac{\rho-\phi}{2}\right)\log\left(\frac{\rho-\phi}{2}\right)+k_BT\chi\left(\frac{\rho^2-\phi^2}{4}\right),$$

k_B is the Boltzmann constant, T is the absolute temperature and χ is a function of the temperature describing the enthalpic interaction between the two species [24]. If χ is large and positive the separation of the components is favorable, i.e., if $\chi<\chi_c$ the mixture is miscible and immiscible for $\chi>\chi_c$ for some critical value χ_c depending on the substances involved in the mixture. In the Shan-Chen multicomponent method shown in Chapter 3, the interaction parameter G_{AB} plays the role of the parameter χ. Also, the value k_BT corresponds to the square of the speed of sound, which in the is denoted by c_s^2 in Shan-Chen multicomponent method.

Many features of kinetics of the system are insensitive to the detailed shape of $V(\rho,\phi)$ [32]. Lets consider the Landau expansion of the free energy around the critical point $\phi_c=0$ up to fourth order

$$V(\rho,\phi)=V(\rho,0)+\frac{1}{2}a_2\phi^2+\frac{1}{4}a_4\phi^4 \tag{A.18}$$

where $a_2 = \dfrac{\partial^2 V}{\partial \phi^2}(\rho, 0)$ and $a_4 = \dfrac{\partial^4 V}{\partial \phi^4}(\rho, 0)$ is a temperature independent constant. We can set $V(\rho, 0) = 0$ without loss of generality, as a consequence of the incompressibility condition. The odd powers of ϕ are not taken into account in the Landau expansion if we assume symmetry between ϕ and $-\phi$ like in a symmetric 50-50 binary mixture [32]. $V(\rho, \phi)$ has a single minimum for $\chi < \chi_c$, and two minima for $\chi > \chi_c$ at

$$\pm\phi_{min} = \pm[-a_2/a_4]^{1/2} \tag{A.19}$$

corresponding to the two coexisting components in equilibrium. For the Shan-Chen method described in Chapter 3, we have [82]

$$|a_2| \sim \frac{G_{AB} c_s^2}{2}, \tag{A.20}$$

for $\tau \gg 1/2$.

Let us now consider an interface between the two components. In the following we derive an analytical expression for surface tension and interface width. First, it is important to note that these quantities are associated with the calculus of the chemical potential of the system. When the system is in equilibrium the thermodynamic force density $F = -\phi \nabla \mu$ must be zero, which implying in a constant chemical potential, i.e.

$$a_2\phi + a_4\phi^3 - k\Delta\phi = \text{const.} \tag{A.21}$$

Let us introduce a dimensionless order parameter $\overline{\phi} = \phi/\phi_{min}$. The equation (A.21) becomes

$$a_2\overline{\phi} - a_2\overline{\phi}^3 - k\Delta\overline{\phi} = \text{const.} \tag{A.22}$$

We can set the constant to be zero looking at the bulk regions where $\phi = \pm\phi_{min}$. For simplicity, let us assume that the two fluids are separated by a planar interface, whose normal is in the y direction. We have $\overline{\phi} = \pm 1$ when $y = \pm\infty$, i.e., in the bulk regions. In this context, the equation (A.22) has an interface solution [55] given by

$$\overline{\phi} = \tanh\left(\frac{y}{\sqrt{2}\delta}\right) \quad \therefore \quad \phi = \phi_{min} \tanh\left(\frac{y}{\sqrt{2}\delta}\right), \tag{A.23}$$

where

$$\delta = \sqrt{k/|a_2|}, \tag{A.24}$$

is the **interface width**, also called **correlation length** [32].

The interfacial tension γ in diffuse interface models corresponds the surface excess free energy F per unit area when the reference surface $y = 0$ is chosen in such a way that

$$\int_{-\infty}^{0} (\phi(y) + \phi_{min})dy + \int_{0}^{\infty} (\phi(y) - \phi_{min})dy = 0. \tag{A.25}$$

Then

$$\gamma = \int_{-\infty}^{\infty} \left[\Delta V + \frac{k}{2} \left(\frac{d\phi(y)}{dy} \right)^2 \right] dy, \tag{A.26}$$

where

$$\Delta V = \begin{cases} (V(\rho, \phi) - V(\rho, -\phi_{min})), & \text{for } -\infty < y < 0. \\ (V(\rho, \phi) - V(\rho, \phi_{min})), & \text{for } 0 < y < \infty. \end{cases}$$

The equilibrium order parameter profile minimizes the excess surface free energy. Thus

$$k\frac{d^2\phi(y)}{dy^2} - \frac{d\Delta V}{d\phi} = 0, \tag{A.27}$$

multiplying by $(\frac{d\phi}{dy})$ we can integrate this equation to obtain

$$\Delta V(\rho, \phi) = \frac{k}{2} \left(\frac{d\phi(y)}{dy} \right)^2. \tag{A.28}$$

Consequently, we can obtain the surface tension as

$$\gamma = k \int_{-\infty}^{\infty} \left(\frac{d\phi(y)}{dy} \right)^2 dy. \tag{A.29}$$

The expression (A.29) defines the so called mean field surface tension. In Chapter 3, we show a similar expression for the surface tension in the context of the lattice Boltzmann method. Substituting the interface solution (A.23) into (A.29), we obtain

$$\gamma = \phi_{min}^2 \sqrt{\frac{8k|a_2|}{9}}. \tag{A.30}$$

The **sharp interface limit** is obtained using parametrized parameters: $a_2^\varepsilon = a_2/\varepsilon$, $a_4^\varepsilon = a_4/\varepsilon$ and $k^\varepsilon = \varepsilon k$. In the limit $\varepsilon \to 0$, the values of γ and ϕ_{min} are kept constant while the interface width δ is sent to zero. For more details, see [42, 3].

Consider the non-equilibrium state with a moving interface given by $\Gamma(t) = \{\mathbf{x} \in \Omega;\ \phi(\mathbf{x}, t) = 0\}$, for a immiscible binary mixture. For a given test function $\mathbf{w} \in C_c^\infty(\Omega \times [0, T); \mathbb{R}^3)$ with compact support, we have the following relations for sufficient small values of curvatures [65, 32]

$$\int_\Omega (\nabla \cdot \mathbf{P}^K).\mathbf{w} = k^\varepsilon \int_\Omega \Delta\phi\nabla\phi \cdot \mathbf{w} \simeq k^\varepsilon \int_\Omega |\nabla\phi|^2 K \frac{\nabla\phi}{|\nabla\phi|} \cdot \mathbf{w} \simeq \int_{\Gamma(t)} \gamma\kappa\mathbf{n} \cdot \mathbf{w}. \tag{A.31}$$

where $\mathbf{n} = \frac{\nabla\phi}{|\nabla\phi|}$ and is the normal field on $\Gamma(t)$, $K = -\nabla\cdot\mathbf{n}$ is the scalar curvature and $\mathbf{P}^K$ is the pressure tensor given by (A.13). The relations in (A.31) roughly elucidates the connection between the stress tensor $\mathbf{P}^K$ with the kinematic boundary conditions (2.4) in the sharp interface formulation. Also, analogously to the calculations in Chapter 5, is possible to show that $\mathbf{P}^K$ is directly connected to the variation of the energy of the interface.

A.3 Free-energy and the energy budget for the RT systems

In this section, we study the energy budget for the Rayleigh-Taylor systems in the context of a general diffuse interface model, analogously to what was shown in Chapter 5. The formulas are mostly based on the Boussinesq approximation formed by (A.16) and (A.17). We consider immiscible and miscible Rayleigh-Taylor flows as we explained in Chapter 2, see Figures 5.1 and 5.2, with a domain with size $|D| = L_x \times L_y$.

Defining the free-energy density of the system by $E_F = F/|D|$, where F is the free-energy functional (A.2), we can define the total energy for the Rayleigh-Taylor systems as [25]

$$E = E_k + E_p + E_F. \tag{A.32}$$

In the following we elucidate the energy exchanges between E_k, E_p and E_F. We first calculate the evolution of the free energy disregarding the diffusion term in the Cahn-Hilliard equation, i.e., we first consider

$$\frac{\partial\phi}{\partial t} + \nabla(\phi\mathbf{u}) = 0. \tag{A.33}$$

Let us call this variation as $\partial_t F_1$, we have

$$\begin{aligned}
\partial_t F_1 &= \int_\Omega \left(\frac{\partial V}{\partial\rho}\frac{\partial\rho}{\partial t} + \frac{\partial V}{\partial\phi}\frac{\partial\phi}{\partial t} + k\nabla\phi\cdot\nabla\frac{\partial\phi}{\partial t}\right) d\mathbf{x} \\
&= \int_\Omega \left(\frac{\partial V}{\partial\rho}(-\nabla\cdot(\rho\mathbf{u})) + \frac{\partial V}{\partial\phi}(-\nabla\cdot(\phi\mathbf{u})) - k\Delta\phi\frac{\partial\phi}{\partial t}\right) d\mathbf{x} \\
&= \int_\Omega \left(\rho\nabla\left(\frac{\partial V}{\partial\rho}\right)\cdot\mathbf{u} + \phi\nabla\left(\frac{\partial V}{\partial\phi}\right)\cdot\mathbf{u} + k\Delta\phi(\nabla\cdot(\phi\mathbf{u}))\right) d\mathbf{x} \\
&= \int_\Omega \left(\rho\nabla\left(\frac{\partial V}{\partial\rho}\right)\cdot\mathbf{u} + \phi\nabla\left(\frac{\partial V}{\partial\phi}\right)\cdot\mathbf{u} - k\phi\nabla(\Delta\phi)\cdot\mathbf{u}\right) d\mathbf{x}.
\end{aligned} \tag{A.34}$$

Using the identity

$$\phi\nabla(\Delta\phi) = \nabla\cdot\left(\left[-k\phi\Delta\phi - \frac{k}{2}|\nabla\phi|^2\right]\mathbf{I} + k\nabla\phi\otimes\nabla\phi\right), \tag{A.35}$$

we obtain

$$\begin{aligned}
\partial_t F_1 &= \int_\Omega \left(\nabla\left(\phi\frac{\partial V}{\partial\phi} + \rho\frac{\partial V}{\partial\rho}\right)\cdot\mathbf{u} - \nabla V\cdot\mathbf{u} + \right. \\
&+ \left.\nabla\cdot\left(\left[k\phi\Delta\phi + \frac{k}{2}|\nabla\phi|^2\right]\mathbf{I} - k\nabla\phi\otimes\nabla\phi\right)\cdot\mathbf{u}\right)d\mathbf{x} \\
&= \int_\Omega \nabla\cdot\left(\left[\phi\frac{\partial V(\phi,\rho)}{\partial\phi} + \rho\frac{\partial V(\phi,\rho)}{\partial\rho} - V(\phi,\rho) - \right.\right. \\
&- \left.\left. k\phi\Delta\phi - \frac{k}{2}|\nabla\phi|^2\right]\mathbf{I} + k\nabla\phi\otimes\nabla\phi\right)\cdot\mathbf{u}\; d\mathbf{x}.
\end{aligned} \tag{A.36}$$

Thus,

$$\partial_t F_1 = \langle(\nabla\cdot\mathbf{P})\cdot\mathbf{u}\rangle\,|D|. \tag{A.37}$$

where $\mathbf{P}$ is given by (A.11). Consider now the Cahn-Hilliard equation (A.7) without the convective part, i.e.,

$$\frac{\partial\phi}{\partial t} = \nabla\cdot(M\nabla\mu), \tag{A.38}$$

the respective free-energy variation, indicated by $\partial_t F_2$, is given by

$$\begin{aligned}
\partial_t F_2 &= \int_\Omega \left(\frac{\partial V}{\partial\phi}\nabla\cdot(M\nabla\mu) + k\nabla\phi\cdot\nabla(\nabla\cdot(M\nabla\mu))\right)d\mathbf{x} \\
&= \int_\Omega \left(-\nabla\left(\frac{\partial V}{\partial\phi}\right)\cdot(M\nabla\mu) + k\nabla\phi\cdot\nabla(\nabla\cdot(M\nabla\mu))\right)d\mathbf{x} \\
&= \int_\Omega \left(-\nabla\left(\frac{\partial V}{\partial\phi}\right)\cdot(M\nabla\mu) - k\Delta\phi(\nabla\cdot(M\nabla\mu))\right)d\mathbf{x} \\
&= \int_\Omega \left(-\nabla\left(\frac{\partial V}{\partial\phi} - k\Delta\phi\right)\cdot(M\nabla\mu)\right)d\mathbf{x} \\
&= \int_\Omega \left(-\nabla\left(\frac{\delta F}{\delta\phi}\right)\cdot(M\nabla\mu)\right)d\mathbf{x} \\
&= \int_\Omega -M|\nabla\mu|^2 d\mathbf{x} = -\left\langle M|\nabla\mu|^2\right\rangle|D|.
\end{aligned} \tag{A.39}$$

where M is the mobility coefficient. Therefore, the total variation of the free energy density E_F is given by

$$\partial_t E_F = \langle(\nabla\cdot\mathbf{P})\cdot\mathbf{u}\rangle - \left\langle M|\nabla\mu|^2\right\rangle|D|. \tag{A.40}$$

Neglecting the variations of the total density ρ, we have

$$\partial_t E_F = \left\langle(\nabla\cdot\mathbf{P}^K)\cdot\mathbf{u}\right\rangle - \left\langle M|\nabla\mu|^2\right\rangle, \tag{A.41}$$

where $\mathbf{P}^k$ is the Korteweg stress tensor (A.13).

Considering also the formulas for variation of E_k and E_p shown in Chapter 5, we obtain the following set of equations

$$\partial_t E_p = \langle \mathbf{u} \cdot \phi \tilde{g} \mathbf{e}_y \rangle \tag{A.42}$$

$$\partial_t E_K = -\left\langle \mathbf{u} \cdot (\nabla \cdot \mathbf{P}^K) \right\rangle - \eta \left\langle |\nabla \mathbf{u}|^2 \right\rangle - \langle \mathbf{u} \cdot \phi \tilde{g} \mathbf{e}_y \rangle \tag{A.43}$$

$$\partial_t E_F = \left\langle \mathbf{u} \cdot (\nabla \cdot \mathbf{P}^K) \right\rangle - \left\langle M |\nabla \mu|^2 \right\rangle . \tag{A.44}$$

This set of equations shows the direct correspondence between the different forms of energy in the Rayleigh-Taylor flows. For these systems, the gravitational potential energy becomes kinetic energy, and part of the kinetic energy becomes free-energy.

Consequently, the variation of the total energy of Rayleigh-Taylor systems in Chapter 2 is given by

$$\partial_t E = \partial_t E_p + \partial_t E_k + \partial_t E_F = -\eta \left\langle |\nabla \mathbf{u}|^2 \right\rangle - \left\langle M |\nabla \mu|^2 \right\rangle . \tag{A.45}$$

It shows that, even without viscosity, the Rayleigh-Taylor systems are dissipative.

Energy of the interface

In a symmetric system (a 50-50 mixture with density matched) the energy of the interface can be estimated by the excess of free-energy at the interface compared to the bulk regions [32, 42, 3]. This excess of free-energy is given by

$$\Delta F = \int_\Omega \left(\Delta V + \frac{k}{2} |\nabla \phi|^2 \right) d\mathbf{x} \tag{A.46}$$

where

$$\Delta V = (V(\rho, \phi) - V(\rho, 1))(1 - \phi(\mathbf{x})) + (V(\rho, \phi) - V(\rho, -1))\phi(\mathbf{x}). \tag{A.47}$$

Using the system of local coordinates (5.16) introduced in Chapter 5, we have

$$\nabla \phi = \mathbf{n} \left(\frac{\partial \phi}{\partial u} \right) + \mathbf{t} \left(\frac{\partial \phi}{\partial s} \right) , \tag{A.48}$$

where s is arc length parameter, from which follows

$$|\nabla \phi|^2 = \left(\frac{\partial \phi}{\partial u} \right)^2 + \left(\frac{\partial \phi}{\partial s} \right)^2 \approx \left(\frac{\partial \phi}{\partial u} \right)^2 , \tag{A.49}$$

where the last approximation holds for small values of curvatures [32].

For very small values of the interface width (A.24), it is expected the following approximation [96]

$$\Delta V \simeq \frac{k}{2}|\nabla\phi|^2. \tag{A.50}$$

Consequently, from (A.46) we can write

$$\int_\Omega \left(\Delta V + \frac{k}{2}|\nabla\phi|^2\right) d\mathbf{x} \simeq k\int_\Omega \left(\frac{\partial\phi}{\partial u}\right)^2 dsdu = \int_{\Gamma(t)} \gamma ds = \gamma\mathcal{L}_{tot}, \tag{A.51}$$

where $\mathcal{L}_{tot}$ is the total length of the interface and γ is the surface tension coefficient given by (A.30).

Bibliography

[1] S. I. Abarzhi, A. Gorobets, and K. R. Sreenivasan, *Rayleigh–Taylor turbulent mixing of immiscible, miscible and stratified fluids*, Physics of Fluids, 17 (2005), p. 081705.

[2] M. S. Alam and L. Cheng, *Parallelization of lbm code using cuda capable gpu platform for 3d single and two-sided non-facing lid-driven cavity flow*, in International Conference on Offshore Mechanics and Arctic Engineering, vol. 44397, 2011, pp. 745–753.

[3] D. M. Anderson, G. B. McFadden, and A. A. Wheeler, *Diffuse-interface methods in fluid mechanics*, Annual review of fluid mechanics, 30 (1998), pp. 139–165.

[4] T. Astoul, G. Wissocq, J.-F. Boussuge, A. Sengissen, and P. Sagaut, *Analysis and reduction of spurious noise generated at grid refinement interfaces with the lattice boltzmann method*, Journal of Computational Physics, (2020), p. 109645.

[5] R. Benzi, M. Sbragaglia, S. Succi, M. Bernaschi, and S. Chibbaro, *Mesoscopic lattice Boltzmann modeling of soft-glassy systems: theory and simulations*, The Journal of Chemical Physics, 131 (2009), p. 104903.

[6] A. Bertozzi, T. Kolokolnikov, and W. Liu, *Diffuse interface surface tension models in an expanding flow*, Communications in Mathematical Sciences, 10 (2012), pp. 387–418.

[7] C. Bianca and C. Dogbe, *On the Boltzmann gas mixture equation: Linking the kinetic and fluid regimes*, Communications in Nonlinear Science and Numerical Simulation, 29 (2015), pp. 240–256.

[8] L. Biferale, G. Boffetta, A. A. Mailybaev, and A. Scagliarini, *Rayleigh-Taylor turbulence with singular nonuniform initial conditions*, Physical Review Fluids, 3 (2018), p. 092601.

[9] L. Biferale, F. Mantovani, M. Pivanti, F. Pozzati, M. Sbragaglia, A. Scagliarini, S. F. Schifano, F. Toschi, and R. Tripiccione, *Optimization of multi-phase compressible lattice boltzmann codes on massively parallel multi-core systems*, Procedia Computer Science, 4 (2011), pp. 994–1003.

[10] L. Biferale, F. Mantovani, M. Sbragaglia, A. Scagliarini, F. Toschi, and R. Tripiccione, *High resolution numerical study of Rayleigh–Taylor turbulence using a thermal lattice boltzmann scheme*, Physics of Fluids, 22 (2010), p. 115112.

[11] L. Biferale, M. Sbragaglia, A. Scagliarini, F. Mantovani, M. Pivanti, S. Schifano, R. Tripiccione, F. Pozzati, and F. Toschi, *Lattice boltzmann method simulations on massively parallel multi-core architectures.*, 01 2011, pp. 73–80.

[12] F. Blanchette and Y. Lei, *Energy considerations for multiphase fluids with variable density and surface tension*, SIAM review, 51 (2009), pp. 423–431.

[13] G. Boffetta and A. Mazzino, *Incompressible Rayleigh–Taylor turbulence*, Annual Review of Fluid Mechanics, 49 (2017), pp. 119–143.

[14] G. Boffetta, A. Mazzino, S. Musacchio, and L. Vozella, *Kolmogorov scaling and intermittency in rayleigh-taylor turbulence*, Physical Review E, 79 (2009), p. 065301.

[15] G. Boffetta, A. Mazzino, S. Musacchio, and L. Vozella, *Rayleigh–Taylor instability in a viscoelastic binary fluid*, Journal of Fluid Mechanics, 643 (2010), pp. 127–136.

[16] G. Boffetta, A. Mazzino, S. Musacchio, and L. Vozella, *Statistics of mixing in three-dimensional rayleigh–taylor turbulence at low atwood number and prandtl number one*, Physics of Fluids, 22 (2010), p. 035109.

[17] R. Bolgiano Jr, *Turbulent spectra in a stably stratified atmosphere*, Journal of Geophysical Research, 64 (1959), pp. 2226–2229.

[18] J. U. Brackbill, D. B. Kothe, and C. Zemach, *A continuum method for modeling surface tension*, Journal of computational physics, 100 (1992), pp. 335–354.

[19] J. Brannick, C. Liu, T. Qian, and H. Sun, *Diffuse interface methods for multiple phase materials: an energetic variational approach*, arXiv preprint arXiv:1402.5375, (2014).

[20] M. Brøns, M. C. Thompson, T. Leweke, and K. Hourigan, *Vorticity generation and conservation for two-dimensional interfaces and boundaries*, Journal of Fluid Mechanics, 758 (2014), pp. 63–93.

[21] A. Burrows, *Supernova explosions in the universe*, Nature, 403 (2000), pp. 727–733.

[22] P. Carles, Z. Huang, G. Carbone, and C. Rosenblatt, *Rayleigh-taylor instability for immiscible fluids of arbitrary viscosities: A magnetic levitation investigation and theoretical model*, Physical Review Letters, 96 (2006), p. 104501.

[23] M. E. Cates and E. Tjhung, *Theories of binary fluid mixtures: from phase-separation kinetics to active emulsions*, arXiv preprint arXiv:1806.01239, (2018).

[24] M. L. Cecopieri-Gómez and J. Palacios-Alquisira, *Interaction parameter (x); expansion factor (ε); steric hindrance factor (σ); and shielding function f (ξ); for the system pea-organic solvents by intrinsic viscosity measurements*, Journal of the Mexican Chemical Society, 49 (2005), pp. 188–195.

[25] A. Celani, A. Mazzino, P. Muratore-Ginanneschi, and L. Vozella, *Phase-field model for the Rayleigh–Taylor instability of immiscible fluids*, Journal of Fluid Mechanics, 622 (2009), pp. 115–134.

[26] A. Celani, A. Mazzino, and L. Vozella, *Rayleigh-Taylor turbulence in two dimensions*, Physical Review Letters, 96 (2006), p. 134504.

[27] S. Chandrasekhar, *Hydrodynamic and hydromagnetic stability*, Courier Corporation, 2013.

[28] M. Chertkov, *Phenomenology of Rayleigh-Taylor turbulence*, Physical Review Letters, 91 (2003), p. 115001.

[29] M. Chertkov, I. Kolokolov, and V. Lebedev, *Effects of surface tension on immiscible Rayleigh-Taylor turbulence*, Physical Review E, 71 (2005), p. 055301.

[30] T. T. Clark, *A numerical study of the statistics of a two-dimensional rayleigh–taylor mixing layer*, Physics of Fluids, 15 (2003), pp. 2413–2423.

[31] J. D. Cowan and H. R. Wilson, *Excitatory and inhibitory interactions in localized populations of model neurons*, Biophysical Journal, 12 (1972), p. 1.

[32] R. C. Desai and R. Kapral, *Dynamics of Self-organized and Self-assembled Structures*, Cambridge University Press, 2009.

[33] P. D. Ditlevsen, *Turbulence and shell models*, Cambridge University Press, 2010.

[34] M. P. Do Carmo, *Differential geometry of curves and surfaces: revised and updated second edition*, Courier Dover Publications, 2016.

[35] S. Dyachenko and A. C. Newell, *Whitecapping*, Studies in Applied Mathematics, 137 (2016), pp. 199–213.

[36] L. C. Evans, *Partial differential equations*, Graduate Studies in Mathematics, 19 (1998).

[37] P. C. Fife, *Models for phase separation and their mathematics*, (2000).

[38] U. Frisch, *Turbulence: the legacy of A. N. Kolmogorov*, Cambridge university press, 1995.

[39] T. Funada and D. Joseph, *Viscous potential flow analysis of Kelvin-Helmholtz instability in a channel*, Journal of Fluid Mechanics, 445 (2001), pp. 263–283.

[40] J. L. Gondar and R. Cipolatti, *Iniciação à física matemática*, Modelagem de Processos e Métodos de Solução. Rio de Janeiro, IMPA, (2011).

[41] K. Gulati, J. F. Croix, S. P. Khatri, and R. Shastry, *Fast circuit simulation on graphics processing units*, in 2009 Asia and South Pacific Design Automation Conference, IEEE, 2009, pp. 403–408.

[42] Z. Guo and P. Lin, *A thermodynamically consistent phase-field model for two-phase flows with thermocapillary effects*, Journal of Fluid Mechanics, 766 (2015), pp. 226–271.

[43] E. Herman and G. Strang, *Calculus volume 1, 2, and 3*, (2018).

[44] H. Huang, D. T. Thorne Jr, M. G. Schaap, and M. C. Sukop, *Proposed approximation for contact angles in shan-and-chen-type multicomponent multiphase lattice boltzmann models*, Physical Review E, 76 (2007), p. 066701.

[45] K. Huang, *Statistical mechanics (john wiley and sons, 1987)*, Chap, 8, pp. 189–191.

[46] Z. Huang, A. De Luca, T. J. Atherton, M. Bird, C. Rosenblatt, and P. Carles, *Rayleigh-taylor instability experiments with precise and arbitrary control of the initial interface shape*, Physical review letters, 99 (2007), p. 204502.

[47] S. Jin and Q. Li, *A bgk-penalization-based asymptotic-preserving scheme for the multispecies Boltzmann equation*, Numerical Methods for Partial Differential Equations, 29 (2013), pp. 1056–1080.

[48] D. Joseph, *Viscous potential flow*, Journal of Fluid Mechanics, 479 (2003), pp. 191–197.

[49] D. D. Joseph, *Fluid dynamics of mixtures of incompressible miscible liquids*, in Applied and Numerical Partial Differential Equations, Springer, 2010, pp. 127–145.

[50] D. D. Joseph, A. Huang, and H. Hu, *Non-solenoidal velocity effects and Korteweg stresses in simple mixtures of incompressible liquids*, Physica D: Nonlinear Phenomena, 97 (1996), pp. 104–125.

[51] J. Kim, *Phase-field models for multi-component fluid flows*, Communications in Computational Physics, 12 (2012), pp. 613–661.

[52] D. B. Kirk and W. H. Wen-Mei, *Programming massively parallel processors: a hands-on approach*, Morgan kaufmann, 2016.

[53] A. N. Kolmogorov, *Dissipation of energy in the locally isotropic turbulence*, Proceedings of the Royal Society of London. Series A: Mathematical and Physical Sciences, 434 (1991), pp. 15–17.

[54] J. Koplik and J. R. Banavar, *Slip, immiscibility, and boundary conditions at the liquid-liquid interface*, Physical review letters, 96 (2006), p. 044505.

[55] T. Krüger, H. Kusumaatmaja, A. Kuzmin, O. Shardt, G. Silva, and E. M. Viggen, *The lattice Boltzmann method*, Springer International Publishing, 10 (2017), pp. 978–3.

[56] P. K. Kundu and I. M. Cohen, *Fluid mechanics*, Elsevier, 2001.

[57] A. G. Lamorgese, D. Molin, and R. Mauri, *Diffuse interface (di) model for multiphase flows*, in Multiphase Microfluidics: The Diffuse Interface Model, Springer, 2012, pp. 1–72.

[58] L. D. Landau and E. M. Lifshitz, *Course of theoretical physics*, Elsevier, 2013.

[59] L. D. Landau and E. M. Lifshitz, *Statistical Physics: Volume 5*, vol. 5, Elsevier, 2013.

[60] D. Lee, J.-Y. Huh, D. Jeong, J. Shin, A. Yun, and J. Kim, *Physical, mathematical, and numerical derivations of the Cahn–Hilliard equation*, Computational Materials Science, 81 (2014), pp. 216–225.

[61] D. Legland, K. Kiêu, and M.-F. Devaux, *Computation of Minkowski measures on 2D and 3D binary images*, Image Analysis & Stereology, 26 (2007), pp. 83–92.

[62] J. Li, *Multiscale and multiphysics flow simulations of using the Boltzmann equation.*

[63] ——, *Multiscale and multiphysics flow simulations of using the Boltzmann equation*, Springer, 2020.

[64] H. Liang, X. Hu, X. Huang, and J. Xu, *Direct numerical simulations of multi-mode immiscible Rayleigh-Taylor instability with high reynolds numbers*, Physics of Fluids, 31 (2019), p. 112104.

[65] C. Liu and J. Shen, *A phase field model for the mixture of two incompressible fluids and its approximation by a fourier-spectral method*, Physica D: Nonlinear Phenomena, 179 (2003), pp. 211–228.

[66] D. Livescu, *Compressibility effects on the rayleigh–taylor instability growth between immiscible fluids*, Physics of fluids, 16 (2004), pp. 118–127.

[67] A. A. Mailybaev and A. Nachbin, *Explosive ripple instability due to incipient wave breaking*, Journal of Fluid Mechanics, 863 (2019), pp. 876–892.

[68] E. Meshkov, *Some peculiar features of hydrodynamic instability development*, Philosophical Transactions of the Royal Society A: Mathematical, Physical and Engineering Sciences, 371 (2013), p. 20120288.

[69] E. E. Meshkov and S. I. Abarzhi, *Group theory and jelly's experiment of rayleigh–taylor instability and rayleigh–taylor interfacial mixing*, Fluid Dynamics Research, 51 (2019), p. 065502.

[70] C. NVidia, *Cuda c programming guide, version 9.1*, NVIDIA Corp, (2018).

[71] A. Obukhov, *The influence of hydrostatic forces on the structure of the temperature eld turbulent ow*, in Dokl. Akad. Nauk. SSSR, vol. 125, 1959, p. 1246.

[72] P. Perlekar, L. Biferale, M. Sbragaglia, S. Srivastava, and F. Toschi, *Droplet size distribution in homogeneous isotropic turbulence*, Physics of Fluids, 24 (2012), p. 065101.

[73] R. D. Petrasso, *Rayleigh's challenge endures*, Nature, 367 (1994), p. 217.

[74] S. B. Pope, *Turbulent flows*, 2001.

[75] P. Ramaprabhu and M. Andrews, *Experimental investigation of Rayleigh-Taylor mixing at small atwood numbers*, Journal of Fluid Mechanics, 502 (2004), p. 233.

[76] L. Rayleigh, *Investigation of the character of the equilibrium of an incompressible heavy fluid of variable density*, Proc. R. Soc., 14 (1883), pp. 200–207.

[77] H. Robey, Y. Zhou, A. Buckingham, P. Keiter, B. Remington, and R. Drake, *The time scale for the transition to turbulence in a high reynolds number, accelerated flow*, Physics of Plasmas, 10 (2003), pp. 614–622.

[78] D. Sart, A. Mueen, W. Najjar, E. Keogh, and V. Niennattrakul, *Accelerating dynamic time warping subsequence search with gpus and fpgas*, in 2010 IEEE International Conference on Data Mining, IEEE, 2010, pp. 1001–1006.

[79] M. Sbragaglia and D. Belardinelli, *Interaction pressure tensor for a class of multicomponent lattice Boltzmann models*, Physical Review E, 88 (2013), p. 013306.

[80] M. Sbragaglia, R. Benzi, L. Biferale, S. Succi, K. Sugiyama, and F. Toschi, *Generalized lattice Boltzmann method with multirange pseudopotential*, Physical Review E, 75 (2007), p. 026702.

[81] A. Scagliarini, L. Biferale, M. Sbragaglia, K. Sugiyama, and F. Toschi, *Lattice Boltzmann methods for thermal flows: Continuum limit and applications to compressible rayleigh–taylor systems*, Physics of Fluids, 22 (2010), p. 055101.

[82] L. Scarbolo, D. Molin, P. Perlekar, M. Sbragaglia, A. Soldati, and F. Toschi, *Unified framework for a side-by-side comparison of different multicomponent algorithms: Lattice Boltzmann vs. phase field model*, Journal of Computational Physics, 234 (2013), pp. 263–279.

[83] W. Schmidt, *From tea kettles to exploding stars*, Nature Physics, 2 (2006), pp. 505–506.

[84] D. Sevcovic and K. Mikula, *Evolution of plane curves driven by a nonlinear function of curvature and anisotropy*, SIAM Journal on Applied Mathematics, 61 (2001), pp. 1473–1501.

[85] E. D. Siggia, *High Rayleigh number convection*, Annual Review of Fluid Mechanics, 26 (1994), pp. 137–168.

[86] L. M. Siqveland and S. Skjaeveland, *Derivations of the young–laplace equation*, Unpublished research. https://doi. org/10.13140/RG, 2 (2014).

[87] J. C. Slattery, L. Sagis, and E.-S. Oh, *Interfacial transport phenomena*, Springer Science & Business Media, 2007.

[88] S.-I. Sohn, *Effects of surface tension and viscosity on the growth rates of Rayleigh-Taylor and Richtmyer-Meshkov instabilities*, Physical Review E, 80 (2009), p. 055302.

[89] S. Succi and S. Succi, *The lattice Boltzmann equation: for complex states of flowing matter*, Oxford University Press, 2018.

[90] H. S. Tavares, L. Biferale, M. Sbragaglia, and A. A. Mailybaev, *Immiscible rayleigh-taylor turbulence using mesoscopic lattice boltzmann algorithms*, arXiv preprint arXiv:2009.00054, (2020).

[91] ——, *Validation and application of the lattice boltzmann algorithm for a turbulent immiscible rayleigh-taylor system*, arXiv preprint arXiv:2101.04847, (2021).

[92] G. I. Taylor, *The instability of liquid surfaces when accelerated in a direction perpendicular to their planes. i*, Proceedings of the Royal Society of London. Series A. Mathematical and Physical Sciences, 201 (1950), pp. 192–196.

[93] S. Terrington, K. Hourigan, and M. Thompson, *The generation and conservation of vorticity: deforming interfaces and boundaries in two-dimensional flows*, Journal of Fluid Mechanics, 890 (2020).

[94] S. Thalabard, J. Bec, and A. Mailybaev, *From the butterfly effect to spontaneous stochasticity in singular shear flows*, Communications Physics, 3 (2020), p. 122.

[95] U. Thiele, S. Madruga, and L. Frastia, *Decomposition driven interface evolution for layers of binary mixtures. i. model derivation and stratified base states*, Physics of Fluids, 19 (2007), p. 122106.

[96] Y. Tonegawa, *Phase field model with a variable chemical potential*, Proceedings. Section A, Mathematics-The Royal Society of Edinburgh, 132 (2002), p. 993.

[97] J. Waddell, C. Niederhaus, and J. W. Jacobs, *Experimental study of rayleigh–taylor instability: low atwood number liquid systems with single-mode initial perturbations*, Physics of Fluids, 13 (2001), pp. 1263–1273.

[98] D. A. Wolf-Gladrow, *Lattice-gas cellular automata and lattice Boltzmann models: an introduction*, Springer, 2004.

[99] Y.-N. Young and F. Ham, *Surface tension in incompressible Rayleigh–Taylor mixing flow*, Journal of Turbulence, (2006), p. N71.

[100] P. Yue, J. J. Feng, C. Liu, and J. Shen, *A diffuse-interface method for simulating two-phase flows of complex fluids*, Journal of Fluid Mechanics, 515 (2004), pp. 293–317.

[101] D. Zhao and H. Aluie, *Energy cascades in rayleigh-taylor turbulence*, arXiv preprint arXiv:2006.04301, (2020).

[102] Y. Zhou, *Rayleigh–taylor and richtmyer–meshkov instability induced flow, turbulence, and mixing. i*, Physics Reports, 720-722 (2017), pp. 1 – 136.

[103] M. Zingale, S. Woosley, C. Rendleman, M. Day, and J. Bell, *Three-dimensional numerical simulations of Rayleigh-Taylor unstable flames in type ia supernovae*, The Astrophysical Journal, 632 (2005), p. 1021.